School of Physics and Astronomy

Muon Spin Relaxation As A Probe Of Electron Spin Relaxation in Organic Semiconductors

Doctoral Thesis

Maureen Willis
Queen Mary, University of London

Supervisors: Dr A. Drew and Dr. W. Gillin

Declaration

I declare that all the work presented in this thesis is my own

Signed ..... Maureen Willis

Abstract

The purpose of this thesis is to study the electron spin relaxation (eSR) in small organic molecular semiconductors using the muon spin relaxation (MuSR) technique. One of the inherent problems in utilising the spin degree of freedom is the lack of understanding of the fundamental mechanisms behind spin relaxation. Two interactions have been proposed as the dominant mechanisms behind the spin relaxation, the Hyperfine interaction (HFI) and the Spin Orbit (SO) interaction. There remains much debate over the models for these interactions and their exact role, a contention that drives the work carried out in this thesis.

The MuSR technique is utilised providing a novel molecular scale probe sensitive to relaxation rates in the range of 0.01-10 MHz. The Avoided Level crossing (ALC) MuSR application is useful in accessing the spin relaxation information. Temperature dependent ALC-MuSR measurements are performed for a selection of functionalised acenes and Quinolate molecules. Transverse field MuSR measurements are also taken to determine the Hyperfine coupling constants present. DFT and semi-empirical computational methods are employed to determine theoretical values for the isotropic and anisotropic terms and the suitability of these methods was discussed.

It is concluded that an intra-molecular eSR is present in all small organic molecular semiconductors. The mechanism behind this eSR was found not to be the HFI but in fact the SO interaction. It is also determined that the eSR is coupling to the vibrations in the molecule and a possible theory based on the curvature of the molecule from the vibrational modes inducing an enhanced SO coupling is proposed, which results in the eSR. The final part of this thesis looks at the future experiments that have been initiated or can be conducted to further the understanding of spin relaxation and determine the role of a vibrationally enhanced SO coupling.

Contents

Declaration **1**

Abstract **2**

List of Figures **7**

List of Tables **12**

1 Introduction **13**

2 Organic Semiconductors **15**

2.1 Introduction to Organic Semiconductors 15

2.2 SP^2 Hybridisation and π-Conjugation 17

2.2.1 Hybridisation 17

2.2.2 π-Conjugation 18

2.3 Transport in Molecules 19

2.3.1 Bands versus Hopping 19

2.3.2 Band Transport 21

2.3.3 Hopping transport 23

2.3.4 Experimental Evidence and Models 24

2.4 Spin Relaxation 27

2.4.1 Spin-Orbit Coupling 28

2.4.2 Hyperfine Interaction 30

2.4.3 Conventional Models 33

2.4.4 Vibrations, Curvature and Enhanced SO Coupling 35

3 Samples **39**

3.1 Small Molecules . . . 39
3.1.1 Tetracene . . . 39
3.1.2 Rubrene (Functionalised Tetracene) . . . 40
3.1.3 Pentacene . . . 41
3.1.4 TMS-Pentacene . . . 41
3.1.5 TIPS-Pentacene . . . 42
3.1.6 Triethylsilylethylnyl Series (TES-Series) . . . 43
3.1.7 Metal-Hydroxyquinoline Chelate Series (Quinolates) . . . 43
3.2 Sample Preparation . . . 45
3.2.1 Synthesis and Purification . . . 46
3.2.2 Re-crystalisation . . . 47
3.2.3 Characterisation . . . 47
3.2.4 Sample mounting . . . 52

4 Muon Spectroscopy 53
4.1 The Muon and Muon Production . . . 53
4.1.1 Pulsed ISIS Source . . . 54
4.1.2 Continuous PSI Source . . . 56
4.1.3 Muon Implantation . . . 58
4.1.4 Muon Decay . . . 60
4.2 Experimental Aspect . . . 61
4.2.1 Geometry . . . 61

5 Physics of Muonium 65
5.1 Muonium in a Longitudinal Applied Magnetic Field . . . 65
5.1.1 Isotropic Muonium . . . 65
5.1.2 Anisotropic Muonium . . . 69
5.1.3 Avoided Level Crossings . . . 70
5.2 Muonium in a Transverse Applied Field . . . 74

6 The Extraction of Avoided Level Crossings and determination of Muon Adduct Sites 77
6.1 Background Subtraction . . . 77

6.2 Muon Site Allocation 79
6.2.1 TIPS-Pentacene 80
6.2.2 AlQ_3 85

7 Electron Spin Relaxation in The Functionalised Acenes 89
7.1 Electron Spin Relaxation 89
7.1.1 TIPS-Pentacene 89
7.1.2 Rubrene 91
7.2 TIPS-Pentacene vs. Deuterated TIPS-Pentacene 92
7.3 Determining the Source of Electron Spin Relaxation Through the Muon Spin Deploarisation 95

8 Z-Dependence Study in the Quinolate and TES Series 102
8.1 The Quinolate Series 103
8.2 The TES-Series 107

9 Temperature Dependence 110
9.1 TIPS-Pentacene and Rubrene 110
9.2 Quinolate Series 113
9.3 Curvature and Enhanced SO in the Quinolate Series 116

10 Summary 120

11 Work in Progress 122
11.1 Z-Dependance of the Core V's the Ligand 122
11.1.1 X-substituted Quinolate Series (X-AlQ3 series) 122
11.1.2 TMX-ADT Series 125
11.2 Additional DFT and Temperature Studies 127
11.2.1 DFT 127
11.2.2 Temperature 128
11.3 Electron Spin Relaxation V's Electronic Transport in P3HT 129

Acknowledgements 136

Bibliography 146

A Errors: A Brief Note **147**

List of Figures

2.1 Organic electronic devices 15

2.2 Typical OLED structure 16

2.3 Organic solar cell 17

2.4 Hybridisation process 18

2.5 Orbital involved in the hybridisation process and the resultant hybridised orbitals 18

2.6 Orbitals in a π-conjugated Benzene ring 19

2.7 Energy levels in organic semiconductors 20

2.8 The effects of the superposition of the random hyperfine fields on the externally applied magnetic field for a normal and deuterated molecule 32

2.9 Orbitals involved in the curvature induced spin-orbit coupling and the resultant transitions between π and σ orbitals 36

2.10 Diagram showing the construction of a simple bending mode in Tetracene 37

3.1 Tetracene 40

3.2 Rubrene 40

3.3 Pentacene 41

3.4 TMS-Pentacene molecule and crystal structure 42

3.5 TIPS-Pentacene molecule and crystal structure 42

3.6 TES-ADX structure 43

3.7 Quinolates 45

3.8 Schematic of the train sublimation process 46

3.9 X-ray diffraction pattern of AlQ3 with refinement (green line) and difference plot (purple line) 48

3.10 X-ray diffraction pattern of GaQ3 with refinement (green line) and difference plot (purple line) 48

3.11 X-ray diffraction pattern of InQ3 with refinement (green line) and difference plot (purple line) 49
3.12 Example of silver packet used in experiments compared with a centimetre rule 52
3.13 Side profile design of E-Field sample mount 52

4.1 Surface pion decay 54
4.2 ISIS muon beam (note DEVA is now HIFI) 55
4.3 Double pulse structure 55
4.4 PSI rotating target 56
4.5 PSI Schematic 57
4.6 The muon's energy loss processes in a sample while spin is conserved throughout 59
4.7 Muon decay 61
4.8 MuSR experimental geometries 63

5.1 Energy levels of isolated muonium as a function of LF 66
5.2 Energy level splittings in isotropic muonium 68
5.3 Repolarisation and Breit-Rabi oscillations at three fields 68
5.4 Avoided level crossing 71
5.5 Muon spin polarisation tuning through ALC resonance 71
5.6 The effect of the a) A, b) D_1 and c) D_2 parameters on the ALC line shape 72
5.7 The effect of eSR on the muon spin polarisation both for the Rabi-oscillations and for the simulated ALC 75

6.1 An example of a typical repolarisation curve 77
6.2 An example of background fitting to the AlQ_3 time integrated data taken on the ALC spectrometer 78
6.3 Background fitting in the Functionalised Acenes 79
6.4 Full longitudinal field scan for TIPS-Pentacene at 10 K(blue) and 300 K(red) 81
6.5 Modelling of the two independent ALCs in group 1 in TIPS-Pentacene 81

6.6 Fourier analysis of TF time-resolved data in TIPS-Pentacene at 0.45 T and at 5 K taken on the DOLLY spectrometer (top). Maximum Entropy analysis of the same data with two clear frequencies resolved in the satellite peaks (bottom) 82

6.7 Structure for TIPS-Pentacene and Pentacene with muon assignments 83

6.8 Comparison of the TIPS-Pentacene and Pentacene group 1 ALC resonances at 10 K 84

6.9 DFT calculations by McKenzie (green dashed) and Pratt (red solid) for sites 1, 3, 4 and 6. Also 10 K resonance data for AlQ_3 (blue markers) and inset, the muon site allocation for each ligand on the Quinolate molecule 86

6.10 Complete sum of the ALCs from Pratt's DFT calculations with individual site components shown also 87

7.1 Group 1 ALC in TIPS-Pentacene plotted at 10 K and 300 K with modelling results shown as solid lines 90

7.2 Relaxation data in TIPS-Pentacene 90

7.3 ALC resonance in Rubrene plotted for six temperatures 91

7.4 Relaxation data for Rubrene 92

7.5 Relaxation rate against applied magnetic field for 10 K and 300 K at low fields showing the decoupling of nuclear HFCs 93

7.6 ALC resonances for a) TIPS-Penacene and b) deuterated TIPS-Pentacene at 10 K and 300 K with modelling results shown as solid lines 94

7.7 Electric field effects from track electrons 96

7.8 Application different electric fields 97

7.9 Pulse sequence for electric field experiment. Note the pulse widths are not to scale in this diagram; the pulse width for the positive and negative fields is 10 s and the pulse width for the zero field is 5 s . . . 98

7.10 Time resolved TF data for TIPS-Pentacene at 300 K for the three electric fields with a magnetic field of 20 G 99

7.11 Electric field data in the presence of an applied longitudinal field . . . 99

7.12 Data for electric field experiment on AlQ_3 by Drew et al. showing the relaxation rate alter upon the application of an electric field. Lower inset shows the electric field pulse sequence and upper inset shows the repolarisation curve 100

8.1 ALC resonance for AlQ_3 at 10 K and 300 K taken on the ALC spectrometer . . . 102

8.2 Relaxation data in AlQ_3 . . . 103

8.3 ALC spectra at 10 K and 300 K for: a) AlQ3, b) GaQ3, c) InQ3, d) BiQ3 with modelling results (solid lines) . . . 104

8.4 Minima of ALC resonances at 10 K and 300 K against Z-number with lines to guide the eye . . . 105

8.5 The eSR at 300 K plotted against Z-number for the quinolate (green squares) and TES (blue triangles) series fitted with a straight line (solid black line) . . . 106

8.6 ALC resonances at 10 K and 300 K for TES series with modelling results (solid lines) . . . 107

9.1 Temperature dependance of the eSR . . . 111

9.2 Temperature dependence of the eSR in the Quinolate series . . . 114

9.3 Z-number dependence of the eSR at various temperatures shown with confidence intervals . . . 115

9.4 Z-dependance of the energies in the Quinolate series . . . 116

9.5 The lowest five frequency bending modes in Pentacene used in the model by Fatini et al. . . . 117

9.6 Single component hyperbolic tanh function fits to temperature data . 118

9.7 Double component hyperbolic tanh function fits to temperature data 118

11.1 . . . 122

11.2 Fitted repolarisation curves . . . 123

11.3 Repolarisation fits around the resonance in the X-substituted AlQ_3 series . . . 123

11.4 ALC resonances in the X-substituted AlQ_3 molecules after background removal . . . 124

11.5 Modelling of a typical resonance to show the extremes of the shape and amplitude changes with eSR . . . 125

11.6 . . . 126

11.7 ALC spectra at 10 K and 300 K for TMS-ADT and TBU-ADT . . . 126

11.8 10 K ALC spectra for AlQ_3 with scaled data from DFT calculation (solid blue line) . . . 127

11.9 Lower field ALCs in TIPS-Pentacene at 10 K and 300 K with their coresponding site allocations (inset) 129

11.10Fitted time-integrated data in P3HT-RRa. Solid line shows fourth order polynomial fit in the local region to the ALC 130

11.11ALC spectra at 10 K and 300 K in P3HT-RRa 131

11.12ALC spectra in P3HT-RR at multiple temperatures and inset the polymer unit cell of P3HT 132

11.13Modelling of an ALC with varying hopping rates in a two site system 132

11.14Normalised ALC amplitudes of P3HT-RRa (purple), P3HT-RR old measurements(green), P3HT-RR new measurements (red) and crystalline P3HT-RR (blue) as a function of temperature. Solid lines are to provide a guide to the eye 133

11.15ALC spectra for P3HT-RR at various temperatures in the crystalline sample 133

List of Tables

3.1 X-Ray powder diffraction refinement results compared to published values 51

6.1 TIPS- Pentacene model parameters and DFT calculation results . . . 83

6.2 Comparison on calculated DFT and modelled HFCs in AlQ_3 86

7.1 TIPS- Pentacene model parameters 94

7.2 DTIPS- Pentacene model parameters 95

8.1 AlQ3 and GaQ3 model parameters where A, D and E are in MHz and eSR is in μs^{-1} 104

8.2 InQ3 and BiQ3 model parameters where A, D and E are in MHz and eSR is in μs^{-1} 105

8.3 TES-ADF and TES-ADT model parameters where A, D and E are in MHz and eSR is in μs^{-1} 108

8.4 TES-ADS model parameters where A, D and E are in MHz and eSR is in μs^{-1} 108

Chapter 1

Introduction

Organic semiconductors are currently at the forefront of much research as they have the potential for a wide range of future applications such as photovoltaics [1–3], organic field-effect transistors [4, 5], organic radio frequency (RFID) circuits [6–8], electronic paper [9, 10], organic-based sensors [11, 12], diodes [13], communication devices [14] and spin valves [15, 16]. In recent years we have seen some applications enter the commercial market from fundamental research [17]. The most notable of these technologies is the newest generation of screens based on organic light emitting diodes (OLEDs), in particular the evolving OLED televisions. This rapid development is driven by the unique properties of organic semiconductors, such as the mechanical flexibility [18], cheap fabrication [19, 20], easy processing [21, 22], long spin coherence time [23] and simply the vast availability and variety of molecules [24]. Their electronic and spin-related properties are highly tuneable with the chemical ability to manipulate atoms, atomic groups or even entire side groups of the molecule. Also many morphologies from amorphous right through to crystalline are producible. In the future, it may even be possible to synthesise the "perfect" structure giving the desired electronic, mechanical and spin-related properties for the application.

The functionality of many organic-based applications relies on the spin degree of freedom such as the next generation "race track memory" hard disks [25]. Given the amorphous organic layers which are used in most organic devices have very low charge carrier mobility, it is surprising that such organic-based spin devices work at all. In amorphous thin films, this is understood by the very long spin relaxation time typically explained by the weak spin-orbit interaction and/or hyperfine interaction in the carbon- and hydrogen-dominated organic materials [26–28]. The exact nature of the spin relaxation is still much a point of contention [26–28]. In the case of polymers, Rybicki and coworkers estimated, theoretically, a spin relaxation time of ≥ 1 μs by the use of a phonon-assisted spin relaxation mechanism that is based on the spin-orbit interaction [29]. Experimentally, a spin coherence time between 1 μs

and 1 s has been determined indirectly from various techniques, such as magnetoresistance and electron paramagnetic resonance (EPR) measurements [15, 23, 28, 30]. However, a spin coherence time of 1 s is considered too high by the scientific community, who argue such a value was deduced from parameters with a high uncertainty [30]. The uncertainties of parameters, like the charge carrier mobility, are a general problem when determining spin coherence times from magnetotransport measurements. EPR, on the other hand, relies on availability of free charge carriers. This is usually not the case for electrically neutral molecules and so doping would be required.

In this report, the electron spin relaxation in small molecular semiconductors is investigated with the muon spin spectroscopy technique. This technique has the unique ability to probe the charge carrier dynamics and the spin relaxation at a molecular level. In addition, it provides easily a sensitivity for electron spin relaxation rates between 0.01 MHz and 10 MHz and is therefore a powerful technique well-suited to measuring the electron spin relaxation rate quantitatively. In addition, because the samples investigated in detail in this report consist of various structures and morphologies, further insight into the spin relaxation mechanism can be gained. The Z (atomic number) dependence plays a key role in unlocking the mechanism behind spin relaxation and can offer clarification in understanding the dominant mechanism in organic semiconductors. This report presents the electric field dependant, deuteration and Z-dependant ALC-MuSR studies on a selection of small organic molecules. These studies support the idea of a spin-orbit based relaxation mechanism and not the more conventional Hyperfine Interaction. This indeed suggests a change in the current understanding of spin relaxation in organic semiconductors in order to fully utilise their potential in technological applications.

Chapter 2

Organic Semiconductors

2.1 Introduction to Organic Semiconductors

In todays world semiconductors dominate the field of electronics, so, the ability to control the many fundamental properties they have is essential. The advantages of organic materials over conventional ones include the ease that one can tune electronic functionality or make structural modifications and the ability for self-assembly and mechanical flexibility. It is then, perhaps, the potential of organic materials that is the driving force behind the interest in organic semiconductors. The main type of organic semiconductors currently being studied are π- conjugated. Typically the charge carriers in these materials move between molecules via the π-orbital ovalap. The materials fall in to two main categories, polymers and small molecules, with typical energy gaps of $\sim$1.5-3.5 eV. This energy gap between the Highest Occupied Molecular Orbital (HOMO) and the Lowest Unoccupied Molecular Orbital (LUMO) is critical to device applications as well as some of the fundamental physics of the semiconductors.

One of the first recorded organic semiconductors was in 1862 when Henry Letheby acquired a partially conductive material by the process of anodic oxidation on aniline, in sulphuric acid. It was later determined that the material was probably polyaniline [31]. This was a significant finding as it indicated that organic compounds could carry current. It was not until 1974 that an organic

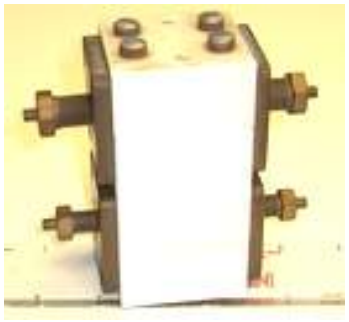

(a) First organic electronic device

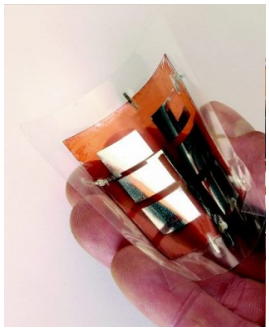

(b) Modern day organic electronic device

Figure 2.1: Organic electronic devices

electronic device was reported, resulting from the efforts of John McGinness and his co-workers in which they created an organic switch. They report how by the application of a voltage the organic semiconductor would go from a low conducting "OFF" state to a high conducting "ON" state. [32].

It was the proof of principle needed for the earlier paper, published in 1972, that reported metallic conductivity in the charge transfer complex tetrathiafulvalene - tetracyanoquinodimethane (TTF-TCNQ) [33]. This first device, which is a far cry from the devices that are produced today, can be seen in figure 2.1 alongside its modern counterpart [34]. The applications of organic semiconductors are rapidly growing, but three of the main uses are Organic Light-Emitting Diodes (OLEDs), organic solar cells and Organic Field Effect Transistors (OFETs).

An OLED is essentially like the more common light emitting diode (LED) in which the recombination of holes and electrons releases photons (light). However, the difference lies in the fact that the OLED uses a single organic semiconductor that has both electrons and holes (excitons) compared to the two types of conventional doped semiconductors used in normal LEDS. The first bilayer OLED device was invented in the 1980s by Tang and Slyke [35] approx. 20 years after the first observation of electroluminescence by Bernanose and co-workers [36–39]. The basic working principle can be seen in figure 2.2 with the bilayer structure. A conductive layer is also shown whose purpose is to improve the efficiency of the device.

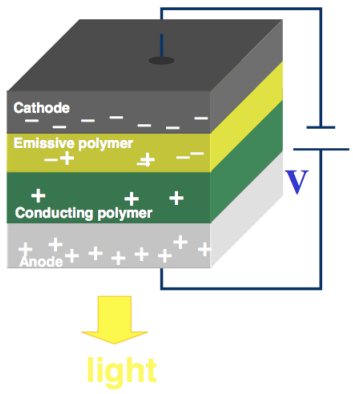

Figure 2.2: Typical OLED structure

There are now at least two types of OLED, those based on small molecules and those that use polymers. The more common small organic molecules used are metal organic chelates such as Tris(8-Hydroxyquinolinato) Aluminium [35] , fluorescent and phosphorescent dyes and conjugated dendrimers such as perylene, rubrene and quinacridone derivatives [40]. Typical polymers used in OLEDS are Polyaniline (PANI:PSS) and Polyethylenedioxythiophene (PDOT:PSS) which are conducting layer polymers and also Polyphenylenevinylene (R-PPV) and Polyflourene (PF) which are emissive layer polymers [41]. They exist in all varieties of modern technology such as television screens, computer monitors, mobile phones and PDAs. Organic Solar Cells (OSCs), also known as Organic Photovoltaic Cells, are essentially OLEDs that work the opposite way as to disassociate the excitons that are created by the solar energy (figure 2.3). The first solar cell was produced by Fritts in 1883 with an efficiency of ∼1%. The device was made from the semiconductor Selenium coated in a thin layer of Gold. Now solar cells are being produced using organic semiconductors (both small molecules and polymers)and there

are three main types; Single Layer, Bilayer and Dipersed Heterojunction [42, 43]. The materials that are currently used are discussed extensively by Peumans et al. in ref [44].

The last of the main applications is the OFET. The idea of a Field Effect Transistor (FET) was first patented by Lilienfeld in 1930 and the first one was built in 1960 by Kahng and Atalla. Now FETs have been adapted to be built with organic semiconductors. The idea is basically to have a conducting path (organic) between source and drain contacts (a conducting path capacitor) with a gate which controls this conduction by regulating the charge carrier movement. Some of the more common organics used are Tetracene, Pentacene, Rubrene, TCNQ and PPV for which reviews have been published [45, 46].

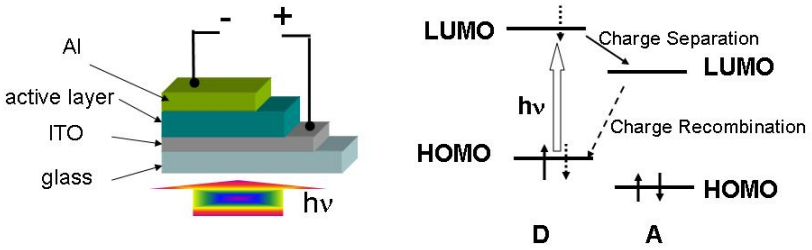

Figure 2.3: Organic solar cell

In the next sections I will review the more common transport and spin relaxation mechanisms for organic semiconductors.

2.2 SP^2 Hybridisation and π-Conjugation

As mentioned one of the key features in the organic molecules commonly being studied is that they are π-conjugated. This section describes the SP^2 hybridisation process that typically occurs in the aromatic benzene ring and in the molecules presented in this thesis. The bonding and molecular orbitals found in benzene molecules are then explained in order to understand the delocalisation present in π-conjugated organic molecules.

2.2.1 Hybridisation

The organic molecules presented in this thesis are predominantly based on the aromatic ring of benzene, which is built from Hydrogen atoms and Carbon atoms. The electron shell configuration of these atoms is $1s^1$ and $1s^2 2s^2 2p_X{}^1 2p_Y{}^1$ respectively and can be seen in the ground state in figure 2.4. In order to form the three bonds necessary in benzene the carbon requires more unpaired electrons and so the first step is the promotion of an electron from the 2s state to the empty $2p_Z$ state. The atom is now said to be in the excited state shown in figure 2.4.

In order to form the trigonal planar structure seen in the bonding in an aromatic ring the s-orbital needs to hybridise with two of the p-orbitals to form three hybridised

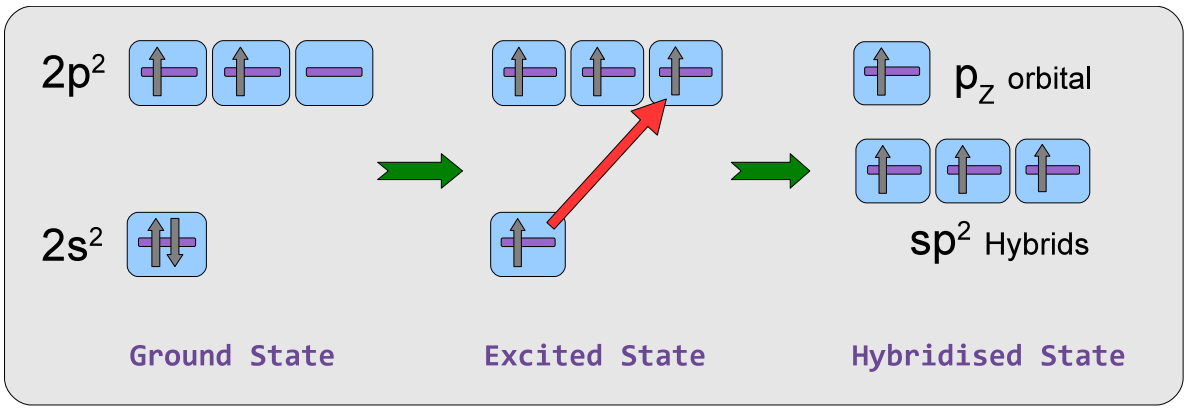

Figure 2.4: Hybridisation process

orbitals, the SP^2 orbitals. These minimise the electrostatic forces between them by orientating themselves in a plane 120° apart from one another. The p-orbitals involved are the $p_X{}^1$ and $p_Y{}^1$ and these are shown along with the resultant hybrid orbitals in figure 2.5. The remaining p_Z orbital is situated perpendicular to the trigonal plane and is unchanged by the hybridisation.

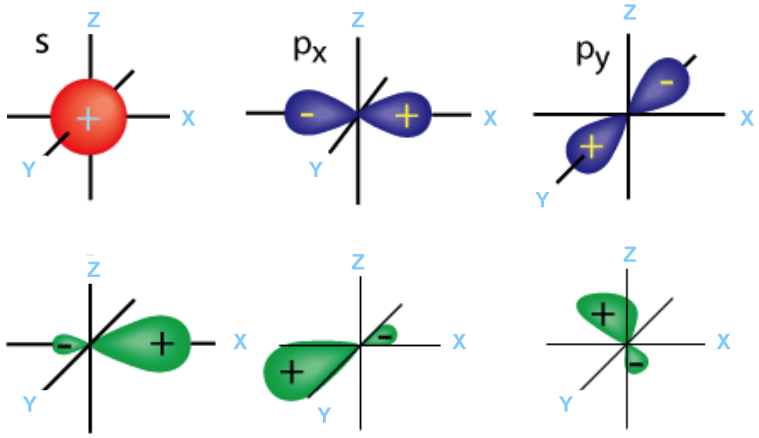

Figure 2.5: Orbital involved in the hybridisation process and the resultant hybridised orbitals

2.2.2 π-Conjugation

When benzene forms two of the sp^2 orbitals on each of the six carbons overlap to create two sigma bonds. However, the p_Z orbitals also overlap sideways to form six π-orbitals above and below the ring of sigma bonds (figure 2.6a). The overlap of these orbitals allows the unpaired electrons to move freely from one orbital to the next essentially spreading the charge around the whole ring and is referred to as π-conjugation. The result of this is that the electrons reside in pairs in three slightly different molecular orbitals which can be seen in figure 2.6b. The delocalisation around the ring reduces the energy of the molecule and hence the benzene ring is very stable.

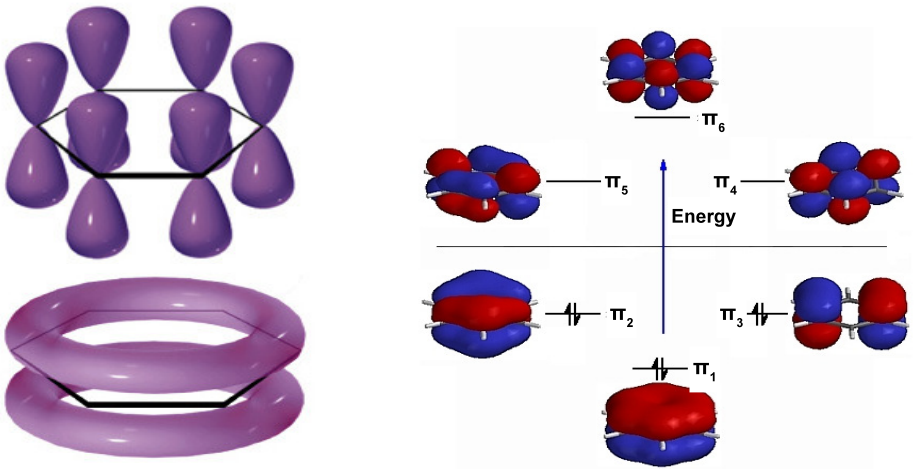

(a) π-orbitals in a Benzene ring

(b) Effect on orbitals in π-conjugation

Figure 2.6: Orbitals in a π-conjugated Benzene ring

2.3 Transport in Molecules

2.3.1 Bands versus Hopping

One of the key features of organic semiconductors is the weak Van der Waals forces that bind them together in the crystal structure. This feature allows the molecules to move more freely inducing phonons creating a vast vibrational spectra. This contributes greatly to the transport of charge carriers. As mentioned in the introduction the charge carriers in the molecules are the hole and electron which reside in the HOMO and LUMO respectively.

Even though the Van der Waals forces are weak there is a noticeable difference in the gaseous state energy gap, where the molecules can be considered isolated, and that of the solid state. The energy change associated with going from a gaseous state to a crystalline state is a decrease in the energy gap. In an amorphous structure the levels become somewhat more complex, taking on a distribution form. This is gaussian in nature with a FWHM of approx. 200 meV and can be seen in figure 2.7 [47].

Organic molecules present two opposite extremes of transport, band like transport and a site to site hopping transport.

A general model Hamiltonian can be used to describe the transport in an organic system [48]. This is shown in equation 2.1.

$$\mathcal{H}_{\text{model}} = \mathcal{H}_0 + \mathcal{H}_1 + \mathcal{H}_2 + \mathcal{H}_3 + \mathcal{H}_4 \tag{2.1}$$

Where

$$\mathcal{H}_0 = \underbrace{\sum_n \epsilon_n a_n^\dagger a_n}_{\text{Site Energies}} + \underbrace{\sum_\lambda \hbar\omega_\lambda \left(b_\lambda^\dagger b_\lambda + \frac{1}{2}\right)}_{\text{Phonon Energies}}$$

$$\mathcal{H}_1 = \underbrace{\sum_n \sum_m J_{nm} a_n^\dagger a_m}_{\text{Site to Site Coupling}}$$

$$\mathcal{H}_2 = \underbrace{\sum_\lambda \sum_n g_{n\lambda} \hbar\omega_\lambda a_n^\dagger a_n \left(b_\lambda + b_\lambda^\dagger\right)}_{\text{Local Electron-Phonon (Holstein) Coupling}}$$

$$\mathcal{H}_3 = \underbrace{\sum_n \sum_m \sum_\lambda f_{nm\lambda} \hbar\omega_\lambda a_n^\dagger a_m \left(b_\lambda + b_\lambda^\dagger\right)}_{\text{Non-Local Electron-Phonon (Peierls) Coupling}} \quad n \neq m$$

$$\mathcal{H}_4 = \overbrace{\underbrace{\sum_n \delta\epsilon_n a_n^\dagger a_n}_{\text{Energetic Disorder}}}^{\text{diaganol}} + \overbrace{\underbrace{\sum_n \sum_m \delta \mathrm{J}_n a_n^\dagger a_m}_{\text{Positional Disorder}}}^{\text{off-diaganol}}$$

where J, g and f are the coupling coefficients for the sites and short and long range phonons respectively, $a/b^\dagger$ and a/b are the creation and annihilation operators for the sites and phonon frequencies and ω_λ is the phonon with frequency λ.

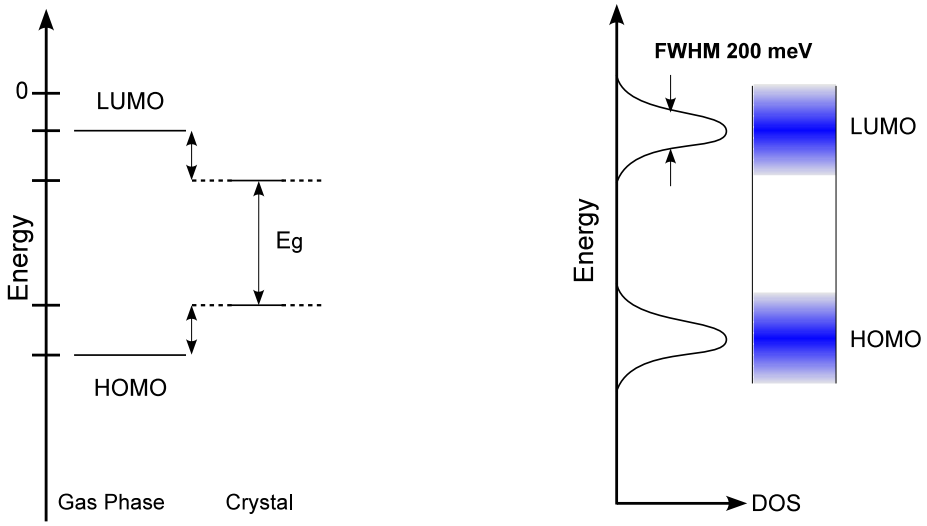

(a) Energy level configuration in gaseous and crystalline organic semiconductors

(b) Energy level configuration in amorphous organic semiconductors

Figure 2.7: Energy levels in organic semiconductors

2.3.2 Band Transport

The simplest model is delocalised transport in an electronic band. This arises when the site to site coupling constant is very large and hence the model hamiltonian is reduced to the $\mathcal{H}_0$ and $\mathcal{H}_1$ terms. In this case the charge carriers are completely decoupled from any phonons in the system. The wave-function of the charge carrier can be described by a simple classical band theory. The holes or electrons exist in the HOMO and LUMO equivalent to the conventional valence and conduction bands with a band gap of $\sim$1 eV. They follow the dispersion relation $\epsilon(k) = -2\tau\cos(kL)$ where τ is the hopping integral or electronic coupling between states localized on adjacent molecules, k is the wave-vector and L is the intermolecular distance and their motion is described classically by the Boltzmann equation [49]. If impurities or phonons exist, i.e. the system is not the idealistic ballistic system in a vacuum, then carriers with wave-vector k are scattered to the new state k'. The average time between two interactions can be described as a constant τ_S and hence the mobility of the system is represented by the equation

$$\mu = e\tau_S/m^*$$

where m^* is the reduced mass.

One of the key signatures, in the experimental data, of band transport is the temperature dependance of the mobility. This follows the well known power law $\mu \propto \mathrm{T}^{-n}$ and hence mobility decreases with increasing temperature. This simple band transport model is suitable in pure crystals or at very low temperatures however as the phonon scattering becomes more efficient as temperature increases it becomes necessary to introduce phonon coupling in to the model Hamiltonian.

This is carried out by considering the local electron-phonon coupling term (also known as the Holstein coupling). There are two regimes resulting from this term which are the weak coupling and the strong coupling regimes. In order to develop the weak coupling case it is assumed in the large polaron theories that the effect from the Holstein term can be considered a small perturbation which sightly modifies the wave-function. The more common perturbation theories used to treat the problem are the Rayleigh-Schrödinger and Brillouin-Wigner theories although more advanced theories have also been used [50]. The important result that is derived from this theory is that the electron phonon coupling alters the effective mass to give a renormalised effective mass $\bar{m}^*$. This can be related to the purely electronic effective mass with the following expression [50]:

$$\bar{m}^* = \frac{m^*}{1 - \alpha/6}$$

where $\alpha = \Delta E/\hbar\omega$ and ΔE is the energy related to the stabilisation of the polaron.

It is clear to see that if α reaches 6 then the polaronic effective mass tends to infinity signifying a breakdown in the large polaron model and the localisation of the charge.

It is now necessary to look at the strong coupling case which is modelled using strong electron-phonon coupling theory. This approach starts the complete opposite to the weak coupling theories in the sense that the electronic coupling term is assumed to be a perturbation on the effects from the electron-phonon coupling term. The molecules are considered to be totally isolated and to each have a set of vibronic states on the molecule. This produces the renormalised Hamiltonian from that described before. The resultant Hamiltonian can be seen in equation 2.3

$$\tilde{\mathcal{H}} = e^{S}\mathcal{H}_{\text{model}}e^{-S} \tag{2.3}$$

where e^S is a unitary operator defined such that $S = -g\sum_n \left(b_n^\dagger - b_n\right) a_n^\dagger a_n$. It acts as to diagonalise the non interacting components of the Hamiltonian. The application of the transformation to the electronic coupling term, which carries the electron-phonon coupling in this case, provides the renormalised electronic hamiltonian seen in equation 2.4.

$$\tilde{\mathcal{H}}_2 = e^{S}\mathcal{H}_2 e^{-S} \tag{2.4}$$

However this transformed coupling term still contains a complex mix of fermionic and bosonic modes which present a problem. To treat this problem the assumption that the charge carrier is still delocalised is made so the modified term can be approximated to its thermal average and the bosonic components eliminated. This implies that the inelastic processes are negligible and the occupation number of the phonons does not change throughout the transport. The Hamiltonian $\mathcal{H}_2$ is now reduced back to the original one with an additional pre factor:

$$\tau e^{-2g^2\left(N_\omega + \frac{1}{2}\right)}$$

with $N_\omega = \left[\exp\left(\hbar\omega/k_B T\right) - 1\right]^{-1}$. Essentially this pre factor is the temperature dependant reduction factor of the band width and inverse effective mass. As in the case of the large polaron theories the charge dynamics can be described semi-classically with the substitution of polaronic bands for the simple bands. The main result of this is that the mobility should reduce more markedly with increasing temperature.

Classical band theory can be used to explain band transport with the assumption that these short range bands can be analogous to the classical long range bands. It produces a T-dependance of that in equation 2.5 [47, 51]. It is assumed that at low temperatures the band transport remains dominant [52] if there are no traps.

$$\mu \propto \mathrm{T}^{-n} \tag{2.5}$$

2.3.3 Hopping transport

The assumption made in the case of the strong electron-phonon coupling that led to the modified $\mathcal{H}_2$ is only valid if the charge is delocalised. However this is not always the case and the charge may be localised to a single molecule with the ability to hop from one molecule to the next, each time experiencing a different phonon occupation number. Hence the system is in the hopping transport regime. In this case the charge hopping rate between two neighbouring molecules can be computed directly from the Hamiltonian discussed thus far. The computation is carried out using the Fermi Golden rule with two assumptions. The first is that the initial distribution of vibrational states is that of the Boltzman distribution and the second is that the system is in the limit of a small coupling τ. The simplest result is when the high temperature limit is assumed i.e. when $k_B T \gg \hbar\omega_0$ and is as follows:

$$k_{hop} = \frac{\tau^2}{\hbar}\left(\frac{\pi}{k_B T \Lambda}\right)^{1/2} e^{-\Lambda/4k_B T} \tag{2.6}$$

where Λ is the reorganisational energy from the more chemistry based representation of the electron-phonon coupling g [53–56]. The mobility can be extracted from equation 2.6 using the Einstein relation ($\mu = eD/k_B T$) and the relation $D = k_{hop} L^2$. For the region where Λ is sufficiently greater then $k_B T$ then the temperature dependance of the mobility follows an approximate Arrhenius law $\mu \sim \exp\left(-E_B/k_B T\right)$.

Thus far the non-local (Peierls) electron-phonon has been ignored in the model hamiltonian. However it is needed to relate the real systems to the models. This coupling modulates the hopping integral that is induced by the phonons and recent computations have shown that it plays a vital part in the transport mechanisms. The term in the Hamiltonian describing this coupling is:

$$\mathcal{H}_3 = \sum_n \sum_m \sum_\lambda f^2_{nm\lambda} \hbar\omega_\lambda a^\dagger_n a_m \left(b_\lambda + b^\dagger_\lambda\right) \quad n \neq m$$

The last term that is important to hopping transport is that describing the naturally occurring energetic and positional disorder typically found in organic semiconductors ($\mathcal{H}_4$ in equation 2.1). This term alters the the diagonal and off-diagonal components of the matrix respectively. There are various models which describe the energy level distributions in an organic semiconductor system and the various expressions for mobility can be extracted from them.

2.3.4 Experimental Evidence and Models

Models

The two transport regimes, localised and delocalised, pose the problem that they have different temperature dependancies for the mobility and so research has been undertaken to study the region or transition between the two regimes in order to achieve a more general hamiltonian. The recent work of Fratini et al. is an exmple of this as they are proposing a model which combines the band like structure in a diffusive case and then allows for the interruption by thermal lattice vibrations in a dual transport model for the intermediate band-hopping regime [57].There are studies by other authors who have looked at the intermediate regime in between hopping and band transport including Cheng and Silbey who used a variational approach to find the best degree of localisation of the electronic wavefeunction [58]. However the temperature region in which they predict the cross over from bands to hopping is small and not consistent with the experimental data. Other elegent theories involve the interpolation scheme proposed by Loos et al. [59] and the general path integral method [60] originally introduced by Feynmann [61].

The short range, band-like, transport is believed to occur in highly pure crystals at low temperatures as there are few defects or phonons to scatter or interfere with motion of the charge carriers [62]. Cheng et al. [63] determine that a band model is not plausible above 150 K although there are reports of band-like motion even up to room temperature.

The interesting aspect however, is the discrepancy in the model behind hopping transport. The existence of a polaronic self-trapping model and one derived from the thermal fluctuations cause a point of contention amoung the different groups in the community. The first of the disputed models is the self-trapping polaron model where the charge carrier couples to the phonons in the lattice and undergoes incoherent polaronic motion. There are small polarons where the coupling only extends locally and large polarons where the polaron dimensions are large in comparison to the lattice spacing. These are discussed in Emin's paper along with their optical properties [64].

Holstein considered in 1959 the idea of polaron motion in which he studies both the small and large polaron case applying the Molecular Crystal Model. He first uses the application of the tight binding model to derive an exact solution for the large polaron motion and compares it to the Continuum Polarisation Model in conventional polaron theory. This is then applied to the small polaron case in which he reports there are two apparent temperature regimes produced through the analysis of on and off diagonal elements in the matrix describing the vibrational state of the system. Ultimately this results in a transition of the transport from bands to activa-

tion energy type hopping of the polaron [65, 66]. One problem with Holsteins model is that he does not consider the non-local electron-phonon coupling (the Peierls coupling) discussed earlier which proves to be important for the mobility in organic semiconductors.

This coupling was integrated in to the Holstein model by Hannewald et al. in 2004 by the use of a more general Hamiltonian (equation 2.7)in which the introduction of the $\mathcal{H}_3$ is seen. The last term ($\mathcal{H}_3$) is the important term and essentially describes the creation or annihilation of an electron coupled to a phonon (with frequency ω_Q) on a neighbouring site using the transfer integral probability g_{Qmn}. They carry it through using much the same logic as Holstein and show that a Polaronic band (from the renormalisation of the purely electronic band) is formed which has a temperature dependent narrowing on heating leading to a localised polaron hopping. They use this to derive the parameters of the hamiltonian from first principles for Naphthalene (a two ringed version of the Tetracene discussed later). The model correctly reproduces the temperature dependance of the mobility and highlights the importance of the non-local electron-phonon interactions in polaronic transport [67]. It is worth noting that from their studies it appears the LUMO couples more strongly to the phonons then the HOMO and so it encourages hole transport. There are other approaches which are analogous to Hannerwald's like those of Munn [68] and Zhao [69] and more recently Wang [70] and their co-workers however their models do not allow for first principles evaluations.

$$\mathcal{H} = \underbrace{\sum_{mn} \epsilon_{mn} a_m^\dagger a_n + \sum_Q \hbar\omega_Q \left(b_Q^\dagger b_Q + \frac{1}{2} \right)}_{\text{Energy contribution with no interactions}} + \underbrace{\sum_{mnQ} \hbar\omega_Q g_{Qmn} \left(b_Q^\dagger + b_Q \right) a_m^\dagger a_n}_{\text{site to site electron-phonon coupling}} \quad (2.7)$$

However there is the opinion from other members in the scientific community that this polaronic self-trapping transport model is not correct. Fishchuck et al. [71] suggest in their paper that the polaron model assumes a strong electron phonon coupling which they believe is not true and that the predicted transfer integrals are too high for solids with weak Van der Waals forces. They also conclude that the small polaron models contradict the experimental evidence of a transition from non-dispersive to dispersive transport regimes on lowering the temperature. Although they do not derive a completely new model they do adapt the polaronic one such that there is an energy term from the disorder contribution in the system i.e. they introduce the $\mathcal{H}_4$ term. The most important argument is that the band renormalisation polaronic models always imply the possibility that the vibrations can be averaged out and indeed Holstein explicitly carries out a thermal average when calculating the off diagonal matrix elements. This is the key assumption described earlier to eliminate the bosonic modes and has led to the second of these contentious models.

Troisi and Orlandi devised a transport model in 2006 dubbed Diffusion Limited by Thermal Disorder (DLTD) [52, 72] in which there is a stark contrast to the previous model. They suggest that the transport is neither polaronic nor the combination of thermally activated hopping and polaronic transport. Their model assumes that thermal molecular motions (essentially phonons) cause fluctuations in the charge transfer integrals which lead to the localisation of states by the destruction of the translational symmetry in the electronic Hamiltonian. The fluctuations to the charge transfer integrals are of the same order as the integrals themselves and so it leads to the break down of the band transport and the conventional wave vector k, used classically to characterise bands, is no longer is a good quantum number to describe the system. They also show that their model is in good agreement with the fluctuations in Pentacene and causes dynamic localisation of the charge carriers. Troisi did extend the model a year later to incorporate the local electron-phonon interactions and successfully calculated the temperature dependance of the mobility in the organic molecule Rubrene [73]. Also the recent work of Fratini et al. complements this as they are proposing a model which combines the band like structure in a diffusive case and then allows for the interruption by thermal lattice vibrations in a dual transport model for the intermediate band-hopping regime [57].

Experimental Evidence

The experimental community have provided, and still are providing, vast amounts of optical and electrical measurements that continue to test and develop the models used to describe charge carrier dynamics. Indeed many of these measurements involve the small organic molecules presented in this thesis. There are three main categories of experimental evidence that currently exist.

The first is that of the work in high purity and crystalline materials that show the presence of bands and require a band-like model. Measurements on highly purified samples of pentacene and rubrene (presented later) show that if a suitable limit is reached where defects are sufficiently low in number then the transport behaviour in these samples is very much band like [74–76]. The same result is possible through solution processing thin films [77] so may prove relevant in the field of organic transistors. Also Hall measurements show behaviour consistent with a delocalised transport mechanism. They display a significant effect in the presence of a magnetic field not expected from a localised hopping transport mechanism [78, 79].

The second catagory of evidence is that of complete localisation. Electron spin resonance (ESR) measurements by Marumoto et al. [80] on thin film pentacene showed localisation of charge carriers to within 10 molecules or less at room temperature. In addition charge modulated spectroscopy (CMS) measurements have shown behaviour that displays the signature of localised charge states in the case of

pentacene [77].

The last category of experimental evidence and probably the most interesting and relevant is that of dynamic localisation. This involves the transition from a polaronic band theory to one of localised charge carriers induced by the dynamic disorder in the organic semiconductors. Lang et al. [81] show the presence of localised states in addition to a coupling to low frequency phonons in the tail of the density of states (DOS). They evaluated the tail in pentacene using photocurrent and electrical measurements. Also Pernstich et al. carried out thermoelectricity measurements in Rubrene in a study of the DOS [82]. They conclude a similar idea to Fratini et al. [57] that there is a band like transport with thermally activated traps. Finally Koch et al. [83] studied the electronic properties of a thin film of pentacene on graphite using energy dependant photoelectron spectroscopy. They initially use a band theory model to analyse the data but conclude the localisation of charge carriers induced by the thermal disorder upon heating. They determined the crossover from bands to localisation at approximately 120 K.

This section has only briefly covered the experimental evidence and work currently being conducted in order to highlight the need for a clearer model, but there remain many more experiments which raise may more questions about the transport in organic semiconductors.

2.4 Spin Relaxation

The spin of an electron can relax (change direction or quantum mechanical state) through spin-depolarising interactions with its environment in a medium. In general the relaxation of a spin polarised ensemble is very complex. However, two classes of spin relaxation can be distinguished. The first is a depolarisation of the longitudinal spin component through interactions with the lattice i.e. phonons and is generally slower as it involves energy exchange with the environment. It has a characteristic relaxation time denoted T_1. The second is a process which effects the transverse spin component and causes a dephasing through fluctuations in the rotational frequencies. This has a shorter characteristic relaxation time denoted T_2 although these two time scales are commonly amalgamated in to one characteristic time τ_s. The dominant relaxation mechanism in organic materials is still unclear and leaves much for dispute among different research groups. There are, however, two main mechanisms namely the Hyperfine Interaction (HFI) and Spin-Orbit coupling (SO) which will be reviewed in this section.

2.4.1 Spin-Orbit Coupling

SO is believed by some to play a role in spin relaxation in organic molecules. It does not involve the nuclear spins in the system but instead is a relativistic effect that sees the electric field from the atoms core converted in to a magnetic field, in the rest frame of the electron. This is carried out by applying a Lorenz transform for which the derivation given by Atkins and Friedman is below [84].

For an electron with mass m_e and momentum $p_e = m_e v_e$ moving in an electric field ϵ_{SO} the magnetic field is given by

$$\vec{B}_{SO} = -\frac{1}{m_e c^2}\vec{p} \times \vec{\epsilon}_{SO}$$

If the potential is assumed isotropic then the electric field ϵ_{SO} can be given by

$$\vec{\epsilon}_{SO}(r) = -\frac{1}{e}\frac{\mathrm{d}V(r)}{\mathrm{d}r}\frac{\vec{r}}{r}$$

so we can then write

$$\vec{B}_{SO} = \frac{1}{re m_e c^2}\frac{\mathrm{d}V(r)}{\mathrm{d}r}\vec{p} \times \vec{r}$$

and knowing that $\vec{L} = \vec{r} \times \vec{p}$ we obtain the equation

$$\vec{B}_{SO} = -\frac{1}{re m_e c^2}\frac{\mathrm{d}V(r)}{\mathrm{d}r}\vec{L} \tag{2.8}$$

Now, the hamiltonian H_{SO} of an interaction between the electron's magnetic moment and the SO magnetic field is given by

$$H_{SO} = -\vec{\mu}_e \cdot \vec{B}_{SO}$$

Using $\vec{\mu}_e = (g_e e/2m_e)\vec{S}_e$ where $g_e \approx 2$ and substituting in equation 2.8 produces the equation for the energy E_{SO}

$$E_{SO} = \frac{1}{m_e^2 c^2}\left\langle \frac{1}{r} \right\rangle \frac{\mathrm{d}V(r)}{\mathrm{d}r}\left\langle \vec{L} \cdot \vec{S}_e \right\rangle \tag{2.9}$$

So, if an electrostatic potential V_{SO} is used where

$$V_{SO}(r) = -\frac{e^2 Z_{\text{eff}}}{r}$$

then equation 2.9 becomes

$$E_{SO} = \frac{e^2 Z_{\text{eff}}}{m_e^2 c^2}\left\langle \frac{1}{r^3} \right\rangle \left\langle \vec{L} \cdot \vec{S}_e \right\rangle$$

It is worth noting that this derivation is based on the assumption that one can

step from the point of view of a stationary nucleus to the moving electron without treating the change relativistically. In fact this is not the case and gives rise to Thomas precession where the factor g_e is half its value so $g_e \approx 1$. Knowing this and applying the solution to the integral of the radial equations [85] the common relation of the energy can easily be obtained.

$$\left\langle \frac{1}{r^3} \right\rangle \propto \frac{Z_{\text{eff}}^3}{a_0^3}$$

where a_0 is the Bohr radius. Therefore

$$E_{SO} \propto \frac{e^2 Z_{\text{eff}}}{2m_e^2 c^2} \frac{Z_{\text{eff}}^3}{a_0^3} \left\langle \vec{L} \cdot \vec{S}_e \right\rangle$$

and so

$$E_{SO} \propto Z_{\text{eff}}^4 \tag{2.10}$$

Organics materials more commonly consist of Carbon and Hydrogen atoms which have low proton numbers. In comparison with more conventional materials this would imply a rather weak SO. Indeed there is much debate over if, and how much, the SO plays a role in spin relaxation. Recently Dedui et al. in a progress article concluded that the SO was too small to be considered as a mechanism for spin relaxation and instead argue that the theories based on the HFI should be developed [28]. This is supported by the work of Bobbert et al. who devise a theory for Spin Diffusion in Disordered Organic Semiconductors based on incoherent hopping of a charge carrier and coherent precession of its spin in an effective magnetic field, composed of the random hyperfine field of hydrogen nuclei and an applied magnetic field [86]. This is more evident by Bobbert's report on what makes spin relax in which he discounts the SO and discusses the HFI [27]. There are also studies by Nguyen [87] and McCamen [88] and their co-workers supporting the theory of a HFI mechanism.

In strong contrast to this Bandyopadhyay [26] produces a compounding collection of experimental evidence to suggest there is a contradiction between the experimental data and the predictions from theory based on the HFI. He also provides evidence to support the Elliot-Yafet mechanism one of the main conventional SO models which will be reviewed later in the section. It is argued that, in the case of the π-conjugated organic molecules, the wave functions of the π-electrons are mainly in the P_Z orbitals which contain nodes in the molecular plane [23, 26, 89]. Therefore, any in-plane contact hyperfine interactions would be weak. Also Kanchibotia et al. conclude that the long T_2 relaxation time they observe in AlQ3 is a direct result of SO [90] and this is complimented by the work of Rolfe et al. in which they deuterate

the AlQ3 and perform Magneto Resistance measurements to disprove the role of the HFI [91]. Further contrary to the HFI are the studies of Drew et al. in which they observe a rapid decrease in the spin diffusion length with increasing temperature not predicted by the HFI [92].

2.4.2 Hyperfine Interaction

The HFI is the other possible candidate for the spin relaxation mechanism and as mentioned previously some believe that it is the dominant mechanism owing to the weakness of the SO in organic materials. However, aside from being a possible mechanism for spin relaxation it is still of great importance as it is the origin for the spin-spin coupling between the electron and the muon. The HFI has two main parts to it, the Fermi Contact Term (FCT) and the Dipolar Term (DT). In some cases there are higher order terms but in most cases they are negligible. The Hamiltonian for the HFI is derived below using the method given in reference [93].

The ratio between the magnetic moment and angular momentum is given by the gyromagnetic ratio (γ) and is defined for a particle of charge q to be [84]

$$\gamma = \frac{qg}{2m}$$

where g and m are the g-factor and mass of the particle respectively. Knowing this the relationship can be derived between the magnetic moment of a particle ($\vec{\mu}_i$) and its spin ($\vec{S}_i$).

$$\vec{\mu}_i = \gamma_i \vec{S}_i = \frac{qg}{2m}\vec{S}_i \tag{2.11}$$

Now a magnetic dipole vector potential ($\vec{A}_{\text{dip}}$) is produced from the magnetic moment of the nucleus or muon ($\vec{\mu}_I$) which is given as a function of $\vec{r}$, the distance to where the electron resides, in equation 2.12 where μ_0 is the permeability of a vacuum.

$$\vec{A}_{\text{dip}}(\vec{r}) = \frac{\mu_0}{4\pi}\frac{\vec{\mu}_I \times \vec{r}}{r^3} = \frac{\mu_0}{4\pi}\nabla \times \frac{\vec{\mu}_I}{r} \tag{2.12}$$

By using this equation and the standard identity $\nabla^2(1/r) = -4\pi\delta(\vec{r})$ the magnetic flux density can now be derived.

$$\begin{aligned}\vec{B}(\vec{r}) &= \nabla \times \vec{A}_{\mathrm{dip}}(\vec{r}) \\ &= \nabla \times \frac{\mu_0}{4\pi}\nabla \times \frac{\vec{\mu}_I}{r} \\ &= \frac{\mu_0}{4\pi}\left[\nabla\left(\vec{\mu}_I \nabla \frac{1}{r}\right) - \vec{\mu}_I \nabla^2 \frac{1}{r}\right] \\ &= \frac{\mu_0}{4\pi}\left[\frac{3\vec{r}(\vec{\mu}_I \cdot \vec{r}) - \vec{\mu}_I r^2}{r^5} + 4\pi\vec{\mu}_I \delta(\vec{r})\right] \end{aligned} \tag{2.13}$$

There are two separate parts to equation 2.13. The first part is the dipole-dipole interaction and has the expected typical r^3 dependance. The second part describes the now deemed FCT. It is worth noting that this derivation does not take in to account the demagnetisation from the field of the nucleus. Soliverez [94] discusses the changes to the FCT from a spherical nucleus. He determines the factor to be $8\pi/3$ instead of the derived 4π. This agrees with the theory in reference [93] where the derivation is for spherical field. Moskowitz and Della Torre [95] also report a theory in which there is a tensor for the demagnetisation factors. This however, is a simplification of what is a more complex core and is incorrect for point like particles such as the muon. Having derived the magnetic flux density it is now possible to continue to derive the Hamiltonian for the HFI.

$$\begin{aligned} H &= -\vec{\mu}_e \cdot \vec{B}(\vec{r}) \\ &= -\mu_0 \vec{\mu}_e \vec{\mu}_I \delta(\vec{r}) + \frac{\mu_0}{4\pi}\left[\frac{(\vec{\mu}_e \cdot \vec{\mu}_I)r^2 - 3(\vec{\mu}_e \cdot \vec{r})(\vec{\mu}_I \cdot \vec{r})}{r^5}\right] \\ &= H_{\mathrm{FC}} + H_{\mathrm{DD}} \end{aligned} \tag{2.14}$$

The expectation value for the electron to be in an orbital $\psi(\vec{r})$ can be used with respect to the δ function. Given this and substituting the magnetic moment from equation 2.11 the H_{FC} becomes

$$H_{\mathrm{FC}} = -\mu_0 \gamma_e \gamma_I |\psi(\vec{r}=0)|^2 \vec{S}_e \cdot \vec{S}_I = A\vec{S}_e \cdot \vec{S}_I \tag{2.15}$$

where $|\psi(\vec{r}=0)|^2$ is the probability of the electron residing at the nucleus and A is the isotropic Hyperfine Coupling constant (HFC). The FCT is more commonly denoted the isotropic term and the DT is denoted the anisotropic term. With the use of a tensor $\tilde{A}$ to encompass all the HFCs equation 2.14 can be generalised to

$$H = \vec{S}_e \cdot \tilde{A} \cdot \vec{S}_I \tag{2.16}$$

It is fluctuations to or modulations of the HFCs that can lead to spin relaxation and dephasing and there are many origins to these discussed by Žutić and co-workers [96]. As mentioned previously there are theories on how the HFI is a mechanism for spin relaxation. Bobbert's theory assumes that the electron which ordinarily resides in the π-orbital sees the nuclear spins, mainly from the Hydrogens, in their mostly pure S-Orbitals [27, 86].

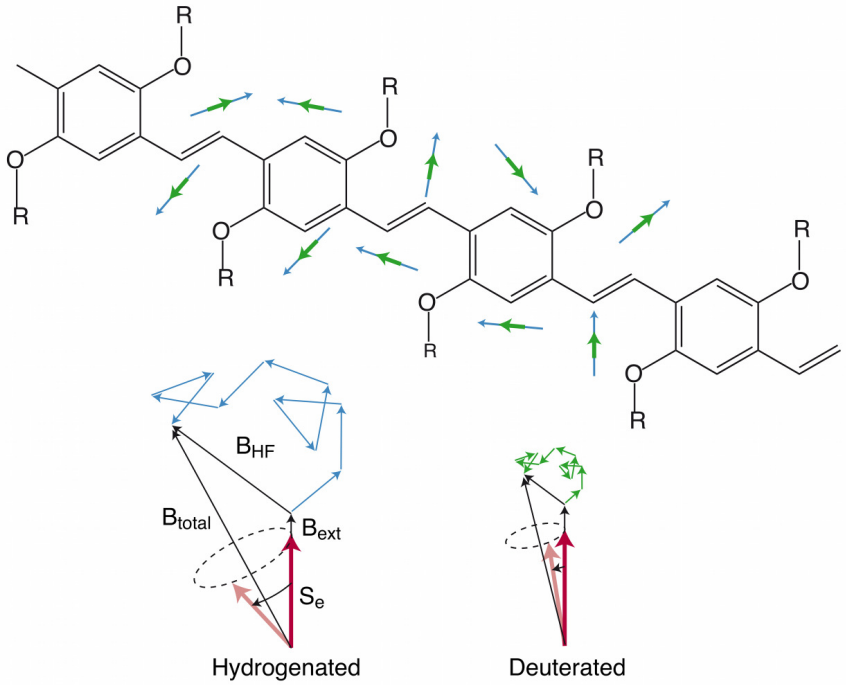

Figure 2.8: The effects of the superposition of the random hyperfine fields on the externally applied magnetic field for a normal and deuterated molecule

The work of McConnell showed that this assumption could indeed be possible by using first order perturbation on a three electron system, where one is the free radical, one is the pure S-Orbital of the Hydrogen and the third is SP-Hybrid orbital of the Carbon atom essentially forming one corner of an aromatic ring. He also showed that in addition there was a dipole-dipole coupling of the π-electron spins to the proton spins [97].The combination of these effects results in a HFC corresponding to a few mT [27]. Also the work of Schulten and Wolynes shows that if there are many proton spins involved then the electron spin precesses around a more classical random Hyperfine field added to an externally applied magnetic field [98]. A pictorial representation of this can be seen in figure 2.8. The Model leads to either a dephasing of the spin ensemble through band-like coherent motion through the sample, or to a relaxation of the spins through an incoherent diffusion/hopping motion. In both, the hyperfine fields have abrupt changes. Bobbert acknowledges that it is still controversial as to if, and how much, this model contributes to spin relaxation [27]. He proposes a simple way to test it in which the Hydrogen atoms are replaced with Deuterium and the sample is said to be Deuterated. As a result the strength of the HFI should be considerably reduced as illustrated in figure 2.8.

Nguyen's work on the deuterated and non-deuterated DOO-PPV polymer supports this model with the claim that they see a clear difference in the optically detected magnetic resonance, magneto-electroluminescence and giant magnetoresistance of the two samples [87]. As briefly mentioned before the work of Rolfe et al. strongly contradicts this. They tested deuterated and normal AlQ3 to compare the light output in an external magnetic field. It is their belief that the magnetoresistance (MR) stems from the fact electron-hole spin pair singlets recombine quicker then those of the triplets and hence the intersystem crossing (from triplet to singlet state) is altered resulting in an altered light output. This MR would then be expected to be independent of the HFI and given they saw no change between the two samples they claim not to support the HFI as the dominant relaxation mechanism [91]. It is clear that more understanding needs to be gained to reach a conclusive theory.

2.4.3 Conventional Models

Elliot-Yaffat (EY)

The EY mechanism uses the 4-component Dirac equation (equation 2.17) to introduce the spin-orbit coupling in to the classical band theory [99, 100]. They essentially derive a spin flip mechanism caused by the presence of impurities and phonons.

$$\left[\frac{\vec{p^2}}{2m} + \vec{V} - \frac{\vec{p^4}}{8m^3c^2} + \frac{\hbar}{4m^2c^2}(\nabla\vec{V}\cdot\vec{p}) + \frac{\hbar}{4m^2c^2}(\nabla\vec{V}\times\vec{p})\cdot\vec{\sigma}\right]\Psi = E\Psi \qquad (2.17)$$

They calculate the matrix elements for the Dirac equation and establish a probability for an electron spin flip caused by the scattering of the momentum by phonons. This spin flip is mediated by the spin-orbit interaction and causes a mixing of the spin up and spin down states and hence causing the electron spin to relax. The relaxation is characterised by a time τ_s which is proportional to the relaxation time T_1. They also apply the theory to experimental data in which they show it is good agreement with the corrected g-values for some semiconductors. The theory is also applied in the case of pure metals in the studies by Beuneu and Monod [101]. The model assumes that firstly the system is approximated by a tight binding model and that the Wannier functions can be applied. The most relevant assumption which makes it a problem to apply the model to organic semiconductors is that there are conventional bands and so essentially the application of classical band theory. As previously discussed this is not the case, however, there are mechanisms that are EY like that have recently been published so imply that the EY model cannot be ruled out completely [23, 26, 90].

D'yakonov-Perel (DP)

D'yakonov and Perel [102] use the lack of spatial inversion symmetry in the system to account for a de-phasing effect in the electron spin. The inversion asymmetry lifts the degeneracy of the spin up and spin down states of the electron to cause a splitting in the energy levels. They conclude that this can be described by a momentum dependent magnetic field B_{DP} which leads to a series of spin precessions with different frequency. This is further explored by Žutić [96] and Fabian et al. [103] in which the relationship derived by D'yakonov and Perel, $\Omega_{DP} \propto B_{DP}$, is discussed. The de-phasing occurs due to the fact there is such a de-coherence in the electron spin precession frequencies. Furthermore they experience momentum changes which add to the de-phasing and hence enhance the electron spins relaxation. The problem with this mechanism is that like the EY mechanism it relies heavily on the existence of conventional band. In addition the fundamental assumption of there being spatial inversion asymmetry does not hold true in the case of some of the small molecules discussed in chapter 3 so leads to the conclusion that the DP model is not applicable.

Bir-Aronov-Pikus (BAP)

Bir et al. [104] propose a very different model to that of EY and DP. They use the idea that conduction electrons can scatter on holes and the scattering is dictated by an interaction between the electron spin S_e and the angular momentum of the hole. It is the time of the interaction for which the electron is at a distance r , less then the electron wavefunction, from the hole that is key to the electron spin relaxation rate. The Hamiltonian describing this interaction is written as

$$\hat{H} = A_{BAP} S_e J \delta(r)$$

where A_{BAP} is the exchange integral between the conduction electron and the valence hole. They discuss how there are two conditions for the relaxation time. The first is the condition where the interaction time is equal to the diffusion time of the holes in the interaction region. Naturally this condition leads to a fast relaxation time and is essentially describing the dependance of the spin relaxation time on the hole concentration. The second condition is when the spin of the holes is relaxing quicker then the interaction time and this leads to an averaging of the electron hole spin interaction and hence long electron spin relaxation times. The main assumption of this model is that there are high hole concentrations and this is usually not the case in organic materials. Also the model requires the hole and electron to reside on the same molecule for the distance to be conceivable where they would form an exciton which would annihilate or dissociate. Given that the MuSR technique only provides a low concentration of muon and even less bound Muonium (which is covered in a

later chapter) the model is not applicable in the context of this thesis and it would only be possible to apply this theory in very few circumstances.

2.4.4 Vibrations, Curvature and Enhanced SO Coupling

There are several models which describe an enhanced SO coupling via either a form of coupling to, or absorption of, phonons or the intrinsic curvature of the molecules. They all offer promise in explaining the spin relaxation in organic semiconductors and how the SO plays a role even though it is presumed to be weak in comparison to the hyperfine. This section looks at these models and the potential they have to be applied to small organic molecules.

In the case of polymers a phonon-assisted spin-flip process induced by the SO coupling has been reported by Rybicki et al. where they estimate a spin relaxation rate [29, 105]. The model is EY-like in nature though as reliant on conventional band theory it may well be applicable owing to its parallels with phonon-assisted hopping. The process they report consists of two interactions. Firstly they describe an interaction with SO hamiltonian leading to a spin flip which does not conserve energy. This is then followed by the absorption of a phonon to enforce the overall energy conservation. They use perturbation theory and Fermi's golden rule to estimate a rate for the occurrence of these two interactions. In their derivation they assume the phonons in the absorption process are acoustic in nature in addition to neglecting any terms due to non-conservation of momentum arising from phonon absorption processes. They argue that in a real π-conjugated system the acoustic phonons have a broad spectrum of energies available to satisfy the energy conservation. Also they believe the momentum conservation is relaxed in π-conjugated polymers due to distortions in the polymer chain and polaronic effects which both limit the wave function extent or coherence length L of the excess carrier. Their treatment of the phonon-assisted spin-flip scattering parallels that given by Miller and Abrahams for phonon-assisted hopping and they derive an important relation for the temperature dependance (equation 2.18).

$$n_{ph} = \exp\left(-\left[E_1 - E_0\right]/k_{\mathrm{B}}T\right) \tag{2.18}$$

where E_n is the energy of the nth excited state such that the energy difference corresponds to the energy of the absorbed phonon. Rybicki et al. applied their model to obtain a value for the rate R in polyacetylene using a value for $E_1 - E_0$ of 100 meV. The result they get is in the order of 1 MHz which is smaller then the hyperfine but consistent with data published on a singly charged polyphenylene-vinylene-type polymer. Further investigation is required to determine whether the model is truly applicable in the case of small organic semiconductor molecules though

the model raises questions as to the role of phonons in spin relaxation.

As mentioned above an alternative to the phonon assisted model is one that originates from the intrinsic curvature in the molecule. These models are typically applied in the case of nanotubes and graphene sheets which are π-conjugated molecules. Their relevance to the small molecules discussed in this thesis arises from the potential to describe the effects from vibrational bending modes and the expected enhancement of the SO coupling. Indeed collaborators Fratini et al. [106] are adapting one of these models to describe a direct vibrational coupling through the absorption and emission of phonons which is mediated by the enhanced SO interaction evolving from the curvature.

This model will be described later in the section but firstly, attention must be drawn to effects of curvature and the model preposed by Huertas-Hernandos et al. in which they describe the spin-orbit interaction in graphene sheets, a material that consists of aromatic rings that are the constituents of all the small molecules considered here. They distinguish three types of contributions to the SO coupling; the intrinsic SO interaction in flat graphene, the SO coupling that originates from an external electric field and an enhanced SO interaction due to possible local curvature of the graphene sheets, i.e. ripples in the sheet [107, 108]. In order to do this they first set up a Hamiltonian to describe the intra-atomic SO coupling at two points on the sheet K and K' in terms of their wave vectors and incorporating the spinors for the π bands. They then start to consider the effects from local curvature by defining a system to have the geometry seen in figure 2.9 [109]. In the case of a curved graphene sheet, a hopping between the orbitals in the π and σ bands is induced which are also seen in figure 2.9 as red arrows.

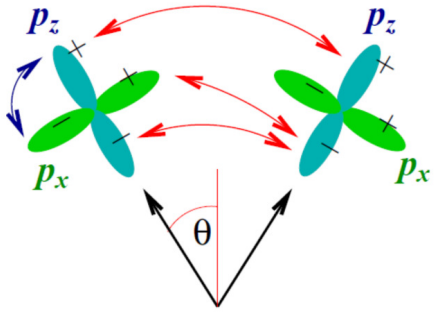

Figure 2.9: Orbitals involved in the curvature induced spin-orbit coupling and the resultant transitions between π and σ orbitals

For the simple case the curvature modifies the hopping between the two atoms compared to the flat surface for the p_Z and p_X orbitals but will not change the hopping between p_Y orbitals. They derive the (reduced) p_Z-p_X hopping to be a Hamiltonian that is the sum of three terms. They also apply the limit to θ (figure 2.9) where the radius of the curvature is much greater then the inter-atomic spacing.

They conclude that the hopping terms induced by the (intrinsic) curvature discussed break the isotropy of the lattice and lead to an effective anisotropic coupling between the π and σ bands in the momentum space. The model is then expanded for the more general curvature in the X and Y directions and they introduce two radii of curvature R_1 and R_2 which allows for an additional hopping with the p_Y orbital. After applying their model in the context of graphene they estimate numerically the coupling strength from the curvature, which is in the order of 12-15 μeV. The relation they use is given in equation 2.19.

$$\Delta_{\text{Curv}} = \frac{\Delta \cdot (V_{pp\sigma} - V_{pp\pi})}{V_1} \left(\frac{a}{R_1} + \frac{a}{R_2} \right) \left(\frac{V_1}{V_2} \right)^2 \tag{2.19}$$

It is possible using this equation to estimate the contribution of this coupling in a small molecule such as tetracene. A simple bending mode in the order of 1° along the spine can be used (a diagram of this can be seen in figure 2.10). In this case the radius of curvature $R \approx R_1$ can be evaluated using:

$$R_1 \approx \frac{360^\circ \, L}{4\pi\phi}$$

The value of L is the length of the tetracene spine and is approximately 9.7 Å, giving a Radius of curvature of 27 nm, and the inter-atomic carbon-carbon distance, a, is 1.42 Å. Given these values and the quoted values $\Delta = 12$ meV, $V_1 = 2.47$ eV, $V_2 = 6.33$ eV, $V_{pp\sigma} = 5.38$ eV and $V_{pp\pi} = -2.24$ eV the contribution from the curvature equates to $\Delta_{\text{Curv}} \approx 30$ μeV. It is worth noting that in this calculation the contribution from the curvature across the width of the rings in the tetracene is considered negligible.

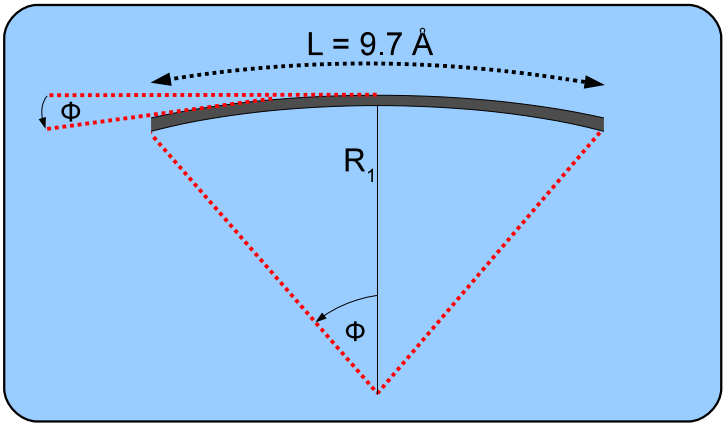

Figure 2.10: Diagram showing the construction of a simple bending mode in Tetracene

Recently Jeong et al. [110] have gone on to show that in addition to the SO contribution from the curvature that Huertas-Hernandos et al. show, there is also in fact an off diagonal coupling contribution which is in the same order of magnitude and

does not couple to the pseudo spin. They show that there are extra terms which do not come simply from the extension of the theory of curvature in carbon nanotubes but require the consideration of the different types of bending ie. twisting. They predict the relaxation rates in the region of 5-20 MHz which although not completely outrageous are still at best an order of magnitude greater then the eSR rates in the small molecules presented in this thesis. However, the numerical predictions from these theories offer promise that they could be applied to the small molecules.

The last of the models to be discussed is that being developed by collaborators Fratini et al. [109] They propose a spin relaxation mechanism that is not transport related, being active at the molecular level very much independent of the mobility of the carriers. Although their theory draws parallels with those discussed above as they state the spin relaxation is due to the strong enhancement of SO interactions in the presence of molecular (and inter-molecular) vibrational modes. The orbitals involved in their system are those discussed earlier in figure 2.9. They draw analogies to the vibronic SO coupling in previously reported photoluminescence experiments. They too use the idea that the spin-flip is accompanied by the absorption or emission of a phonon. They start with the tight binding model and much in the same vein as above they incorporate the $pp\sigma$ and $pp\pi$ character of the chemical bond to set up a hamiltonian including the curvature term. They then apply the zeeman interaction to lift the degeneracy of the spin states of the molecular orbitals. By considering the bending modes in Pentacene they solve the unperturbed Hamiltonian to extract an expression for the relaxation, in particular in the case of an additional electron as in MuSR. They go on to derive an expression to describe the temperature dependance of the eSR in the small molecules presented in this thesis. The results of this model are very promising and add to the evidence that the curvature and phonons play a vital role in enhancing significantly the SO coupling present in organic semiconductors.

Chapter 3

Samples

In this chapter I will review the properties and characteristics of some of the small molecules relevant to my PhD and this thesis and discuss the processes used in preparing the samples for the experiments performed.

3.1 Small Molecules

3.1.1 Tetracene

Tetracene is a polycyclic aromatic hydrocarbon and is a four ringed member of the Acene series. Its appearance is a bright orange powder as can be seen in figure 3.1a[111, 112]. Its chemical formula is $C_{18}H_{12}$ and it has a density of approx. 1.31 g/mol. The crystal structure of Tetracene is triclinic and its unit cell is given by a=6.05Å, b=7.84Å, c=13.01Å, $\alpha = 77.13°$, $\beta = 72.12°$ and $\gamma = 85.79°$. Campbell et al report different values to these however the most recent of the values are those given above [113, 114]. It is the herring bone style packing that promotes motion of charge carriers in the 2D a-b plane (see figure 3.1c). However, it is worth noting that Sondermann et al. report a phase transition for Tetracene at 180K which essentially rotates the molecules in to the a-c plane. This is complemented by the studies of de Boer et al. who show that the intrinsic hole mobility of $\sim$1cm^2/Vs drops rapidly below this phase transition [115, 116]. Tetracene is used in devices such as field effect transistors (FETs) and organic light emitting diodes (OLEDS). Literature on single crystal and thin film organic FETs such as the work of Goldmann et al. and Cicoira et al. report of effective hole mobilities up to 1.3 cm^2/Vs although mobilities appear to depend on growth technique and purity of the material [117–120].

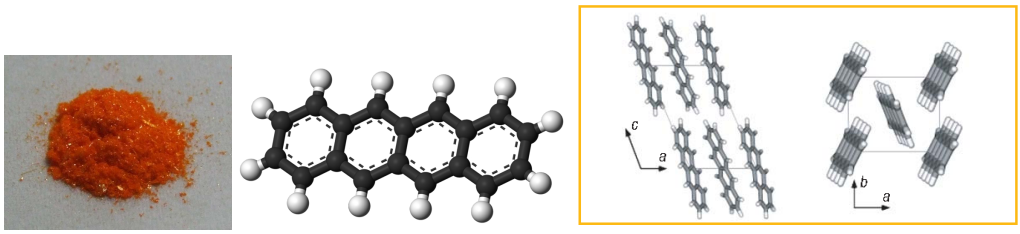

(a) Tetracene powder (b) Tetracene molecule (c) Tetracene crystal

Figure 3.1: Tetracene

3.1.2 Rubrene (Functionalised Tetracene)

Rubrene (also known as 5,6,11,12-Tetraphenyltetracene) is a derivative of Tetracene with four phenyl side groups attached to the two central rings on the Tetracene spine. Its chemical formula is $C_{42}H_{28}$ and it is bright orange in appearance (see figure 3.2 [121, 122]). Owing to its weak intermolecular bonding Rubrene exists in several phases depending on the conditions in which it is grown [123]. Taylor and Akopyan et al. report monoclinic and triclinic structures respectively although their growth methods unfortunately were not documented [124, 125]. However the more common phase of Rubrene is the orthorhombic structure for which several variations exist. Henn and Williams reported an Aba2 phase in 1971 [126] and the Bbam phase was reported later in 1983 by Bulgarovskaya and co-workers [127]. The main parameters of the unit cell are a=26.86Å, b=7.19Å and c=14.43Å at Room Temperature(RT) but on cooling from 300K to 100K these values slightly decrease due to thermal contraction [123]. Goldmann et al. [117] report FET hole mobilities for Rubrene of 10.7cm^2/Vs although Podzorov et al. [76] report that the intrinsic hole mobility is 20cm^2/Vs which is high in contrast to other organic molecules. There is a single paper that suggests there is a phase transition at about 175K which explains a rapid drop in mobility below this temperature [76].

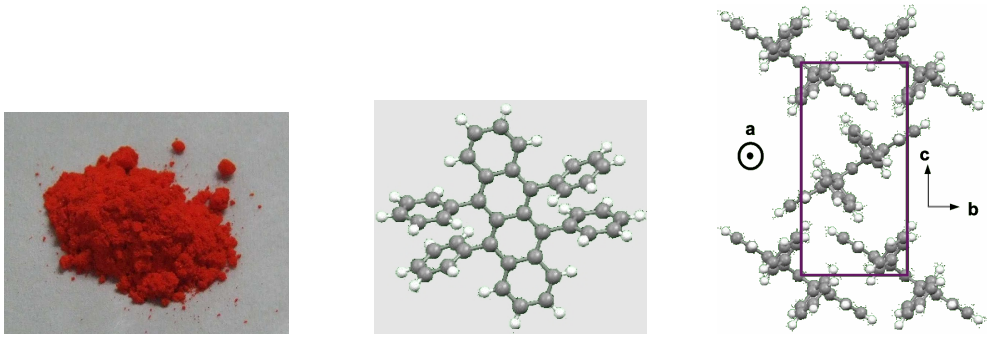

(a) Rubrene powder (b) Rubrene molecule (c) Rubrene crystal

Figure 3.2: Rubrene

3.1.3 Pentacene

Pentacene like Tetracene is a polycyclic aromatic hydrocarbon and is the next member of the Acene series. Its appearance however is the dark blue-black powder shown in figure 3.3a[121, 122]. Its chemical formula is $C_{22}H_{14}$ and it also has a density of approx. 1.3 g/mol. The crystal structure of Pentacene is also triclinic, although different polymorphs are reported. The polymorphs are characterised by their $d(001)$-spacing as this is the value which changes significantly. Mattheus et al discuss two common polymorphs with unit cell parameters a=6.29Å, b=7.69Å, c=14.41Å, $\alpha = 76.86°$, $\beta = 88.16°$ and $\gamma = 84.36°$ and a=6.27Å, b=7.78Å, c=14.45Å, $\alpha = 76.48°$, $\beta = 87.68°$ and $\gamma = 84.68°$ [128, 129]. These are a result of the growth method used and correspond to vapour deposition and growth from solution respectively. There are other polymorphs in the literature but these appear to be induced by external conditioning (heat,pressure,etc.) [114, 128–130]. Its likeness to the herring bone packing in Tetracene once again promotes motion of charge carriers in the a-b plane (see figure 3.3c). Pentacene is also used in FETs and mobilities up to 1.4 cm^2/Vs have been reported by Goldmann and co-workers [117]. In addition Jurchescu et al. report values for hole mobilities of 35 cm^2/Vs in single crystals although these are far higher then the other literature [75].

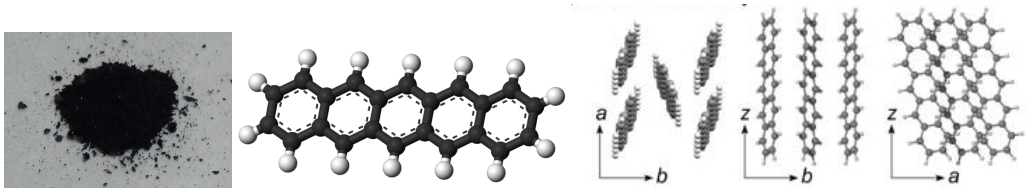

(a) Pentacene powder (b) Pentacene molecule (c) Tetracene crystal

Figure 3.3: Pentacene

3.1.4 TMS-Pentacene

TMS-Pentacene has the more technical name of 6,13-bis(trimethylsilylethynyl)-pentacene and the chemical formula $C_{32}H_{30}Si_2$. It has a chemical weight of 470.7g/mol and is the least researched of the acenes discussed in this report. The molecule and its crystal packing can be seen in figure 3.4. Anthony et al [131] report on how the crystal structure is based on a "slipped stack" layout with 1D motion along the stack. They also report how motion on the other two off-chain transport paths is much slower. In earlier studies Anthony et al. [132] also characterise the unit cell parameters to be a=5.8Å, b=10.1Å, c=11.6Å, $\alpha = 76.3°$, $\beta = 76.9°$ and $\gamma = 85.0°$ to form a triclinic cell. Sheraw et al. [133] made organic thin film transistors from TMS-Pentacene and report mobilities of $10^{-5}cm^2/Vs$. Also the work of Zhu et al. [134] on the electronic structure of functionalised Pentacene concluded an energy gap of 1.9 eV with the HOMO and LUMO situated at 4.6 and 2.7 eV respectively.

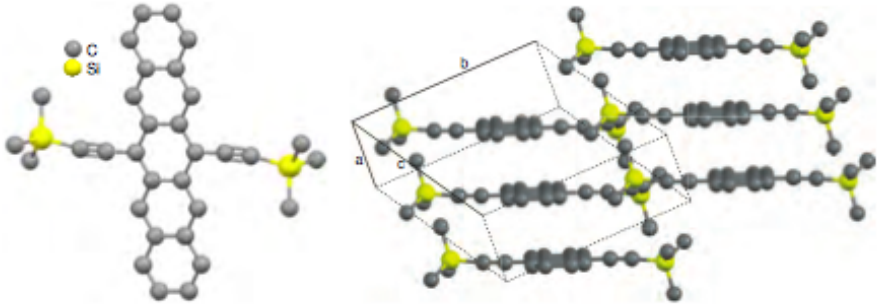

Figure 3.4: TMS-Pentacene molecule and crystal structure

3.1.5 TIPS-Pentacene

TIPS-Pentacene is more formally known as 6,13-bis(triisopropylsilylethynyl)-pentacene and has a molecular weight of 639g/mol. It has a low density of 1.1g/cm^3 and its chemical formula is $C_{44}H_{54}Si_2$. Griffith et al. [135] have carried out an in depth study in to the electrical properties in comparison to Pentacene in which they discuss its crystal packing. This can be seen along with the molecule itself in figure 3.5. TIPS-Pentacene has two structural phases with a transition at 124°C. The low temperature phase is triclinic and Chen et al. [136, 137] who carry out extensive studies in to the phase transitions and charge transport report unit cell parameters of a=7.6Å, b=7.7Å, c=16.8Å, $\alpha = 89.5°$, $\beta = 78.7°$ and $\gamma = 84.0°$. The high temperature crystal packing parameters are still however not entirely clarified. In contrast to the TMS-Pentacene the crystal structure is brick work like structure with 2 fast directions for charge transport and the work of Sheraw [133] and Payne [138] and their co-workers have determined the mobility to be between 0.4 and 1.0 cm^2/Vs. Also Anthony et al. [139] report that the transport along the b-axis is 100 times faster then the a-axis and 10000 times faster then the c-axis. There is also the advantage that when solution processed TIPS-Pentacene exhibits high mobilities.

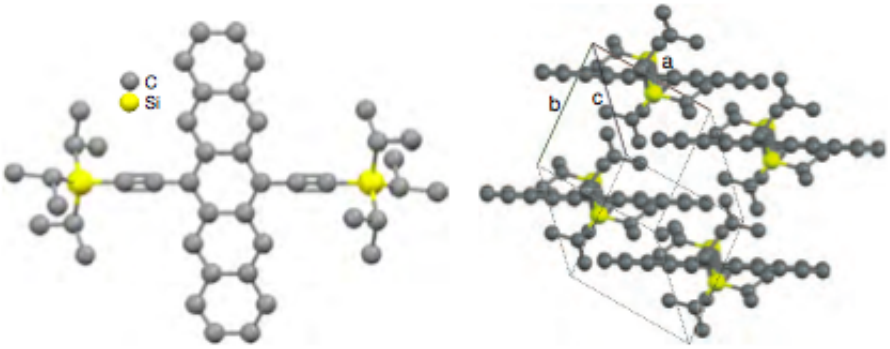

Figure 3.5: TIPS-Pentacene molecule and crystal structure

3.1.6 Triethylsilylethylnyl Series (TES-Series)

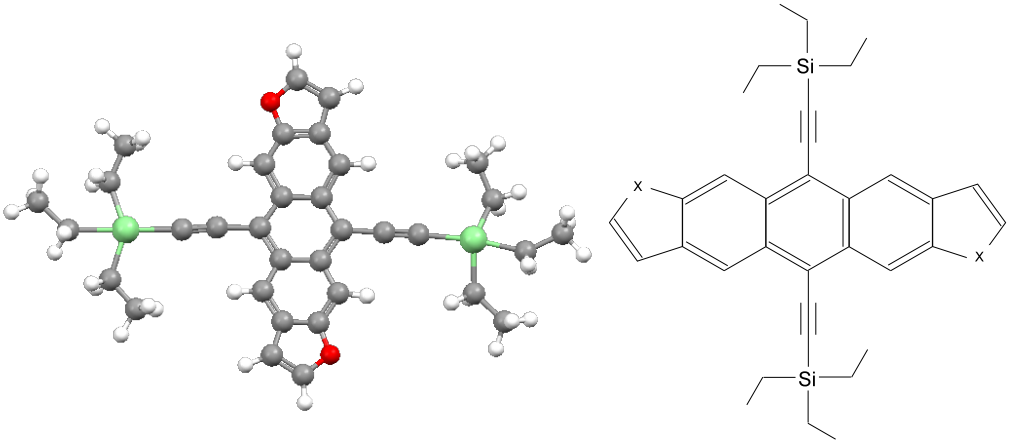

(a) TES-ADF molecule

(b) TES-ADX structure where X= O, S, Se

Figure 3.6: TES-ADX structure

In the case of the TES Series the published literature is focused on the TES-ADT molecule although one would expect the properties to be similar throughout the series. TES-ADT is more formally known as triethylsilylethynyl anthradithiophene and has a molecular weight of 484.88g/mol. Its chemical formula is $C_{28}H_{26}Si_2S_2$ and its structure can be seen in figure 3.6. The work of Payne et al describes the stability upon synthesis of crystalline Acenedithiophenes and also they report how by using solution deposition they achieve thin film transistors (TFTs) with mobilities of 1.0 cm^2/Vs [138, 140]. This is one the highest reported values for TES-ADT to the best of knowledge and the quality of the films is reported to be highly crystalline. There are also lower mobilities reported by Dickey and Lee and their co-workers however the TFTs are created by spin coating the organic layer resulting in mobilities in the order of 0.002±0.002 cm^2/Vs. They do report how, by Solvent-vapour annealing, they can improve the mobilities to between 0.11±0.09 cm^2/Vs and 0.43 cm^2/Vs [141, 142]. The change is dictated by the conditions of annealing and the solvent used and the resultant structures are finger like crystals or spherulites with maximised $\pi - \pi$ overlap. The typical crystal packing is reported to be similar to the 2D Brickwork like packing in TIPS-Pentacene and x-ray diffraction gives a triclinic space group with the parameters a=6.73 Å, b=7.25 Å, c=16.7 Å, $\alpha = 98.14°$, $\beta = 94.53°$ and $\gamma = 103.90°$ [141]. A review by Loo provides details of the properties and possibilities of these materials [143].

3.1.7 Metal-Hydroxyquinoline Chelate Series (Quinolates)

The Quinolate molecules are quite different to the Acenes as they do not have this spine type feature but instead are a more propellor like structure. Their chemical

formula is $M(C_9H_6NO)_3$ and they are essentially three hydroxyquinoline ligands attached to a metal chelate (M) (see figure 3.7a). The metal ion can be substituted of which the most common sustitution is with metals in group 3 of the periodic table. It is worth pointing out that the Thallium metal ion in this series prefers the 1-oxidation state and is less stable in the 3-oxidation state possibly owing to the bond lengths distorting the molecule [144]. This is overcome by substituting Bismuth in its III oxiation state for which, the reported structure contains water of crystalisation and so is not representative of the true crystal structure[145]. There are no reports, to the best of knowledge, on the properties of BiQ_3 and hence they are not discussed in this section. The other thing to note is that the Quinolate molecules have different phases which fit in to two polymorph groups, the *facial*-isomer and the *meridianal*-isomer. These can also be known as *cis*-isomer and the *trans*-isomer respectively. The α and β phases belong to the meridianal (mer) polymorph group and the δ and γ belong to the facial (fac) polymorph group. In appearence the mer phases have a bright yellow colour and the fac phases have a more creamy white colour (figure 3.7c [146]). The two polymorphs not only have a different appearence but also have a different rotational symmetry. The fac polymorph has a C_3 symmetry while the mer polymorph has a C_1 symmetry. Photoluminescence measurements like those reported by Cölle et al. show that the mer polymorph luminesces in the yellowy-green region and the cis polymorph luminesces in the blue region [147, 148]. T. Lee et al have carried out a detailed study in which they discuss how to transfer between the phases and the growth of phases from different solvents [149]. This is important as on purifying the material it exists in a Racemic mixture. The α and β phase have a crystal packing for which the π-π overlap dictates a helical motion of charge carriers whereas the δ and γ phases in fact minimise the π-π overlap, such that only one of the ligands overlaps with the neighbouring molecule. Cölle et al. report their studies on this crystal structure and show how the interaction is localised to two molecules effectively destroying the helical packing present in the other phases [150].

Tris(8-Hydroxyquinolinato) Aluminium (AlQ_3)

AlQ_3 is the most common molecule of the Quinolate series and since the first device made by Tang and VanSlyke in 1987 with a driving voltage of approx. 10 V it has been used frequently in OLEDs [35]. Presently, the mobilities measured in devices are typical of those measured by Dediu et al. of 1×10^{-5}cm^2/Vs [28], although Drew et al. have determined the upper limit to the intrinsic mobility, through the muon technique, to be 0.23 cm^2/Vs [151]. Its molecular weight is $\sim$459g/mol and the natural phase is the α phase although on train sublimation this phase purity is lost. Many studies of the crystal structures of the phases have been carried out such as the work of Cölle and Braun and their co-workers [146, 148, 150].

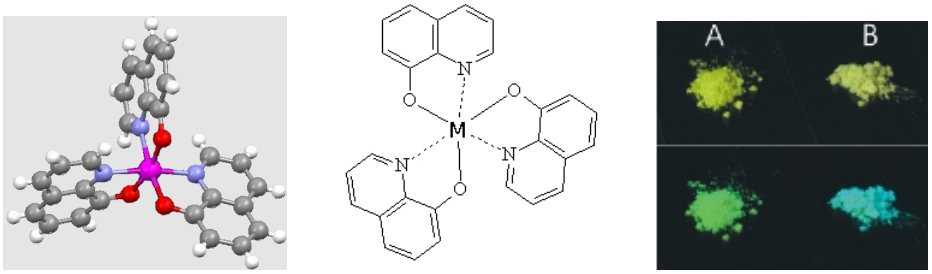

(a) Quinolate molecule

(b) schematic

(c) powder form with (bottom) and without (top) luminescing. A = mer and B = fac

Figure 3.7: Quinolates

Tris(8-Hydroxyquinolinato) Gallium (GaQ_3)

GaQ_3 is very similar to the AlQ_3 in the sense it also exist naturally in the α phase but has a molecular mass of ∼502g/mol. Wang et al. and Brinkmann et al. have characterised the phases of GaQ_3 through X-ray powder diffraction and list them in a table [152, 153]. As of yet, to my best knowledge there are no reports of mobility in GaQ_3 although given the similarities one would not expect the mobilities to be too far from those reported for AlQ_3 . However Wang et al. report a difference in energy energy levels between AlQ_3 and GaQ_3 even though their luminescence measurements are similar [154].

Tris(8-Hydroxyquinolinato) Indium (InQ_3)

InQ_3 is the last of the more stable quinolates and has a molecular mass of ∼547g/mol. It is in the naturally occuring β phase unlike the other quinolates discussed but again bares many similarities to the AlQ_3 molecule. A detailed crystal structure study using x-rays has been carried out by Sapochak and she discusses the different growth methods for InQ_3 crystals [155]. As with the GaQ_3 there are no mobility measurements to the best of my knowledge however a similarity to the mobility in AlQ_3 would be expected.

3.2 Sample Preparation

In this section the synthesis, preparation techniques and packaging of the samples used in the reported experiments will be discussed. The Quinolates were additionally purified and re-crystallised, from their as made state, to not only ensure chemical purity but also phase purity. The Tetracene and pentacene and their derivatives were not purified and were crystalline after synthesis.

3.2.1 Synthesis and Purification

The Quinolate samples except for the AlQ_3 were synthesised by the reaction of the metal chloride with the 8-Hydroxyquinoline ligand in the presence of an ammonia buffer solution. The exact method is published in [147]. The base reagents in addition to the AlQ_3 were purchased from Sigma Aldrich and the AlQ_3 was allegedly 99.9% pure. The Tetracene and Pentacene and their derivative samples were synthesised using published methods and needed no further purification on arrival. In the case of the Deuterated TIPS-Pentacene the deuteration was carried out J. E. Anthony by first preparing deuterated triisopropylsilyl acetylene as described in the literature [156]. Deuterated 6,13-pentacenequinone was then prepared from tetradeutero phthalic anhydride, which was reduced with lithium aluminum hydride, oxidized to the phthalaldehyde under Swern conditions, then condensed with 1,4-cyclohexanedione to yield the quinone. Lastly the deuterated acetylene and deuterated quinone were combined to the desired pentacene by literature methods [157].

The Quinolate samples were all purified via train sublimation. This was carried out in a 3-zone Lenton furnace in a horizontal orientation. Around 2 g of material is mounted in a borsilicate glass boat and inserted in to a borsilicate glass tube. This is heated under a vacuum of ∼3E-6 mbar to the sublimation point of the sample in steps to ensure the rate of heating is slow enough such that the sample does not degrade. There are three main impurities in the Quinolate samples discussed in this report. The first is the water in the sample as the drying process does not remove 100%. Under vacuum the water evaporates at around 80° C and so is removed from the sample long before the sublimation point of the sample. The second is excess Hydroxyquinoline that is not consumed in the reaction. The sublimation point of this is ∼120° C so like the water it is evaporated before the sublimation process. Lastly there is the by-products of the reaction which degrade at the high sublimation temperatures and therefore remain in the glass boat.

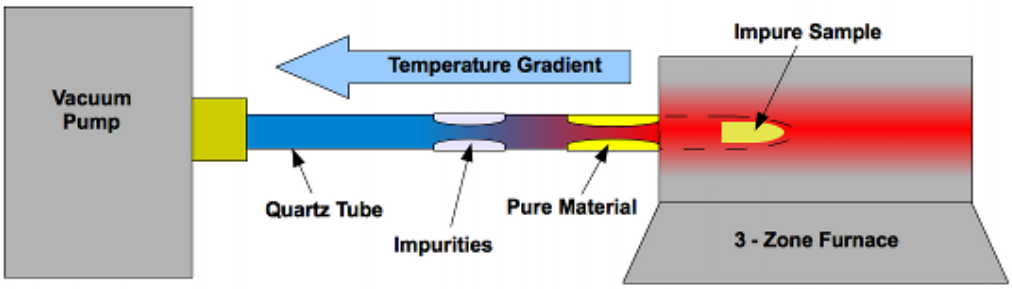

Figure 3.8: Schematic of the train sublimation process

A schematic of the sublimation process can be seen in figure 3.8. The evaporated materials are carried along the tube, which has a natural temperature gradient, towards the vacuum pump. As the material cools it is deposited along the tube. It

is worth noting here that the pure material can form in various phases dependent on the temperature at which it deposits, producing fractions along the tube. However, these can be identified using x-ray diffraction and the majority is formed in the α-phase in the case of the samples prepared in this report as the deposition temperature is around 310° C. Cölle and Brütting have produced a comprehensive review which shows the different phases and their crystallinity produced by train sublimation [158] for AlQ_3 . Also as can be seen in figure 3.8 should any of the impurities deposit on the tube the temperature gradient in the tube ensures that they are significantly further from the furnace then the pure material.

3.2.2 Re-crystalisation

As mentioned above the train sublimation process leaves the sample chemically pure but in a mixture of phases. There is literature which describes a method for phase selection that involves annealing the sample for several hours at around ∼400° [149]. However the simplest method is to recrystallise the sample from Acetone at a particular rate. This method is published by Brinkmann et al. in which the values are reported in the case of GaQ_3 for the α and β-phase. In the case of the quinolate series discussed in this report the α-phase was selected so around 800 ml of saturated solution in Acetone was evaporated at a rate of 50 ml/day [152]. The x-ray analysis confirmed that the sample was indeed in the pure α-phase and was also crystalline. The process was repeated for the AlQ_3 and InQ_3 , however, the BiQ_3 was too unstable and lacked solubility so couldn't be recrystallised. The x-ray analysis is discussed in the following section.

3.2.3 Characterisation

The phases for the AlQ_3 , GaQ_3 and InQ_3 were identified by performing a Rietveld refinement on the x-ray powder diffraction data. To carry out the measurements the samples were mounted on standard sample discs and placed in a Panalytical Xpert Pro diffractometer. A long 2θ scan was performed in the range of 5-120° to ensure all peaks were established. The data obtained is presented in figures 3.9, 3.10 and 3.11. It is worth noting at this point that the powder data is not ideal and that the peaks were no longer distinguishable above 40-50° , however phase analysis was still possible. It is apparent from the diffraction patterns that the AlQ_3 and GaQ_3 are in equivalent phases but the InQ_3 is in a different phase. The significance of this will be discussed in a later chapter. Also shown on the graphs are the results from the refinements and the difference plots (green and purple lines respectively).

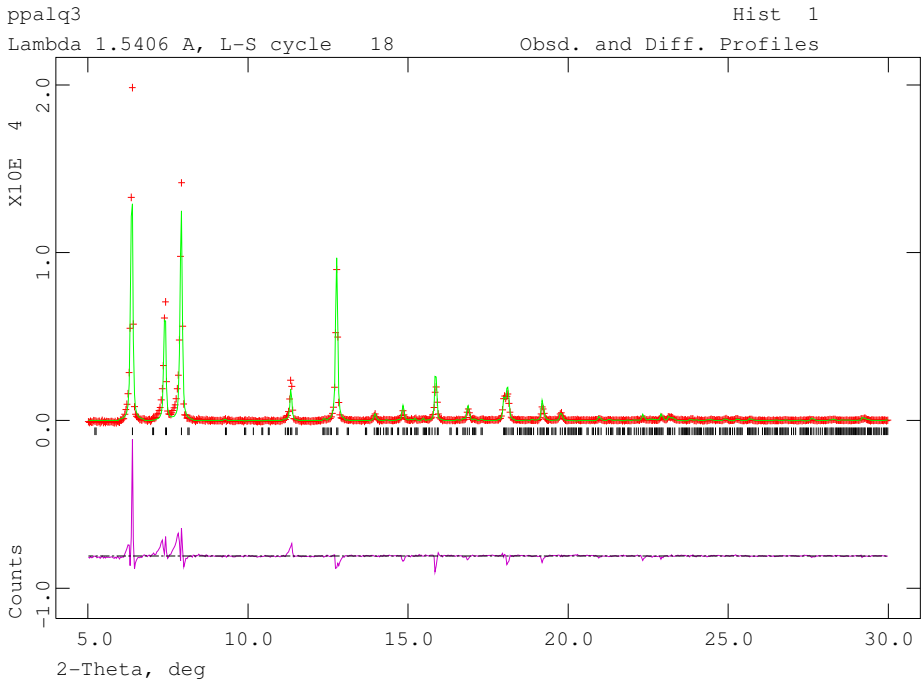

Figure 3.9: X-ray diffraction pattern of AlQ3 with refinement (green line) and difference plot (purple line)

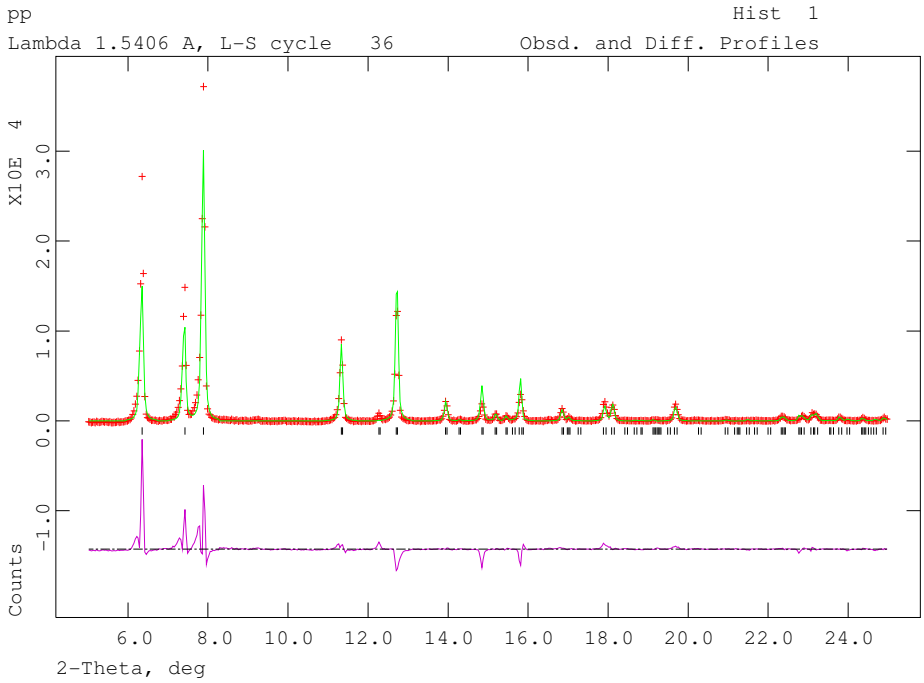

Figure 3.10: X-ray diffraction pattern of GaQ3 with refinement (green line) and difference plot (purple line)

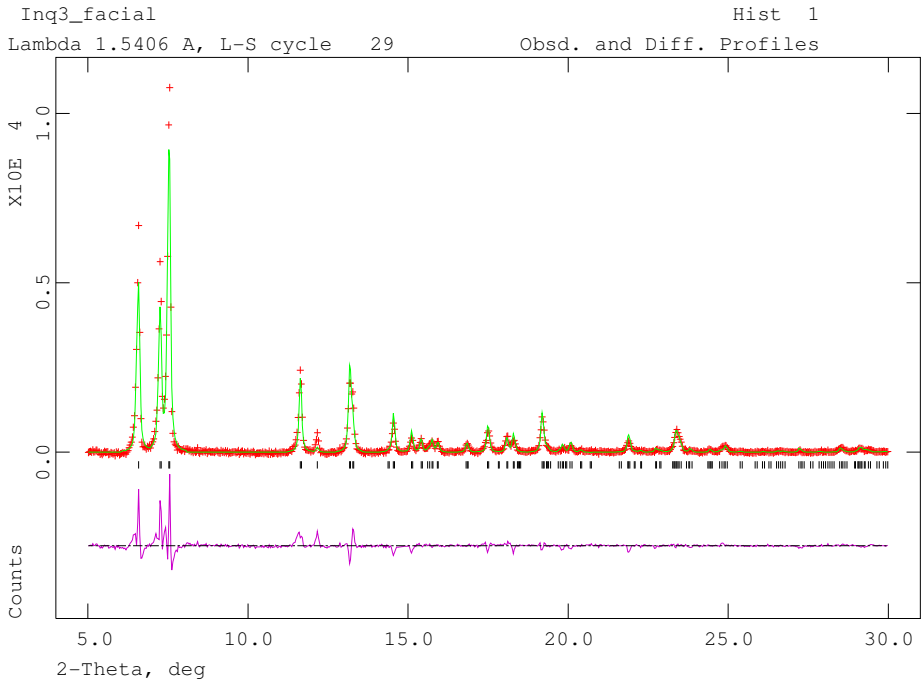

Figure 3.11: X-ray diffraction pattern of InQ3 with refinement (green line) and difference plot (purple line)

To analyse the data the software named General Structure Analysis System (GSAS) was used [159]. This software allows for a full Rietveld refinement including the background, the preferred orientation, the phase unit cell, the peak asymmetry and the grain size. In the case of the data presented here the background was fitted with a shifted chebyschev polynomial of the first kind with 8 terms. The function can be found in the handbook of mathematical functions [160] and is given by:

$$\mathbf{I}_i = \sum_{j=1}^{\mathrm{N}} \mathbf{P}_j \mathbf{T}'_{j-1} \tag{3.1}$$

where $\mathbf{T}'_{j-1}$ are the coefficients of the Chebyschev polynomial and are taken from Table 22.3, p795 of the Handbook. Each coefficient is of the form

$$\mathrm{T}'_n = \sum_{m=0}^{i-1} \mathrm{C}_m \mathrm{X}^m \tag{3.2}$$

and the values of Cm are again found listed in reference [160]. The function has a correction applied to it to make the polynomial orthogonal. This is given by:

$$\mathbf{X} = \frac{2\left(\mathrm{T} - \mathrm{T}_{min}\right)}{\mathrm{T}_{max} - \mathrm{T}_{min}} - 1 \tag{3.3}$$

This gives a final background expression of:

$$\mathbf{I}_b = \sum_{j=1}^{\mathrm{N}} \mathbf{B}_j \mathbf{T}'_{j-1} \tag{3.4}$$

where the coefficients are as above and the values of B are determined by least squares during the refinement.

To account for the polycrystalline nature of the samples the diffraction patterns were refined with an eighth order general spherical harmonic (GSH) model for the preferred orientation. The GHS was set to a cylindrical symmetry and the coefficients were allowed to vary. This model is implemented in GSAS by Von Dreele [161] using the general axis equation as described by Bunge [162]. In this formulation the preferred orientation correction, Op(h,y) is dependent on both the reflection, h, and on the sample orientation, y. The general axis equation is given by

$$\mathbf{O}_p(\mathrm{h},\mathrm{y}) = 1 + \sum_{\mathrm{L}=2}^{\mathrm{N_L}} \frac{4\pi}{2\mathrm{L}+1} \sum_{m=-\mathrm{L}}^{\mathrm{L}} \sum_{n=-\mathrm{L}}^{\mathrm{L}} \mathrm{C}_{\mathrm{L}}^{mn} \mathrm{K}_{\mathrm{L}}^{m}(\mathrm{h}) \mathrm{K}_{\mathrm{L}}^{n}(\mathrm{y}) \tag{3.5}$$

$\mathrm{K}_{\mathrm{L}}^{m}(\mathrm{h})$ and $\mathrm{K}_{\mathrm{L}}^{n}(\mathrm{y})$ are two harmonic terms. They have values according to the crystal and sample symmetries, respectively, and hence the two inner summations are only over the resulting unique, nonzero harmonic terms. GSAS automatically selects these terms given the space group symmetry and the sample symmetry chosen by the user. The available sample symmetries in GSAS are cylindrical symmetry, 2/m, mmm and no symmetry and the selection of harmonic coefficients is strongly affected by the choice of sample symmetry. In the case of cylindrical sample symmetry (or fibre texture), as used in the refinements reported, only the $\mathrm{K}_{\mathrm{L}}^{0}(\mathrm{y})$ terms are nonzero. This means the rest of the terms can be excluded from the summations and the set of $\mathrm{C}_{\mathrm{L}}^{m0}$ coefficients should be sufficient to describe the effect on the diffraction patterns due to texture.

The results from the Rietveld refinement are reported in table 3.1 for each of the Quinolates. The AlQ_3 and GaQ_3 were found to be in the pure *mer*-α phase reported by Brinkmann et al. [152] and as expected from the re-crystallisation process however the InQ_3 was in the rare *fac*-γ phase [163]. The phase analysis showed that although the InQ_3 was in a different phase it remained pure. There is a difference in the intensities which could be down to two possibilities. The first is that the preferred orientation is not correctly fitted and the second possibility is that the sample contains a small amount of impurities. However the refinements are very reasonable given the quality of the powder diffraction data and the values are in close agreement with the published data seen also in the table.

Table 3.1: X-Ray powder diffraction refinement results compared to published values

	Quinolate Phases					
Crystal Data	**AlQ_3**	**Ref. Data**	**GaQ_3**	**Ref. Data**	**InQ_3**	**Ref. Data**
emperical formula	$C_{27}H_{18}N_3O_3Al$	$C_{27}H_{18}N_3O_3Al$	$C_{27}H_{18}N_3O_3Ga$	$C_{27}H_{18}N_3O_3Ga$	$C_{27}H_{18}N_3O_3In$	$C_{27}H_{18}N_3O_3In$
fw	459.43	459.43	502.17	502.17	547.26	547.26
crystal structure	Triclinic	Triclinic	Triclinic	Triclinic	Triclinic	Triclinic
space group	P -1	P -1	P -1	P -1	P -1	P -1
a, Å	6.2599(12)	6.2455(10)	6.2607(13)	6.27	6.1992(12)	6.1860(12)
b, Å	12.8548(9)	12.8710(18)	12.8704(10)	13.0	13.4518(9)	13.436(3)
c, Å	14.8124(7)	14.739(3)	14.8801(8)	14.8	14.7488(9)	14.725(3)
α, deg	69.697(5)	69.890(6)	110.474(5)	110.0	65.737(5)	65.63(3)
β, deg	89.255(15)	89.464(5)	89.213(13)	89.2	88.148(14)	88.15(3)
γ, deg	82.667(20)	82.520(13)	97.577(15)	98.0	83.555(15)7	83.55(3)
V, Å^3	1108.11(24)	1102.309	1112.78(22)	1123	1114.06(22)	1107.7(4)
Z	2	2	2	2	2	2
temp, K	300	300	300	300	300	293
λ, Å	1.542	1.542	1.542	1.542	1.542	1.542
2θ range, deg	5-120		5-120	5-80	5-120	1-26.7
R Factor	0.1101	0.1091	0.1310	0.1090	0.0931	0.050

3.2.4 Sample mounting

The samples are conventionally mounted in a silver packet made from 25 μm thick silver foil. The silver is 99.9% pure and the profile is well characterised in a muon beam.

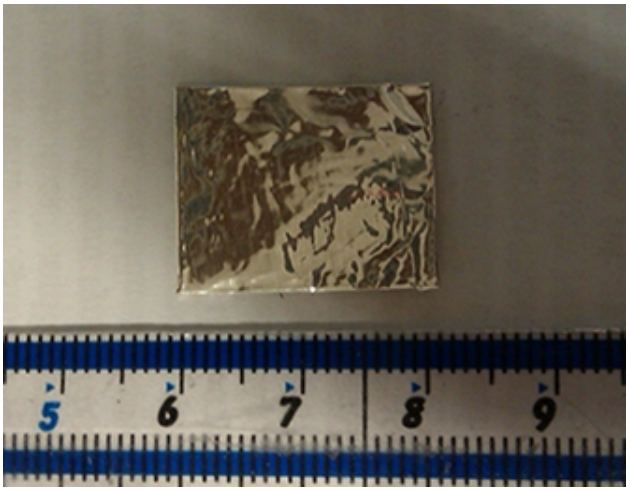

Figure 3.12: Example of silver packet used in experiments compared with a centimetre rule

An example of the packet used is sown in figure 3.12. The Quinolate series were all mounted in packets that were ~17 X 17 mm in size. Around 800mg of the phase pure powder form of the sample was loaded in to the packets. The TES-Series were loaded in different sized packets as the mass of sample available varied. Around 100 mg of TES-ADF was mounted in a packet 25 X 17 mm in size. The TES-ADT weighed 60 mg and had a packet size of 15 X 12 mm. Lastly in the series, the TES-ADS weighed 50 mg and was in a packet measuring 20 X 15 mm. The TIPS-Pentacene was mounted in two ways dependent on the experiment performed. In the case of the standard ALC measurement around 115 mg of the sample was mounted in a packet measuring 15 X 25 mm. However, in the electric field experiments the TIPS-Pentacene was pressed in to a disc that had a diameter of 13 mm and a thickness of 2 mm. Finally the DTIPS-Pentace was mounted in a packet 15 X 20 mm that weighed ~120 mg. Occasionally additional silver foils are placed in front of the packet when mounting to act as "degraders". This ensures that the muons are stopping in the sample by reducing their momenta. Also the mounting plate was adapted in the E-Field experiment to the design shown in figure 3.13. The main Al plate is grounded and the sample is electrically contacted to this plate. A ±5 kV electric field can be applied through the sample via the titanium contact sheet. The teflon spacer prevents any shorting between the two contacts.

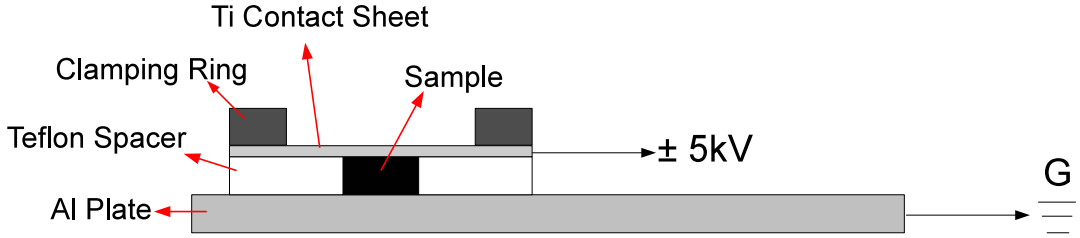

Figure 3.13: Side profile design of E-Field sample mount

Chapter 4

Muon Spectroscopy

4.1 The Muon and Muon Production

The muon is part of the lepton family and is like an electron except it has a mass of 105.7 MeV/c^2 which is 200 times that of the electron. It is a subatomic particle with spin 1/2 and it has a half life of 2.2 μs. Since its first discovery by Neddermeyer and Anderson in 1937 [164] the production of the muon has come a long way, now being provided by particle accelerators in addition to the cosmic ray. Like the other particles in the lepton family the muon has an antiparticle with the same spin but the opposite charge. There are 4 main facilities that produce muons which are ISIS in Oxfordshire UK, the Paul Scherrer Institute (PSI) in Villigen Switzerland, the Tri-University Meson Facility (TRIUMF) in Vancouver Canada and there is a new muon facility being built in Japan. The muon decays from the pion which is produced from the collision of a proton in to a nucleus. In muon facilities this is done by accelerating protons in a synchrotron or cyclotron and colliding them in to a target which is typically graphite, owing to its low proton number which is ideal for high pion production. This target is stationary at ISIS compared to the rotating targets at PSI which will be discussed further later. The pions at rest then decay emitting muons with 4.1MeV of kinetic energy as shown in figure 4.1. It is worth noting only the muons near the surface have enough energy to escape the target and hence are named surface muons. These muons are always positive and most importantly 100% spin polarised. There is another type of muon that is obtained from the pions which are called decay muons. This is due to the fact that negative pions with sufficient energy escape the target and decay in to either backwards or forwards muons (their momenta is anti-parallel or parallel to that of the pion respectively). These muons are either spin polarised positive muons or negative muons of a broad momentum distribution. Eaton and Kilcoyne give a comprehensive discussion of the muon production methods and also present the less common pion decay channels [165]. The muon also undergoes Larmor precession in

a magnetic field. This is discussed by De Renzi [166] and Blundell [167] in which they present the relationship between the precession frequency and the magnetic field in terms of the gyromagnetic ratio (equation 4.1).

$$\omega = -\gamma B \tag{4.1}$$

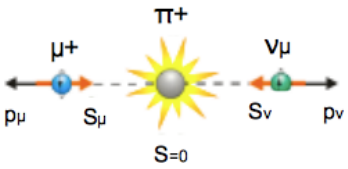

Figure 4.1: Surface pion decay

4.1.1 Pulsed ISIS Source

ISIS (figure 4.2) is currently the only pulsed muon source and it uses a synchrotron to accelerate the protons. The first muon beam commissioning reported by Eaton and co-workers [168] was in 1987 and it is now one of the leading muon facilities in the world. The proton beam provided by the synchrotron runs at a current of ∼200 μA and is accelerated to an energy of 800MeV by first linearly accelerating negative hydrogen ions to 37% of the speed of light and then stripping the electrons off to feed the synchrotron. The electrons are stripped away by passing the beam through 0.3 μm thick Aluminium foils. In the synchrotron the protons are accelerated to 84% of the speed of light in approx. 10000 revolutions from which they are guided to a target 10mm thick, to produce muons. There are two main muon facilities at ISIS, the Riken-RAL Japanese facility with 4 beam ports and the European facility with 3 beam, ports. The typical layout of the muon beam line is shown in figure 4.2.

The time structure at ISIS is a double pulse structure as the accelerator runs at twice the frequency of the pulse frequency which is 50MHz and so two bunches of protons are accelerated at one time. The width of each sub-pulse is approx. 70ns at FWHM and the separation of the pulses is 320ns (see figure 4.3). The technical details are published on the ISIS webpage [169] and also can be found in reference [165].

ARGUS Beamline

The Riken-RAL facility at ISIS houses the Advanced Riken General-purpose MuSR spectrometer. The instrument has 192 detector segments and allows for a single pulse mode although this reduces the event rate. It is for this reason the mentioned double pulse structure is commonly preferred. The data rate for the standard double pulse mode can range up to 70 million events per hour. The longitudinal field range

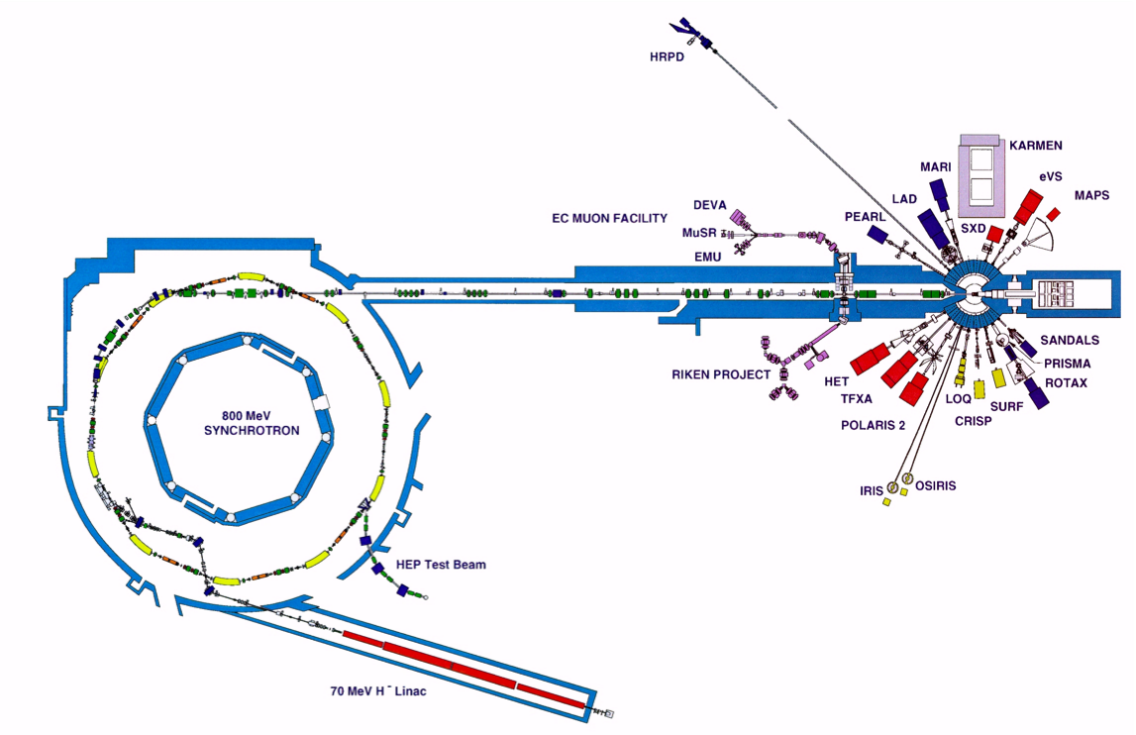

Figure 4.2: ISIS muon beam (note DEVA is now HIFI)

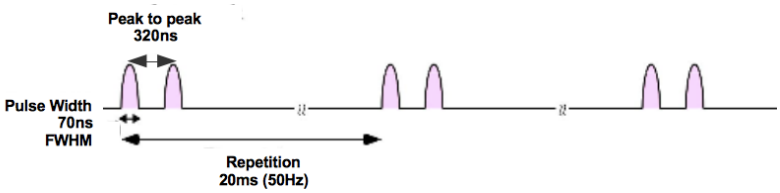

Figure 4.3: Double pulse structure

of the instrument is between 0 and 0.395 T and in addition there is a transverse field magnet providing fields between 0 and 15 mT. The accuracy of the zero field is < 0.01 mT. For the purpose of all the measurements taken, a flow cryostat operating at a temperature range of 5-300 K was used. The background contamination of the instrument is $< 10^{-5}$ of the highest muon rate resulting in the signal being indistinguishable at times higher than 25 μs. Hence this limits the time window to around 30 μs with a time resolution determined by the proton bunch pulse width. The width of the beam spot is adjustable in the range of 10-50 mm.

HIFI Beamline

ISIS has a High Field muon instrument denoted HIFI which operates with a longitudinal field range of 0-5 T and transverse field up to 10 mT. The magnetic fields are provided by a superconducting magnet and have an additional low longitudinal field (¡40mT) modulation or sweep capability. The instrument has an event rate in the region of 40-45 million events per hour with a time window of 30 μs. The double pulse is divided between three instruments resulting in a single pulse shared between

the HIFI and EMU instruments. Hence the instrument operates in a half pulse mode only with a background contamination in the same order as ARGUS. A Closed Cycle Refrigerator (CCR) was used providing a temperature range of 10-600 K. The beam spot size can be adjusted between 10-27 mm horizontally.

EMU Beamline

EMU is a new 96-detector μSR spectrometer which is optimised for zero field and longitudinal field measurements. A longitudinal field of up to 0.5 T can be applied and also the coils allow for a transverse field to be applied with a range of 0-15 mT. The beam spot is adjustable within a FWHM range of 10-27 mm by the use of adjustable slits. The data rate at optimum operation is in the order of 55 million events per hour with a time resolution of down to 2 ns and a measurement window of $\sim$30 μs. As in the HIFI spectrometer the double pulse is divided between spectrometers giving the half pulse. The CCR cryostat was used providing a temperature range of 12 K - 600 K.

4.1.2 Continuous PSI Source

The Swiss Muon Source (SμS) at PSI has a cyclotron providing protons with a beam energy of around 590MeV. The 2.2 mA proton current, 10 times that of ISIS, is directed to a target as in the ISIS facility and undergoes much the same pion decay processes. One of the main differences is that PSI operates multiple rotating targets to improve the quantity of muons produced and to reduce damage to the target. This method does have the disadvantage that the muons are scattered more in the target and additional collimation and slits in the target wheel are required [170, 171]. The target can be seen in Figure 4.4

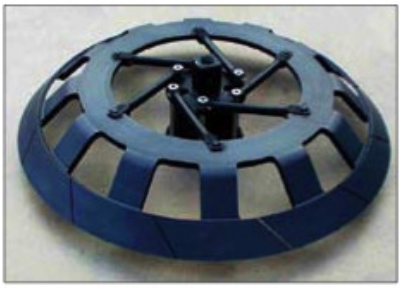

Figure 4.4: PSI rotating target

There are $10^7 - 10^8$ muons being produced every second which are guided to the muon instruments in a quasi continuous beam. The event rate that can be achieved at PSI is quite low as the detection system only allows for one muon arriving at a time compared to the bunch at ISIS. This is on the one hand a major limitation,

but on the other hand a great advantage because the time resolution is far greater as the muon has a definite arrival and decay time. This allows for higher frequencies to be measured in a system, especially the organic semiconductors with hyperfine frequencies in the range of tens or hundreds of MHz. It has the ability to see much faster relaxation rates that would not be visible at ISIS. The technical details for reference are published on the institute homepage [172].

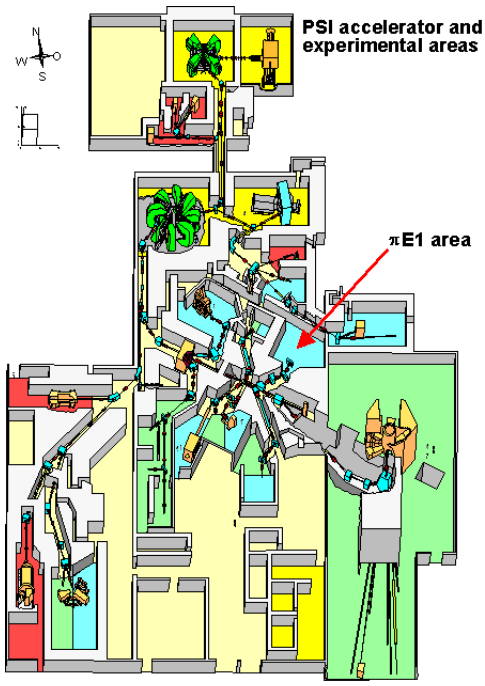

Figure 4.5: PSI Schematic

GPS Beamline

GPS is an acronym for the General Purpose Surface muon instrument at PSI. GPS has two magnets, a primary and auxillary one, denoted WED and WEP respectively. The primary magnet is commonly operated in the field range of 0.03-0.6 T. For fields below 0.03 T a separate power supply is used. The auxillary magnet can provide a field of up to 10 mT in a perpendicular direction to the main field. It is used with the spin rotator switched off to determine the instrument and experiment parameters. The earth's magnetic field along with any stray fields are compensated for so measurements in zero field are possible. The standard cryostat used is a continuous flow Helium-4 evaporation cryostat and can provide temperatures in the range of 1.6-320 K.

The GPS specification [172] shows that the spin polarization of the muons, coming from the 5 mm thick graphite target, is greater than 95% and hence maintained throughout the transfer to the instrument. There are five possible detectors, with respect to the direction of the beam, that can be used depending on the field setup needed. These are the forward, backward, up, down and right detectors and do not

need the detector array like ISIS. In the longitudinal field mode the forward and backward detectors are needed to detect the positrons compared with the up, down and right in the transverse field mode (> 100 G). To switch between longitudinal and transverse modes a spin rotator is needed as the orientation of the magnet cannot be changed so instead the direction of the muon spin direction is rotated. The spin rotator comprises of overlapping magnetic and electric fields. The magnetic field is responsible for the 60° rotation of the spin and the high voltage electric field for the conservation of momentum. This results in only a fraction of the muons spin polarisation being used as there remains a longitudinal component to the spin. There is also a veto mode for the longitudinal configuration in which the forwards detector is used to discount muons which do not hit the sample reducing the detectable area. This reduces substantially the background but also the event rate and so is compromise between the two. However, veto mode does allow for the use of very small samples.

ALC Beamline

ALC is the Avoided Level Crossing removable spectrometer at PSI. It has a superconducting magnet which allows for fields in the range of 0-5T and its detectors consist of 20 positron counters arranged in two rings. The spectrometer can be used in two modes, time integral and time differential, depending on the measurement needed. The time integral mode allows for much higher data rates in the region of 90-210 million events per hour and is suited to an ALC measurement. However this mode can only be used in the longitudinal field setup and does not offer the low background and high time resolution that is possible in the time differential mode. The muon rate in the time differential mode is in the order of 30 million events per hour and the time resolution is 1.2 ns. To enable the transverse field ALC uses a spin rotator like that of GPS but with a rotation of 42° and the positron counters are grouped accordingly. The polarisation is about 90% for the longitudinal field and as in GPS the percentage is reduced to 60% for the transverse field. The beam can be collimated within the range of 10-20 mm. The standard cryostat is the Janis Helium-flow cold-finger cryostat which allows a temperature range of 3-470 K.

4.1.3 Muon Implantation

Muons hitting the sample implant at a certain depth depending on energy, density of the sample and thickness of degraders before the sample. Monte Carlo simulations can be done to calculate the muon implantation depth however in the case of the surface muons, with a momentum in the range of 20 to 80 MeV, the implantation

depth has the relation presented by Eaton and Kilcoyne [165]

$$R = ap^{3.5}$$

where a is the constant encompassing the mass density and composition of the sample and p is the muon momentum. There is also a straggling effect giving a width to the implantation depth which arises from the statistical nature of the muon's energy loss and the slight spread in the momentums of the arriving muons. This width is given by ΔR and has the following relation.

$$\Delta R = a\left[0.008 + 12.25\left(\frac{\Delta p}{p}\right)^2\right]^{\frac{1}{2}} p^{3.5}$$

Muons arriving in the sample lose their energy in a many stage process which includes ionisation, thermalisation and collisions. This is illustrated in figure 4.6 with the characteristic time scales.

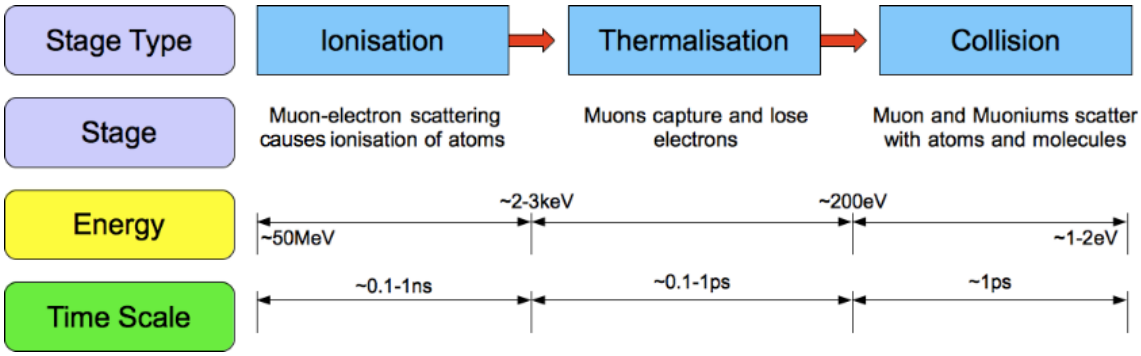

Figure 4.6: The muon's energy loss processes in a sample while spin is conserved throughout

Nagamine [173] describes how the surface muons come into the sample with an energy up to 52.8 MeV and go through many processes quickly losing their kinetic energy. They firstly scatter off electrons which then ionise in the sample and leave the muons with an energy of around 2 keV. Then typically on the picosecond scale they rapidly capture and lose an electron until their energy is decreased to a few hundred eV. The result of capturing an electron is the formation of an atom called Muonium which is a Hydrogen like atom containing a positive muon with an orbiting electron. Although the hyperfine coupling from the formation of this Muonium changes the spin precession slightly the overall change to the spin polarisation is negligible and essentially preserved. The last stage in the muon's energy loss has two models. The first model is that the muons form a permanent Muonium, having reached the collision stage, and lose their remaining energy through scattering with atoms and molecules but preserving the Muonium. This is called the epithermal model and by using low energy muon Morenzoni [174] and Prokscha et al. [175] have carried

out in depth studies. The second model is where the muons continue to capture and lose electrons to form either stable Muonium or remain free muons but at low energies. This is called the spur model and studies of how the model works have been carried out by Gorelkin [176] and Eshchenko [177] and their co-workers. In both models the muons lose their energy either through elastic or inelastic collisions to the surrounding medium. Nagamine [173] presents the case where they are elastic collisions where as Blundell [167] discusses the case of the inelastic collision. Both of the models occur with negligible loss to the spin polarisation on the time scale of nanoseconds.

In an organic material in the epithermal model the Muonium can undergo a final stage in which they bond with the molecules in the sample. Unsaturated bonds and aromatic rings provide sources of high electron densities for the Muonium to bond to. Studies by Percival et al. [178] show that, in the case of the liquids, it is 1000 times less effective for the muonium to join to a saturated bond and this is supported by Walker in his book [179] in which he explains that the reaction would be over before a muon experiment even starts. This is different to how the spur model would work. In this case the muon leaves behind many electrons on its path to the molecule to which it forms a bond. The bond creates a positively charged molecule which the electrons are attracted to. One of these track electrons neutralises this charge by adding to the molecule. Although no direct evidence to prove either model to the best of knowledge has been presented, the studies of Siebbeles [180] and Walker [181] and their co-workers, both with experiment and simulations, show in the case of liquids the spur model is no longer relevant. Also the work of Storchak et al. [182, 183] in which they study both liquids and solids, highlights the importance in the case of solid semiconductors and rare gas solids of Muonium formation due to charge transport.

4.1.4 Muon Decay

The muon decays in to an electron or positron (depending on its charge) and two neutrionos via the weak decay as shown in figure 4.7a. This is the dominant decay chanel and the distribution of electrons can be described by a set of parameters called the Michel parameters after Louis Michel [184]. In the case where $\theta = 0$ is the direction of the muon spin, the spatial distribution $\mathrm{W}(\theta, \eta)$ can be given mathematically [185] by

$$\mathrm{d}^2\mathrm{W}(\theta,\eta) = \tau_\mu(3-2\eta)\eta^2\left[1+\frac{2\eta-1}{3-2\eta}\cos\theta\right]\mathrm{d}\eta\mathrm{d}(\cos\theta) \tag{4.2}$$

where η is the ratio between the emitted positrons kinetic energy to the maximal kinetic energy $\mathrm{E}/\mathrm{E}_{max}$ and θ denotes the angle between the positron momentum

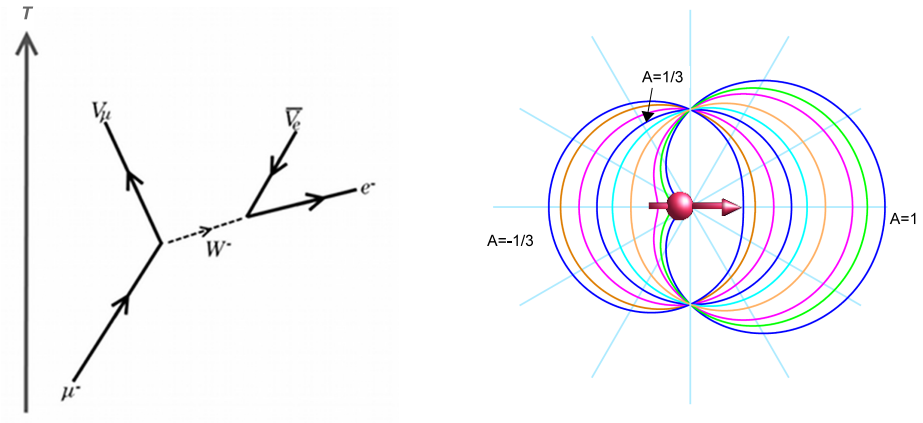

(a) Muon decay feynman diagram

(b) Muon decay spacial distribution

Figure 4.7: Muon decay

and the muon spin. This decay is studied in depth by Bardon et al. and by Kuno and Okada [186, 187]. A graphical representation of the decay distribution is shown in figure 4.7b. In equation 4.2 the coefficient of the cosine term describes essentially the asymmetry in the spatial decay of the muon and can be written as:

$$a(\eta) = \frac{2\eta - 1}{3 - 2\eta} \tag{4.3}$$

Taking the average over all the possible energies produces an asymmetry of $a = 0.33$ and if integrated over $\cos\theta$ equation 4.2 gives the energy spectrum equation

$$\mathrm{dW}(\eta) = 2\tau_\mu(3 - 2\eta)\eta^2 \mathrm{d}\eta \tag{4.4}$$

The way that the muon decays such that the positron direction is tied in to the spin plays a fundamental role in MuSR.

4.2 Experimental Aspect

4.2.1 Geometry

In a typical muon experiment there are an array of detectors surrounding a sample which is in line with the muon beam. The convention used commonly is that the initial muon spin is pointing towards the back detector, the opposite direction to which its initial momentum is directed. The number of events at a given time on a detector is proportional to the exponential decay of the muon.

$$N_{B,F}(t) \propto e^{(-t/\tau_\mu)}$$

The way in which the detectors are set up means that there is an intrinsic asymmetry due to the spatial disribution function discussed earlier (equation 4.2). This is described by

$$1 \pm A(t)$$

There are also differences in the efficiencies of the detectors due to several reasons such as the sample being off center, the intrinsic efficiency differences in individual detectors and the difference in areas of the two detectors. This is all combined in to one parameter ($\epsilon_{B,F}$). Lastly there is an average background on each detector denoted $BG_{B,F}$. Therefore the final equation describing the number of events on a detector at any given time is that given by Brewer and Cywinski [188].

$$N_{B,F} = BG_{B,F} + N^0_{B,F}\epsilon_{B,F}e^{-t/\tau_\mu}[1 \pm A(t)] \tag{4.5}$$

where N^0 is simply a normalisation constant. It then follows that

$$N_B(t) = BG_B + N^0_B\epsilon_B e^{-t/\tau_\mu}[1 + A(t)]$$

and

$$N_F(t) = BG_F + N^0_F\epsilon_F e^{-t/\tau_\mu}[1 + A(t)]$$

The experimental asymmetry is defined as

$$a(t) = \frac{[N_B(t) - BG_B] - [N_F(t) - BG_F]}{[N_B(t) - BG_B] + [N_F(t) - BG_F]}$$

If the case of vanishing backgrounds is taken, then the following approximations can be made

$$a(t) = \frac{[N_B(t) - N_F(t)]}{[N_B(t) + N_F(t)]}$$

Substituting in and redefining the efficiency for convenience as $\alpha = \epsilon_B N^0_B/\epsilon_F N^0_F$ then the asymmetry becomes

$$a_0(t) = \frac{\alpha N_B(t) - N_F(t)}{\alpha N_B(t) + N_F(t)}$$

Lastly if a further assumption is made that $A(t) = A_0P(t)$ then the asymmetry an be reduced to

$$a_0(t) = A_0(t)P(t) = A(t)$$

This implies that once α and the background have been determined then all the relevant information is in the forward-backward asymmetry function $A(t)$.

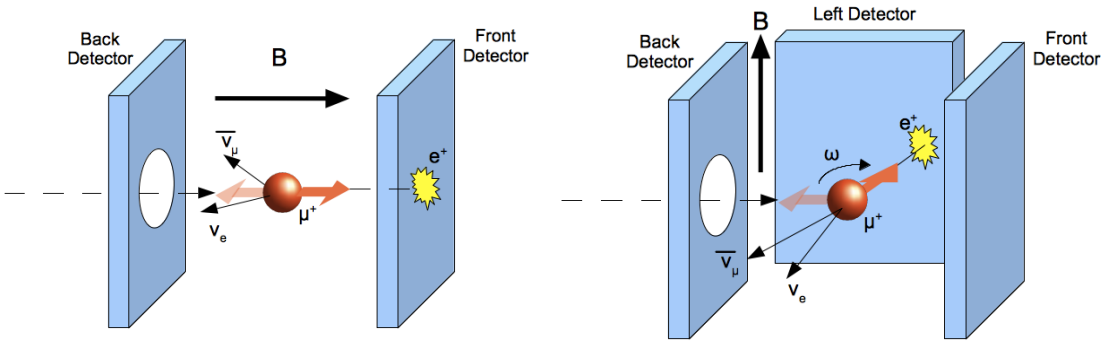

(a) Longitudinal Field MuSR setup (b) Transverse Field MuSR setup

Figure 4.8: MuSR experimental geometries

Longitudinal Field Geometry

The principle of the longitudinal field geometry (LF) is shown in figure 4.8a where the field is applied anti-parallel to the direction of the initial muon spin. The light coloured arrow shows the initial spin direction and the dark arrow the direction at time t. Muons with 100% spin polarisation enter the sample space through the back detector and their momentum is in the direction of the forward detector anti-parallel to the magnetic field. As the muon enters the sample, if there are internal fields such as local magnetic fields or modulating hyperfine fields then the spin direction is altered. As the direction of the positron emission is tied in to the muons spin direction then the emission distribution is also altered. After a time t a proportion of the spin ensemble has depolarised and reduced the initial spin polarisation. The way in which the functional shape of A(t) arises is dependent on the nature of the relaxation.

Transverse Field Geometry

In this case the field is applied perpendicular to the initial direction of the muon spin. The basic idea can be seen in figure 4.8b in which as before the lighter arrow is the initial spin direction and the darker arrow the spin at time t. The applied field causes the muon to precess around its axis with a precession frequency ω and the result is an oscillation of the spin ensemble. There is also a π-shift in the detectors which causes an oscillation in the front-back asymmetry. The asymmetry has the form

$$A(t) = G(t)\cos(\omega t + \phi_0)$$

where $G(t)$ is the relaxation function and $\phi_0$is the phase difference between the initial muon spin direction and that of the primary detector axis. It is important to note that the frequency ω depends on the type of muon (free muon, free muonium or bound muonium) and also on the local magnetic field. For the free and isolated

Muon/Muonium the frequencies are respectively [173]:

$$f_\mu = 135.53 \frac{\text{MHz}}{\text{T}} \times B$$
$$f_{Mu} = 13940 \frac{\text{MHz}}{\text{T}} \times B$$

The second of these is valid for the triplet state Muonium as the singlet state muonium has a precession frequency which is far to high to be observed.

Chapter 5

Physics of Muonium

After the formation of muonium the HFI couples the muon and the electron together. The strength of this coupling can be modulated by the external magnetic field. This chapter presents the time dependent behaviour of the coupled system in an externally applied magnetic field. Firstly the case of the Isotropic Muonium is studied and then this is extended to incorporate the more complex case with anisotropy. The next section then introduces a special case in Muonium physics called an Avoided Level Crossing (ALC). It is shown that the ALCs provide an extremely sensitive probe of the Muonium and its environment, including the electron spin dynamics. Lastly the behaviour of the system in an applied transverse magnetic field will be presented.

5.1 Muonium in a Longitudinal Applied Magnetic Field

5.1.1 Isotropic Muonium

The first case of muonium to consider is isotropic muonium and in isolated muonium the system is described by an isotropic HFC (A) alone. Blundell [189] shows in his work on electronic properties of molecular conductors using spin rotation that the equation 2.16 is extended to include the Zeeman terms from the interactions between the magnetic field and the muon and electron spins and becomes

$$H_0 = -\gamma_\mu \vec{S}_\mu \cdot \vec{B} + \gamma_e \vec{S}_e \cdot \vec{B} + A\vec{S}_\mu \cdot \vec{S}_e \tag{5.1}$$

Blundell [189] shows how this coupled two-spin system can be calculated using the four dimensional spin operators. He gives the eigenvalues for the energy which are as follows:

$$E_1 = \frac{\hbar}{4}\left[A + 2B(\gamma_e - \gamma_\mu)\right] \tag{5.2}$$

$$E_2 = -\frac{\hbar}{4}\left[A - 2\sqrt{A^2 + B^2(\gamma_e + \gamma_\mu)^2}\right] \tag{5.3}$$

$$E_3 = \frac{\hbar}{4}\left[A - 2B(\gamma_e - \gamma_\mu)\right] \tag{5.4}$$

$$E_4 = -\frac{\hbar}{4}\left[A + 2\sqrt{A^2 + B^2(\gamma_e + \gamma_\mu)^2}\right] \tag{5.5}$$

Figure 5.1 shows the energy levels plotted against an applied longitudinal field for the case of isolated muonium. The two spin system can exist in two different states, a triplet or a singlet. These are the energy levels E1-E3 and E4 respectively.

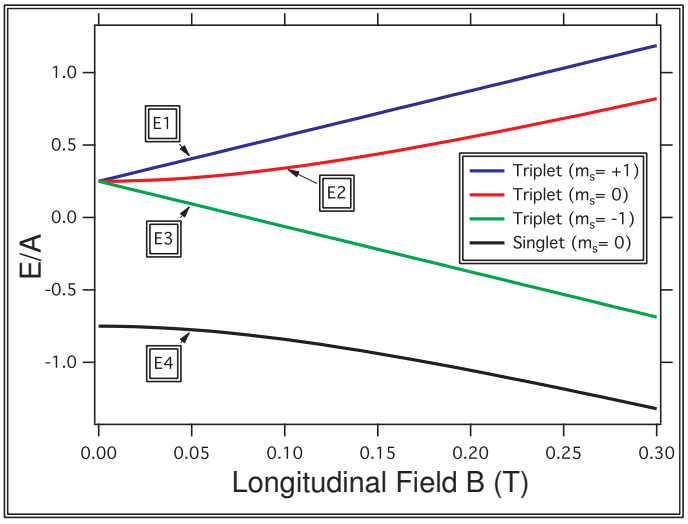

Figure 5.1: Energy levels of isolated muonium as a function of LF

As can be seen the energy levels of the triplet state are degenerate at zero field but split due to the Zeeman interaction as soon as a field is applied. Also important to note is that the energy levels E1 and E2 have a point at approx. 16.4 T where they cross each other and appear degenerate. This is seen in figure 5.2 but later in the section it is shown that the crossing can be avoided by the introduction of nuclear moments to the system.

It has been assumed that the spin system is static up to this point however the two spin system is not static and a more correct solution incorporates the time evolution of the muon spin. Patterson [190] presents a time dependent solution derived using a spin density matrix (SDM) which essentially describes the time evolution of the spins. He defines it, based on the assumptions that the electrons are unpolarised and that there are negligible mixed polarisations, as

$$\rho(t) = \frac{1}{4}(1 + \vec{P}_\mu(t) \cdot \vec{\sigma})$$

where $\vec{P}_\mu(t)$ and $\vec{\sigma}$ are the muon spin polarisation and the 4-dimensional Pauli spin matrix describing the muon spin respectively. It is then logical that he defines the SDM at t=0 to be

$$\rho(0) = \frac{1}{4}(1 + \vec{P}_\mu(0) \cdot \vec{\sigma})$$

Now given that the muons at time zero are fully spin polarised then the SDM is given by

$$\rho(0) = \frac{1}{4}(1 + |\vec{P}_\mu(t=0)| \cdot \vec{\sigma}) = \frac{1}{4}(1 + \vec{\sigma})$$

We also know that the field is applied along the axis of the muon which if defined as the z-axis gives the following

$$\rho(0) = \frac{1}{4}(1 + \vec{\sigma}_z) \tag{5.6}$$

He then uses the Hamiltonian in equation 5.1 and the equation of motion $i\hbar \mathrm{d}\rho/\mathrm{d}t = [H, \rho]$ to obtain

$$P_\mu(t) = Tr\left[\left(e^{(-iHt/\hbar)}\rho(0)e^{(-iHt/\hbar)}\right) \cdot \vec{\sigma}\right] \tag{5.7}$$

When the trace has been taken the time and field dependent polarisation is determined to be

$$P_\mu(t) = \underbrace{\frac{A^2 + 2B^2(\gamma_e + \gamma_\mu)^2}{2A^2 + 2B^2(\gamma_e + \gamma_\mu)^2}}_{\text{Repolarisation}} + \underbrace{\frac{A^2}{2A^2 + 2B^2(\gamma_e + \gamma_\mu)^2}\cos(\omega_{24}t)}_{\text{Oscillation}}$$

$$= \bar{P}_{\mu,iso} + P_{osc} \tag{5.8}$$

where $\omega_{24} = \sqrt{A^2 + B^2(\gamma_e + \gamma_\mu)^2}$ is the frequency of oscillation that the muon spin experiences.

The polarisation consists of two parts, a repolarisation part and an oscillation part. This repolarisation is shown in figure 5.3 and it is clear that at low fields the polarisation is 0.5 but is restored to 1 at higher fields where the hyperfine field is quenched out by the external magnetic fields. It is also shown that there is no relaxation to the oscillatory part for which the frequency corresponds to the energy difference between the energy levels E2 and E4. The oscillations are known as Rabi oscillations and are shown also in figure 5.3. The oscillations are intitially between 0 and 1 when there is no magnetic field. However as the field is increased the energy difference between E2 and E4 is also resulting in a lower amplitude but increasing frequency.

The corresponding magnetic field equivalent to the HFC strength of 4.46 MHz is easily seen from the figure 5.2 to be 16.4 T. At very high fields the HFI is said to be completely quenched out by the field.

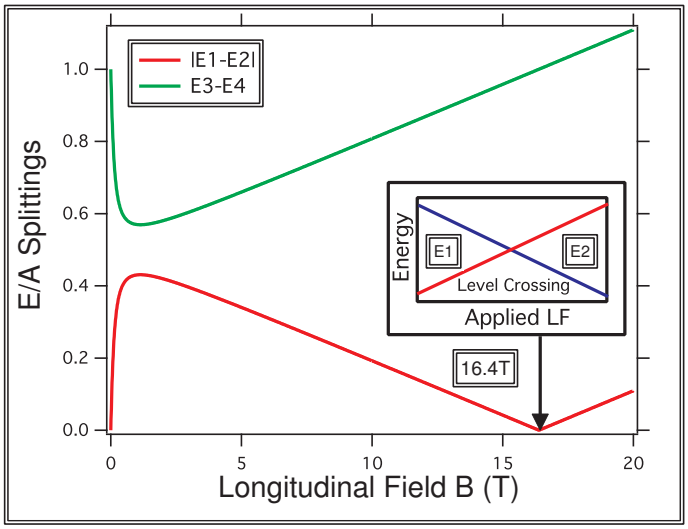

Figure 5.2: Energy level splittings in isotropic muonium

The considerations thus far have been of the idealistic, isolated and completely isotropic two spin system like Muonium. In reality the Rabi oscillations are to fast to be resolved in time and what is seen is an averaging effect which produces a time resolved polarisation reported by Schneider in his thesis [191]

$$\bar{P}_\mu = \frac{\int_0^\infty P_\mu(t) e^{-\lambda t} \mathrm{d}t}{\int_0^\infty e^{-\lambda t} \mathrm{d}t} \tag{5.9}$$

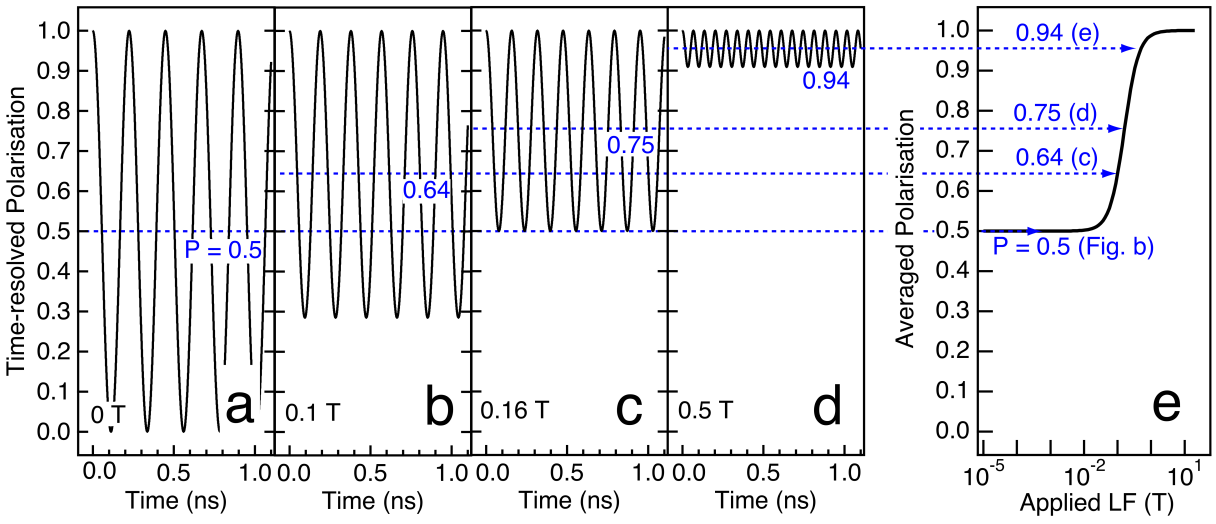

Figure 5.3: Repolarisation and Breit-Rabi oscillations at three fields

It was Heming et al. [192] in their work on detecting muonated free radicals that show that this, in terms of an experimental parameter, is given by the sum of all the data bins or Time Integrated Asymmetry (TIA) and is described by the following equation

$$A(B) = A_0 \bar{P}_\mu = \frac{\Sigma N_B(t) - \Sigma N_F(t)}{\Sigma N_B(t) + \Sigma N_F(t)} \tag{5.10}$$

If equation 5.9 is applied then the solution for the polarisation is in fact reduced

back to the isotropic two spin polarisation case as presented by Pratt [193]

$$\bar{P}_{\mu,iso} = \frac{A^2 + 2B^2(\gamma_e + \gamma_\mu)^2}{2A^2 + 2B^2(\gamma_e + \gamma_\mu)^2}$$

This means that the oscillations vanish and the time averaged oscillations are embodied in the repolarisation curve as seen in figure 5.3.

5.1.2 Anisotropic Muonium

Naturally the next step is to study the anisotropic case of Muonium which has been covered in depth by researchers such as Senba [194] who studies the energy levels and electron spin exchange. This complements the work of Pratt who studies the repolarisation in the case of disordered solids [193]. Firstly it is shown that the polarisation for the case of axial symmetry has a curve described by

$$\bar{P}_{\mu,axial} = \frac{\frac{1}{2}A^2[< cos^2\phi > D_{1,2}^2 + B^2(\gamma_e - \gamma_\mu)^2] + B^2(\gamma_e + \gamma_\mu)^2[D_{1,2}^2 + B^2(\gamma_e - \gamma_\mu)^2]}{[A^2 + B^2(\gamma_e + \gamma_\mu)^2] \cdot [D_{1,2}^2 + B^2(\gamma_e - \gamma_\mu)^2]} \tag{5.11}$$

where $D_{1,2}$ is the axial anisotropic hyperfine coupling parameter. The factor $< cos^2\phi >$ is known as the powder average and usually is equated to a 1/3. It is then shown how this is extended to describe full anisotropy by the use of two dipolar parameters D_1 and D_2. The polarisation now becomes

$$\bar{P}_{\mu,full} = \frac{1}{6}\left[\frac{B^2(\gamma_e - \gamma_\mu)^2}{\frac{5}{12}D_2^2 + B^2(\gamma_e - \gamma_\mu)^2}\right] + \frac{1}{3}\left[\frac{B^2(\gamma_e - \gamma_\mu)^2}{\frac{15}{16}D_1^2 + B^2(\gamma_e - \gamma_\mu)^2}\right] + \frac{1}{2}\left[\frac{B^2(\gamma_e + \gamma_\mu)^2}{A_2^2 + B^2(\gamma_e + \gamma_\mu)^2}\right] \tag{5.12}$$

When considering the Hamiltonian in the case of anisotropy then as discussed by Patterson [190] and Roduner [195] there are effects on the HFI from the surrounding nuclear spins and the anisotropy of the medium. The more complex Hamiltonian shown in equation 5.13 is presented by Roduner and shows the introduction of nuclear terms indexed with a k and the anisotropy in the muon electron HFI.

$$\begin{aligned}\mathcal{H}_{full} =& -\gamma_\mu S_\mu^z B_z + \gamma_e S_e^z B_z + \sum_k -\gamma_k S_k^z B_z + A_\mu S_\mu^z S_e^z + \sum_k A_k S_k^z S_e^z \\ &+ \frac{1}{2} A_\mu [\hat{S}_e^+ \hat{S}_\mu^- + \hat{S}_e^- \hat{S}_\mu^+] + \frac{1}{2} \sum_k A_k [\hat{S}_e^+ \hat{S}_k^- + \hat{S}_e^- \hat{S}_k^+] \\ &- D_{\mu,1,2}[A^\mu + B^\mu + C^\mu + D^\mu + E^\mu + F^\mu] \\ &- \sum_k D_{k,1,2}[A^k + B^k + C^k + D^k + E^k + F^k] \end{aligned} \tag{5.13}$$

$$\begin{aligned} A^i &= +(1 - 3\cos^2\theta)(S_e^z S_i^z) \\ B^i &= -\tfrac{1}{4}(1 - 3\cos^2\theta)(\hat{S}_e^+ \hat{S}_i^- + \hat{S}_e^- \hat{S}_i^+) && \Delta M = 0 \\ C^i &= -\tfrac{3}{2}(\sin\theta\cos\theta e^{(-i\phi)})(S_e^z \hat{S}_i^+ + \hat{S}_e^+ S_i^z) && \Delta M = 1 \\ D^i &= -\tfrac{3}{2}(\sin\theta\cos\theta e^{(+i\phi)})(S_e^z \hat{S}_i^- + \hat{S}_e^- S_i^z) && \Delta M = 1 \\ E^i &= -\tfrac{3}{4}(\sin^2\theta e^{(-2i\phi)})(\hat{S}_e^+ \hat{S}_i^+) && \Delta M = 2 \\ F^i &= -\tfrac{3}{4}(\sin^2\theta e^{(+2i\phi)})(\hat{S}_e^- \hat{S}_i^-) && \Delta M = 2 \end{aligned}$$

where $\hat{S}_\mu^\pm$,$\hat{S}_e^\pm$,$\hat{S}_k^\pm$ are the ladder operators and S_μ^z,S_e^z,S_k^z are the z-components of the spin operators. Also θ and ϕ are the angles between B and the symmetry axis, and the azimuthal angle. In addition to the effects mentioned this has two other significant effects:

1. The degeneracy of the triplet states at B=0T is lifted.
2. The energy levels owing to the mixing of states no longer cross anymore but instead avoid each other to form an avoided level crossing (ALC).

5.1.3 Avoided Level Crossings

As mentioned before in the case of perfect isotropy there is a crossing of energy levels at a particular field, however the anisotropy and introduction of nuclear spins in to a system causes the mixing of spin states. This means that the system can no longer be described by pure zeeman states at higher fields, therefore, the degeneracy at this point is lifted and an oscillations between the energy states occurs at a frequency corresponding to the energy difference. An example of this is shown in figure 5.4. This mixture of states arises from the ladder operators in the Hamiltonian allowing

more transitions between neighbouring states. The resultant time integrated polarisation of the muon spin as the magnetic field is tuned through the ALC resonance and the exact nature of the oscillations are shown in figure 5.5. It is clear to see from the figures that over all the ALC results in a loss of polarisation although the lowest point is slightly shifted from the ALC theoretical value and this is typical of an anisotropic HFI.

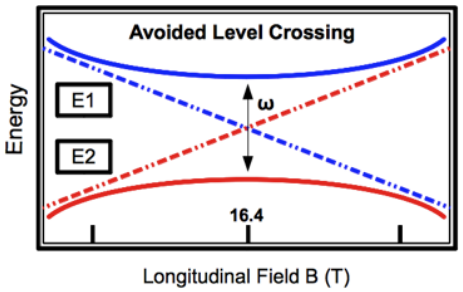

Figure 5.4: Avoided level crossing

As the difference between the two dipolar coupling constants described previously is increased the distortion is greater. It is also possible to see that the oscillations not only increase in amplitude but reduce in frequency emphasising the fact that the energy difference between the two levels is decreasing. In general the ALC resonances can be split in to 3 classes for which many examples exist such as the studies by Roduner [196], Flemming [197] and Bridges [198] and their co-workers.

The first of these resonances is called the $\Delta 0$ ($\Delta M = 0$) resonance and is a muon-nuclear spin flip-flop transition. It is caused by the coupling of the isotropic muon HFCs to the nuclear HFCs and arises from the elements, $A_k[\hat{S}_e^+\hat{S}_k^- + \hat{S}_e^-\hat{S}_k^+]$ and $A_\mu[\hat{S}_e^+\hat{S}_\mu^- + \hat{S}_e^-\hat{S}_\mu^+]$ in the axial symmetric Hamiltonian. The resonance is indirect meaning it is mediated by the electron and occurs in media where the nuclear spins are accessible. It is normally accompanied by strong ALC size and has a resonant field described by Roduner et al. [196] to be

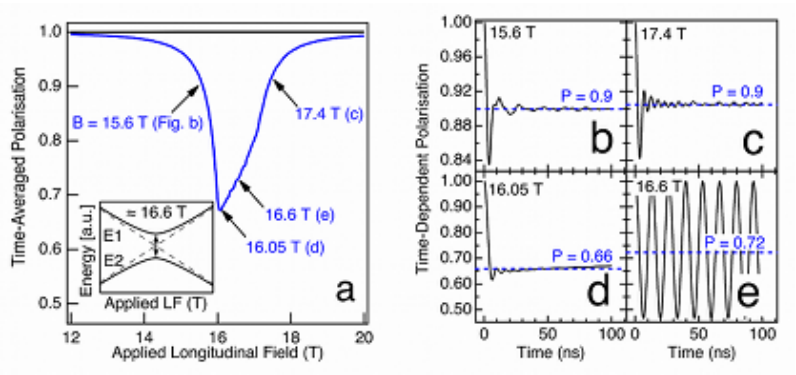

Figure 5.5: Muon spin polarisation tuning through ALC resonance

$$B_r(\Delta_0) = \frac{|A_\mu - A_k|}{2(\gamma_\mu - \gamma_k)} - \frac{A_\mu + A_k}{2\gamma_e}$$

There is still an asymmetric shape to the ALC arising from the anisotropy in the system and therefore the HFCs in the resonant field are in fact effective HFCs.

The second class of resonance is the $\Delta 1$ ($\Delta M = 1$) resonance which is a muon-electron spin flip and is the simplest ALC. It arises from the dipolar components of

the HFI and has a very large intensity. The resonance field can be described by

$$B_r(\Delta_1) = \frac{|A_\mu|}{2\gamma_\mu} - \frac{A_\mu}{2\gamma_e}$$

As is evident in the work of Roduner et al. [196] on reorientational dynamics of cyclohexadienyl radicals this resonance is usually only present in solid media as the reorientations in liquids and gases averages out the DT and is explained further in reference [195].

The third class of resonance is the $\Delta 2$ ($\Delta M = 2$) resonance and is a muon-nuclear spin flip-flip transition. The ALC resonances are weak and have no true relevance for disordered systems. They are similar to the $\Delta 0$ resonances, however, they are driven by the anisotropic parts of the Hamiltonian $S_e^+ S_k^+$, $S_e^- S_k^-$, $S_e^+ S_\mu^+$ and $S_e^- S_\mu^-$. There have been studies of this resonance even though it is very weak and it was reported in single crystal Benzene in 1990 by Roduner [199].

It is worth pointing out that the resonances to this point have been described using the aide of an axially symmetric Hamiltonian and that the principles still stand on the introduction of full anisotropy which must be assumed as there is generally no symmetry in a system.

ALC Line Shape and the Effects of Electron Spin Relaxation

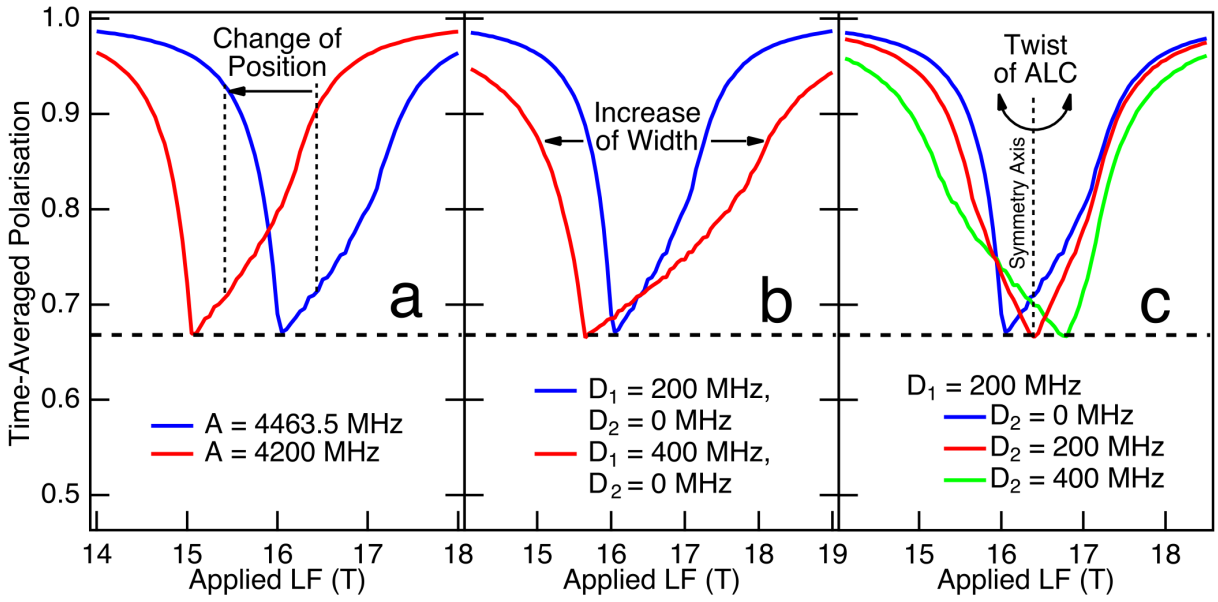

Figure 5.6: The effect of the a) A, b) D_1 and c) D_2 parameters on the ALC line shape

In order to analyse the data presented in this thesis it is important to understand what processes/parameter change the line shape of the ALC resonances. There are

four main variations to the line shape that need to be considered. The first of these is a magnetic field shift in the resonance value which is typically related to the HFC A. A chemical/crystal structure change may cause a shift in position as the electron density at the muon site varies and alters the coupling values. Similarly different muon sites and conformations can alter the position of the ALC and therefore it is important to consider the muon sites present in the system. There may be some very small shifts with temperature as the vibrations of the molecules alter the couplings slightly. The effect of the A parameter can be seen in Figure 5.6a [200]. The next variation to consider is the asymmetry and width of the ALC. These two properties are typically determined by the parameters D_i, specifically the difference between the D parameters influences the asymmetry in the line shape and the D_1 parameter is responsible for a change in width. The D parameters are related to the symmetry in the system and therefore they can be different at different muon sites and for different molecules. The effects of the D_1 parameter can be seen in Figure 5.6b. It is also worth noting that if there are a distribution of HFCs very close together in the system then any changes in their intensity can appear as a change in width. The third variation of the line shape is that related to the second D parameter D_2 which is a twisting of the ALC effecting both the width and asymmetry simultaneously. An example of this can be seen in Figure 5.6c and again this variation is related to a change in the asymmetry of the system and can result from several causes. The last major variation to the line shape is the change of the amplitude. The amplitude of the resonance is determined by the intrinsic depolarisation of the muon at the resonance field and is strongly dependent on the system. Therefore, any increase to the amplitude of the ALC in the same system is a result of a further de-phasing/relaxation of the muon spin ensemble. This is important in this thesis as, in the case of electron spin dynamics, any relaxation in the coupled electron's spin will endure a further depolarisation of the already sensitive muon spin. This is looked at in more depth in the following part of this section. It is worth noting that there are are some additional processes that can result in line shape changes and indeed Roduner and co-workers [195, 196, 201], in various studies, explain how in addition to the asymmetry in the system, reorientation dynamics have an averaging effect on the Hyperfine Tensor. This then leaves one to discuss the introduction of electron spin relaxation. Up to this point only the muon spin relaxation has been considered and to encorporate the electron the SDM needs to be extended to include the electron and mixed polarisation. The are denoted $\vec{P}_e$ and P^{ij} respectively and so the density matrix becomes

$$\rho(t) = \frac{1}{4}\left(1 + \vec{P}_\mu(t)\cdot\vec{\sigma} + \vec{P}_e(t)\cdot\vec{\tau} + \sum_{\mathrm{i,j}} P^{ij}_{mix}\sigma^i\tau^j\right)$$

where $\vec{\tau}$ are the Pauli matrices for the electron spin. According to the studies of Meier [202] on the spin dynamics of transitions that occur between muon states there is a set of 15 differential equations that are provided by the quantum mechanical equation of motion. However, Heming et al. [203] show in their studies of organic free radicals using ALC-MuSR that if a nuclear spin is included then there are in fact 63 differential equations. Meier explains that if the electrons are assumed to experience spin-flips at a rate λ_{eSR} then the differential equations have to be expanded so that they contain the terms

$$\frac{\mathrm{d}\vec{P}_e}{\mathrm{d}t} = \cdots - \lambda_{eSR}\vec{P}_e \quad , \quad \frac{\mathrm{d}\vec{P}_{ij}}{\mathrm{d}t} = \cdots - \lambda_{eSR}\vec{P}_{ij} \tag{5.14}$$

It is not generally possible to solve these equations analytically however simulations like that shown in figure 5.7 show that the electron spin relaxation (eSR) induces a muon spin relaxation. These simulations are obtained from the program Quantum program [204] in which the time evolution of the spin density matrix is solved numerically to produce the muon spin relaxation data. The polarisation is obtained through the integration of the time resolved data at a given magnetic field. Monte Carlo methods are then applied to account for the powder averaging and any random fluctuations in the system. The software allows for the entry of the isotropic HFC, the axial dipolar coupling (D_1) and the non-axial dipolar coupling (D_2) parameters denoted the A, D and E parameters respectively. These parameters are used throughout the results in this thesis. The software allows also for the entry of a spin flip rate of the electron which is reflected in the muon polarisation and is referred to as the eSR throughout the results in this thesis. In these studies the measurement of electron spin relaxation in some of the small molecules reviewed in chapter 1 is reported and it is explained how the values for the electron spin relaxation rates can be extracted for the data.

The additional muon spin relaxation is superimposed on the already damped Rabi-Oscillations previously described and leads to an increase of the ALC size. It essentially enhances the ALC resonance without changing much the position or width. This is key to the results in this thesis as it is the only reasonable explanation for such an increase in the data and reveals the presence of an additional electron spin relaxation in the system.

5.2 Muonium in a Transverse Applied Field

The study of the system in the presence of a high transverse field allows for a very accurate determination of the strength of the coupling between the muon and electron spin. When in a transverse field the spin of the diamagnetic muon precesses

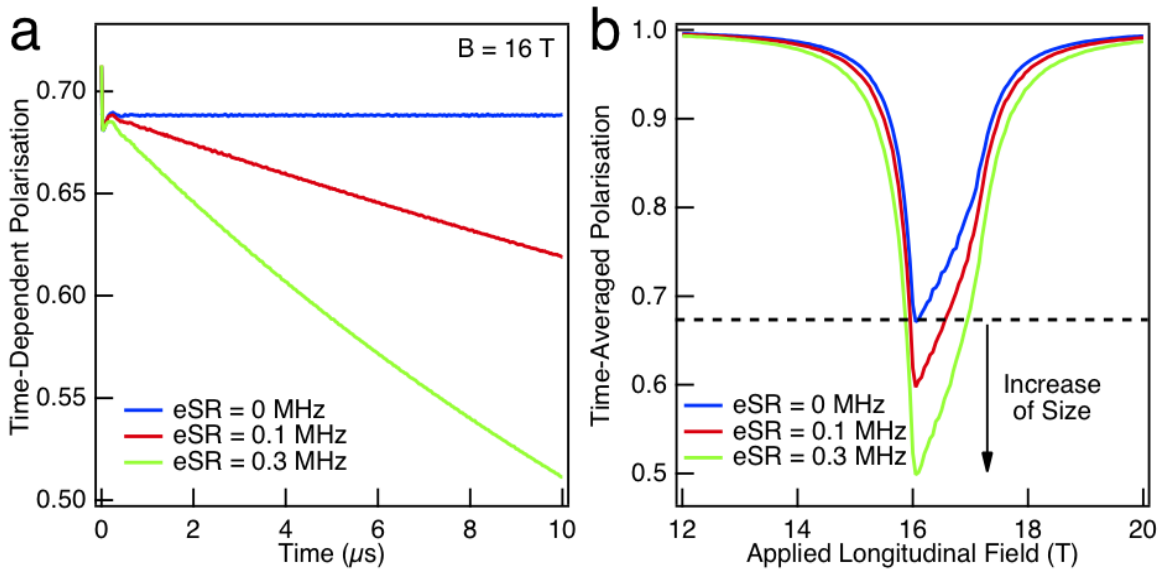

Figure 5.7: The effect of eSR on the muon spin polarisation both for the Rabi-oscillations and for the simulated ALC

with a Larmor frequency. In the case of the isotropic muonium this frequency of precession corresponds to the energy difference shown in the Breit-Rabi diagram (figure 5.4). The amplitude of this precession signal is given by ${C^2}_m/2$ where the individual equations are as follows [190]:

$$E_1 - E_2 \rightarrow {C^2}_2 \tag{5.15a}$$

$$E_2 - E_3 \rightarrow {C^1}_2 \tag{5.15b}$$

$$E_3 - E_4 \rightarrow {C^2}_2 \tag{5.15c}$$

$$E_1 - E_4 \rightarrow {C^1}_2 \tag{5.15d}$$

When the field is $\geq$ 100 mT the only precession frequencies apparent are those governed by $E_1 - E_2$ and $E_3 - E_4$ as the value of C_1 tends to zero and consequently the other precession frequencies are quenched out. The region in which this occurs is denoted the Paschen-Bach regime. It is also the case that these high fields quench out the HFI with the nuclear spins [190]. The remaining states differing only by the muon spin quantum number and not that of the electron or nuclear quantum spin number are mixed [205]. Therefore the two observable muon spin procession

frequencies can be described by the following equations [206]:

$$f_{12} = \frac{1}{2}A + \frac{1}{2}\left(\gamma_e - \gamma_\mu\right)B - \frac{1}{2}A\sqrt{1 + \left(\frac{2B\left(\gamma_e + \gamma_\mu\right)}{A}\right)^2} \tag{5.16a}$$

$$f_{34} = \frac{1}{2}A + \frac{1}{2}\left(\gamma_e - \gamma_\mu\right)B + \frac{1}{2}A\sqrt{1 + \left(\frac{2B\left(\gamma_e + \gamma_\mu\right)}{A}\right)^2} \tag{5.16b}$$

It is clear that the sum of these two frequencies is equal to the isotropic HFC [190, 206] and the amplitudes of the precession signals are equal.

Chapter 6

The Extraction of Avoided Level Crossings and determination of Muon Adduct Sites

6.1 Background Subtraction

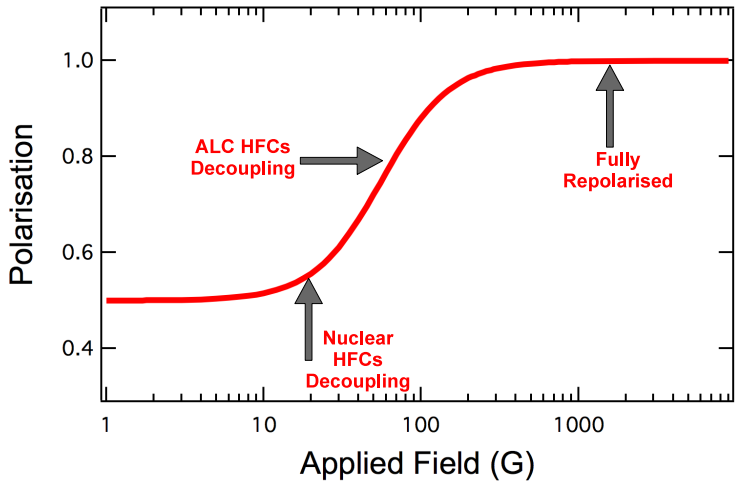

Figure 6.1: An example of a typical repolarisation curve

In order to obtain meaningful information about the eSR from the measured samples the ALCs must first be extracted from the raw data. To do this the time resolved data are firstly condensed down to obtain the time integrated data. This is achieved by the application of equation 5.10 in chapter 5. The time integrated data is then plotted as a series of points against magnetic field and provides the plot in which the resonance is apparent. However, this data still consists of background elements. The background has two major contributing parts. The first of these is the repolarisation curve discussed in Section 5.1. There are three main parts to the repolarisation curve. The first part is at very low fields where the nuclear HFCs start to decouple.

This is in the region of zero to a few mT and appears as a shallow increase in the asymmetry at these fields. The second region is the sharp rise in asymmetry as the muons start to decouple from the ALC HFCs and start to recover their polarisation. The final region is where the muons are nearly fully repolarised and the asymmetry is essentially flat on a local scale. These regions are highlighted in Figure 6.1. In the case of the Quinolate molecules the ALC resonances lie in this region as the they are situated at high fields. However the resonances in TIPS-Pentacene and Rubrene are situated in a region where the muons are very much still repolarising. The repolarisation curve can be fitted using the equations in Section 5.1. Typically a combination of the isotropic and anisotropic repolarisation curves are required to gain an accurate representation of the data.

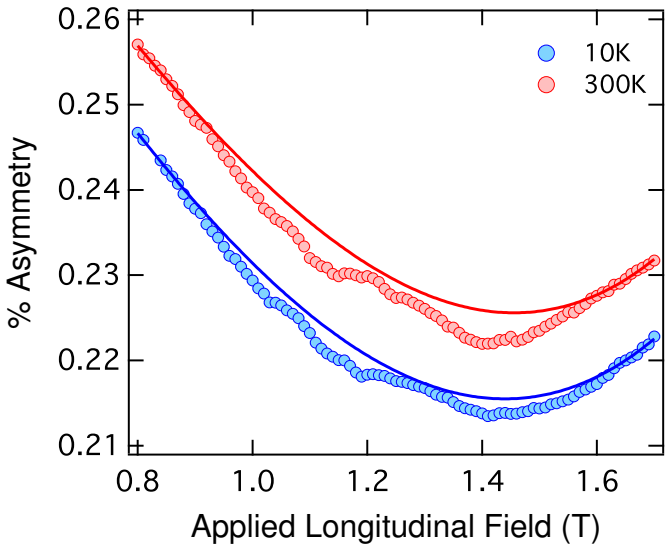

Figure 6.2: An example of background fitting to the AlQ_3 time integrated data taken on the ALC spectrometer

Fitting these curves is useful as the ALCs can be directly subtracted from the curve. However in most cases there is an additional second background component evolving from the positrons spiralling in the higher magnetic fields. This spiralling induces a focusing-defocusing effect seen as a very gradual oscillation in the time integrated asymmetry. This background can also be fitted by superimposing a shifted polynomial on top of the repolarisation curves. This enables a full background subtraction to extract the ALCs. In some cases the polynomial function alone is sufficient to fit the local data around the resonance as in the case of the Quinolate series. The fitted data for the AlQ_3 is shown in Figure 6.2. In this case the polynomial used was of fourth order. It was also shown that the results in TIPS-Pentacene for both methods of fitting were in agreement with one another and the results of these fits can be seen in Figure 6.3a. In the case of Rubrene the ALCs could only be extracted by fitting the full repolarisation curves as seen in Figure 6.3b. Once the data has been substantially fitted the ALCs can be extracted from the background are ready

to model to ascertain the eSR values reported later.

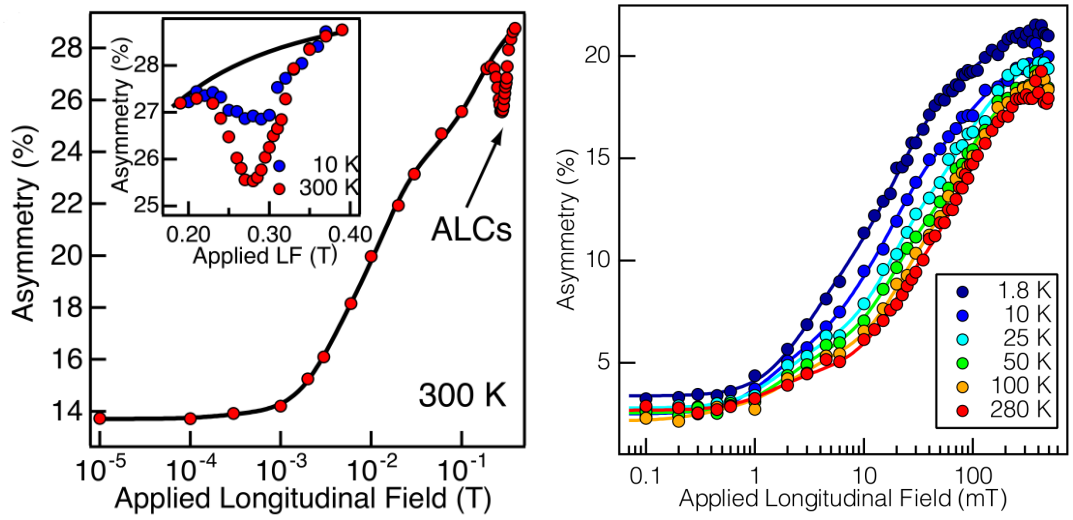

(a) An example of background fitting to the TIPS-Pentacene time integrated data taken on the ARGUS spectrometer

(b) An example of background fitting to the Rubrene time integrated data taken on the ARGUS spectrometer

Figure 6.3: Background fitting in the Functionalised Acenes

6.2 Muon Site Allocation

After forming muonium the muon can join on to a molecule in a similar manor as the addition of a Hydrogen atom. There are several possible adduct positions in the small molecules reported in this thesis and in addition to the various adduct sites there are two conformations in which the muon can be oriented. These positions and the associated coupling constants can be calculated using computational methods such as semi-emperical calculations i.e. PM3 or density functional theory (DFT) calculations. The main difference is that the semi-emperical methods are based on the Hartree-Fock method or a extended version of this, where as the DFT calculations map out many body problems on to single body problems using density functionals. Whilst the simplest method for solving the many body Schrödinger equation is to use the Hartree-Fock method it requires large quantities of computational power and so is difficult to for complex many atom systems and so the DFT calculations offer a more powerful computational tool. Which method is more accurate depends on the manor in which the calculations are performed. DFT calculations if carried out right with the appropriate exchange functions and basis sets have the ability to give more accurate theoretical values, although if the wrong basis set is used or there are large truncation errors or bad geometrical optimisations the accuracy is far better in the PM3 calculations. Very recently, given a lack of appropriate published DFT calculations, a combination a semi-emperical optimisation applied in a DFT

calculation were performed on the Quinolate molecule AlQ_3 and will be discussed further later in this section. Also the DFT values for the HFCs will be compared to the modelled 10K data in both the TIPS-Pentacene and in AlQ_3 .

6.2.1 TIPS-Pentacene

DFT calculations for the TIPS-Pentacene molecule have been initially performed by McKenzie [207] in order to provide the HFCs for the adduct sites and are the only available DFT calculations for this molecule. These calculations, although still allowing for the assignment of adduct positions do consist of some discrepancies which are important to bear in mind when considering the certainty with which the muon sites can be assigned. The more major of the discrepancies is the optimisation of the molecule using the DFT calculations. This optimisation cannot properly account for the real crystal structure of the molecules when optimising the system and so the spatial constraints imposed by the crystal packing of the molecules are ignored. It is mainly for this reason that the DFT optimisation is not as appropriate in the solid state as in the liquids. This effects the formation probabilities and the HFC constant values as the spin distribution on the molecule is altered and hence the results based on the spin distribution are incorrect with the poorer optimisation.

In addition to the optimisation issues the calculations fails to account for the different conformations of the muon at each adduct site so no significant differences in the final values obtained for either conformation must be assumed from the results. This is not the case and in fact there are significant changes to the HFC values. These are not surprising as if the crystal packing is considered then some of the conformations are less preferable because of the proximity to the other atoms and the rigidity of the structure. This means there are essential radical states missing from the calculations which when not included in the calculated average for the adduct site can induce an additional error in the overall HFC values. Lastly the calculations fail to provide any dipolar coupling terms so when reproducing the values in order to model any data the ALC shapes are assumed to be of a Lorenzian form. It is clear to see these discrepancies result in significant errors, in the order of 40%, when considering the data obtained from modelling of the 10 K spectra.

In order to ascertain all the possible adduct position HFCs a broad field scan was initially taken for TIPS-Pentacene. The resultant extracted ALCs are presented in Figure 6.4. It is clear to see that the data can be separated in to two field regions. The lower field region contains two groups of AlCs, Groups 1 and 2 in Figure 6.4a. These groups were modelled at 10K using the Quantum software written by Lord [204] in which a powder averaging and hopping option were applied. The simulation is carried out using a Monte Carlo method with 10000 Monte Carlo steps to ensure fine detail in the final modelling. In the program both the time

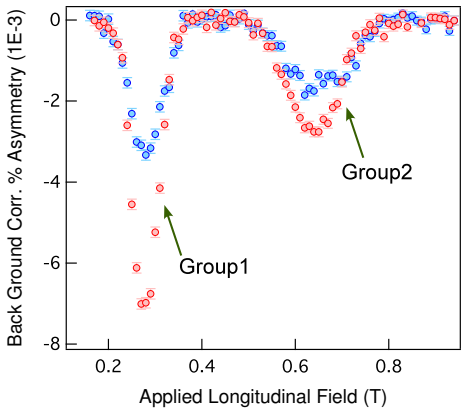

(a) Lower half of B field scan for TIPS-Pentacene at 10 K and 300 K consisting of two major resonances, group 1 and group 2

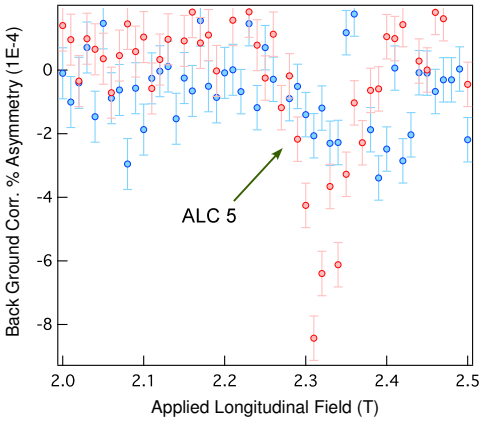

(b) Upper half of B field scan for TIPS-Pentacene at 10 K and 300 K consisting of an individual weak ALC

Figure 6.4: Full longitudinal field scan for TIPS-Pentacene at 10 K(blue) and 300 K(red)

resolved data and the polarisation data are calculated. The modelling produced ALC resonances and hence HFC values for all the ALCs in the spectra. In addition the anisotropic terms and eSR can be extracted from the modelling and will be covered later. In order to satisfactorily model the groups 1 and 2 two sets of two independent ALCs were required, ALCs 1 and 2 for group 1 and ALCs 3 and 4 for group 2. An example of how the ALCs are modelled in group 1 is shown in Figure 6.5 from which it is clear how the overall shape, position and intensity of the group are determined by the sum of the two independent ALCs (the modelling parameters are those for sites 6 and 3 in Table 6.1). The higher field region contains only the one ALC which is very low in intensity compared to those in the lower field region. This poses a problem when modelling the data as there is a lack of finer detail to determine the width and shape of the ALC. Despite this, the ALC was modelled in the best possible manor to obtain a HFC value.

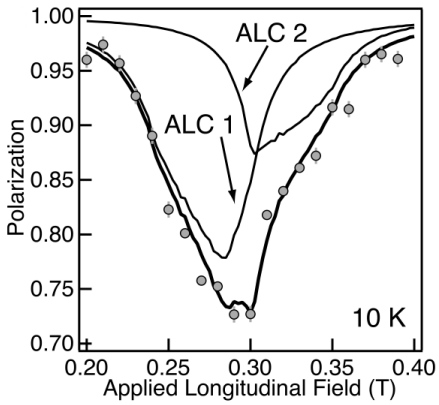

Figure 6.5: Modelling of the two independent ALCs in group 1 in TIPS-Pentacene

In addition to the modelling of the time integrated data the HFCs for the ALCs in group 1 were determined more accurately through TF-MuSR measurements of TIPS-Pentacene. In the Fourier space it is possible to extract the frequencies present in the time resolved TF-data. Figure 6.6 (top) shows the Fourier analysis at a TF of 0.45 T. The most visible feature is the main field peak at about 60 MHz. This is the precession frequency at which the main applied field appears and is not the key feature. It is also possible to observe two smaller satellite peaks situated symmetrically either side of the main peak. These are the important peaks as they evolve from the muon precession frequencies of the HFCs in group 1. The satellite peaks are quite broad which suggests that they may be the result of more then one HFC frequency. It is possible to resolve these peaks through a different type of analysis. The Maximum Entropy analysis of the same time resolved data can also be seen in Figure 6.6 (bottom).

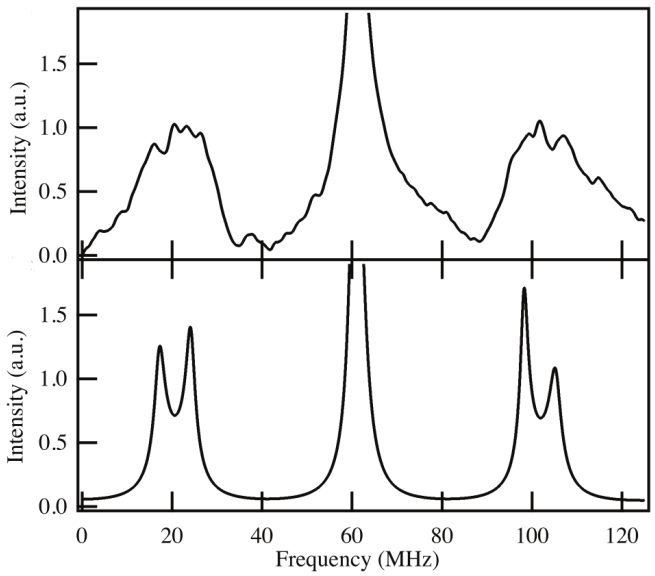

Figure 6.6: Fourier analysis of TF time-resolved data in TIPS-Pentacene at 0.45 T and at 5 K taken on the DOLLY spectrometer (top). Maximum Entropy analysis of the same data with two clear frequencies resolved in the satellite peaks (bottom)

It is immediately obvious that the peaks can be resolved in to two separate frequencies which are sharper than the peaks in the Fourier analysis. The values for the HFC frequencies can be determined by sum of the differences of a corresponding pair of symmetrical peaks and the central main field peak. This was determined for both the sets of peaks to extract the two HFC frequencies in group 1 which were 74.5 MHz and 87.5 MHz. These values are remarkably close to the HFCs obtained from the modelling of the data confirming the accuracy of these results.

Before proceeding to compare the values of the modelling to the DFT values it is necessary to define the site notation used in the DFT calculations. Figure 6.7 shows the structure of TIPS-Pentacene along with the site numbering used in the DFT

calculations by McKenzie. These correspond to the values reported in Table 6.1 alongside the results from the modelling of the data. In order to differentiate the sites of the triple bond in the TIPS-Pentacene additional DFT calculations were performed by McKenzie [207] for Pentacene in which the triple bond is not present and hence provides a direct comparison. These results are also reported in Table 6.1. The method for calculating these values is the same as that used in the TIPS-Pentacene.

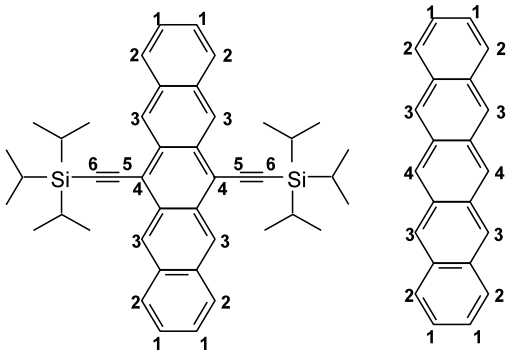

Figure 6.7: Structure for TIPS-Pentacene and Pentacene with muon assignments

Table 6.1: TIPS- Pentacene model parameters and DFT calculation results

Data				**DFT A_μ (MHz)**	
SITE	**A (MHz)**	**D (MHz)**	**E (MHz)**	**TIPS**	**Pentacene**
SITE 1	189.0±1.0	−11.0±0.7	8.0±1.0	253.43	279.49
SITE 2	169.0±1.0	−10.0±0.7	5.0±0.5	n.c.	255.47
SITE 3	84.5±0.6	10.0±0.8	5.0±1.0	114.40	121.60
SITE 4	−	−	−	−	98.07
SITE 5	650.0±1.0	10.0±0.8	10.0±0.8	662.32	−
SITE 6	72.5±0.5	−5.0±1.0	5.0±1.0	109.13	−

The values calculated by McKenzie can be broken down in to two groups of two ALCs and an odd higher frequency ALC. This is not too dissimilar from the values extracted from the data. The highest value in the DFT frequencies is a lot higher then the other values and so naturally could correspond to the individual ALC 5 present in the data. The site number for this ALC is site 5 on the triple bond and is unique to the TIPS-Pentacene as the bond is not present in the Pentacene. It is for this reason that this site can be assigned more definitively as the ALC is not present in the Pentacene confirming that it must be related to the triple bond. Another site that can be ruled out is site 4 as it is a tertiary carbon and the muons preferentially add to the secondary carbons [208] and hence voids this site as a possible muon adduct position. This leaves the two groups of ALCs in the low magnetic field region. The lowest two values in the DFT calculations are quite close in value as in the case of the modelled HFCs so would indicate that the site numbers site 6 and

3 correspond to ALCs 1 and 2 respectively in the data. This is supported by the ALC data in Pentacene as site 6 is not present in the Pentacene molecule so this resonance should not be present in the pentacene ALC spectra.

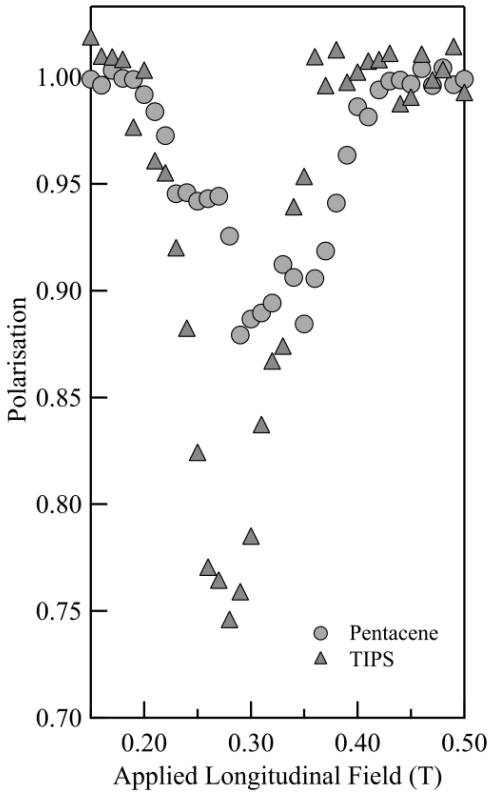

Figure 6.8: Comparison of the TIPS-Pentacene and Pentacene group 1 ALC resonances at 10 K

Figure 6.8 shows a comparison of the TIPS-Pentacene and Pentacene ALCs. It is clear to see the intensity of the ALC in Pentacene is half that of the TIPS-Pentacene and the ALC is situated at the same value as ALC 2 in TIPS-Pentacene. This confirms that the resonance at site 6 is missing and hence the ALC 1 is not present in the Pentacene data. Given this information, the assignment of site 3 to ALC 2 and site 6 to ALC 1 can be made. The assignment of ALCs to the triple bonds is not unheard of and similar work has been conducted in TCNQ [33] where the muon adduct site has been assigned to the end of the triple bond. The last two sites to be assigned are sites 1 and 2. The DFT calculation for site 2 did not converge which adds some uncertainty in to the assignment of the adduct positions to the ALCs. Although, by comparing the ALC HFCs to the values calculated for Pentacene it is still possible to assign the sites correctly. The lowest value in the pair of DFT calculations is site 1 using the value for site 2 from the Pentacene data and therefore would correspond to ALC 3. Where as, the higher value from the Pentacene calculations would correspond to ALC 4 in the TIPS-Pentacene. There is now a complete allocation of the muon adduct positions to the ALCs present in the TIPS-Pentacene data.

6.2.2 AlQ_3

In the case of AlQ_3 the initial DFT calculations considered were those performed by McKenzie for the AlQ_3 molecule [208]. The results of these calculations are used to obtain crucial information about the electron mobility on the molecule. They show that the Muonium electron is in an energy level such that energy difference is too great for the electron to move from the adduct site and hence is bound. This confirms that any spin relaxation is not transport based. However, the same discrepancies exist in these calculations as in the TIPS-Pentacene with the additional problem that they do not consider the ligands in the AlQ_3 separately. This implies that no significant change in the HFCs between the ligands which is contradictory to the muon data presented in this thesis in which there is a clear broadening of the spectra. Despite this, it is still possible, as in the case of TIPS-Pentacene, to compare these DFT HFCs to the values obtained from the modelling of the data. The problems present in the calculations performed by McKenzie, have prompted a very recent set of DFT calculations by another collaborator F. Pratt which build on these initial calculations. After private discussion with Pratt calculations with a different method of geometric optimisation were performed and the results have been compared. The key difference in the calculations is that the optimisation is carried out using an unrestricted Hartree-Fock method with a semi-emperical PM3 parameterisation. This allows for a much better relaxation of the crystal structure addressing some of the solid state effects that are pose a challenge in McKenzie's calculations. This geometry is then used in a DFT calculation to obtain the HFCs and spin distribution in the molecule. McKenzie uses the same exchange and correlation functional, B3LYP, as Pratt but has a different basis set. Pratt uses a standard 6-31G gaussian basis set with no additional functions whereas McKenzie uses two additional d and p polarisation functions in conjunction with the 6-31G basis set, the larger basis set being more ideal. Even with the reduced basis set the calculations by Pratt are still allow for more accuracy in determining the values of the HFCs. This perhaps suggests that the key to obtaining better solid state DFT calculations lies in the initial optimisation of the molecule. Given this better accuracy in the two part DFT calculations these values will be used to assign the muon adduct positions.

The data for the AlQ_3 were modelled at 10 K as in the case of TIPS-Pentacene for which the method is described later in Chapter 8. The 10 K data can be seen in Figure 6.9 along with the numbering convention of the sites for the AlQ_3 ligands (inset). The modelling results are reported in Table 6.2 along with the calculated HFCs for both McKenzie and Pratt. In the case of Pratt's calculations it was also possible to obtain the shapes of the ALCs as the dipolar parameters are provided from the calculations using the spatial distributions of the atomic spin densities

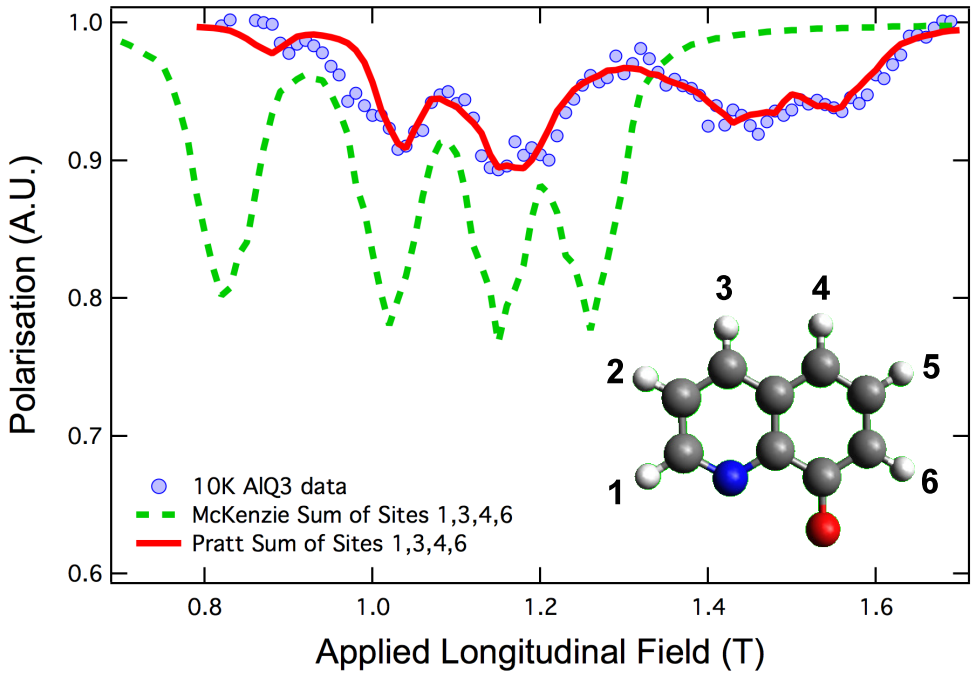

Figure 6.9: DFT calculations by McKenzie (green dashed) and Pratt (red solid) for sites 1, 3, 4 and 6. Also 10 K resonance data for AlQ_3 (blue markers) and inset, the muon site allocation for each ligand on the Quinolate molecule

Table 6.2: Comparison on calculated DFT and modelled HFCs in AlQ_3

	Pratt (MHz)							**Data (MHz)**	**McKenzie (MHz)**
	A1	**A2**	**B1**	**B2**	**C1**	**C2**	**Ave$_P$**	**Ave$_{dat}$**	**Ave$_M$**
Site 1	427.2	416.2	449.3	411.1	420.7	393.7	419.7	420.0	342.99
Site 2	498.9	484.9	501.4	491.6	467.2	513.8	493.0	-	449.27
Site 3	380.1	381.5	405.2	357.5	374.8	323.4	370.4	386.0	313.65
Site 4	284.9	297.4	291.4	311.8	281.3	241.3	284.7	292.5	224.26
Site 5	573.2	580.5	546.7	560.3	506.0	595.0	560.3	-	469.80
Site 6	330.4	337.1	372.4	344.7	327.9	312.3	337.5	329.0	277.89

given by the DFT calculations. It is clear to see from Figure 6.9 that once plotted it is possible to compare the direct values with the modelling results as the DFT values of Pratt are to within 5% of the modelled values. There is one common factor between the two sets of calculations irrespective of the method and that is the values obtained for sites 2 and 5 are not present in the MuSR data. This could be due to the fact that the spatial constraints of the crystal packing prohibit the addition of muonium at these sites essentially giving a formation probability of zero.

There remains 24 possible adduct positions for which the average ALC shapes can be seen in Figure 6.10 although it is not possible to resolve all 24 positions as the ALCs are to close to one another to exhibit distinctive features. Consequently the different HFCs for each site combine to give broad resonances positioned around the average calculated values and hence produce broader dipolar coupling terms in the

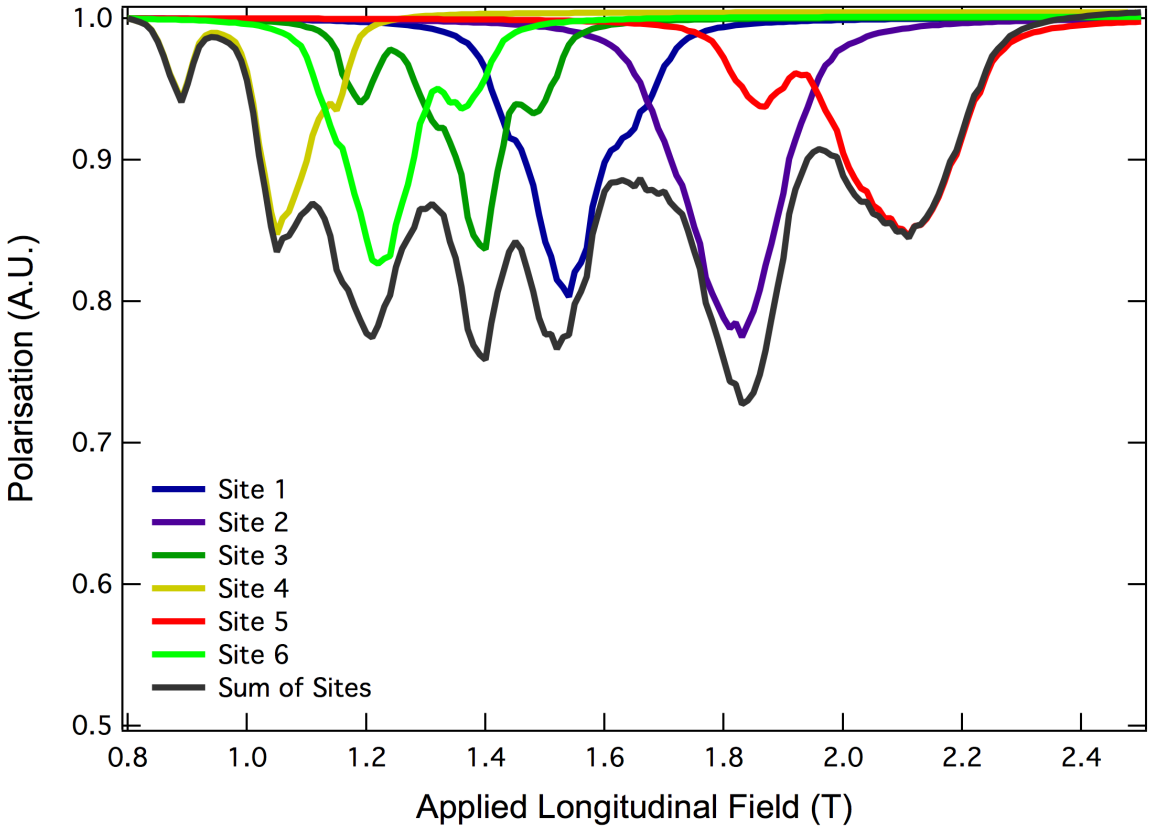

Figure 6.10: Complete sum of the ALCs from Pratt's DFT calculations with individual site components shown also

modelled data. Despite this it is still possible to allocate an overall site to each of the modelled ALCs in the data. There is one site where it is possible to resolve the additional detail from one of the ligands and this is in site 4. In the data there are two ALCs (ALC1 and ALC2 in table 8.1) which correspond to the values calculated for ligand C of site 4 and ligands A and B of site 4 respectively. The value of ALC1 is within 5% of the average value for ligand C and the value for ALC2 is also within 5% of the average value for ligands A and B. This is very good agreement between the calculated and measured values.

The finer detail of the remaining sites cannot be resolved however the DFT value for site 6 can be assigned to ALC 3 in the data as the average value from the data is within 2% of the modelled value from the data. It is worth noting that the slight differences between the calculated and measured values could evolve from the fact that there is no formation probabilities taken in to account in the average calculated values where as these probabilities influence the HFC positions in the modelled data and hence may slightly shift the values. The next site that can be assigned is site 3 which corresponds to ALC 4 in the data to within 4% of the measured value. Also what is interesting about this site is that the modelled ALC HFC values correspond closely to those calculated for ligand A which could imply that the site 3 adduct positions on this ligand have the highest formation probabilities.

Lastly there is site 1 which corresponds exactly to the modelled value for ALC5. It is not surprising that this site corresponds the best with the data as it is the site that is least perturbed by the asymmetry of the ligands and by the positioning of the radical at the given site in the detectable region. Assuming the same site allocations above it is clear to see that the HFC values published by McKenzie differ by a factor of approximately 20% from the values in the data. Hence, this confirms that these DFT calculations do not represent the data well and need to be modified to sufficiently incorporate the crystal structure of the sample. [208]

Chapter 7

Electron Spin Relaxation in The Functionalised Acenes

7.1 Electron Spin Relaxation

7.1.1 TIPS-Pentacene

It can be shown in the case of functionalised acenes that there is an eSR present, that is irrespective of morphology of the sample, from the ALC-MuSR data published in reference [209]. Having extracted the ALCs for the TIPS-Pentacene at 10 K and 300 K from the data taken on the ARGUS spectrometer it is clear to see the difference in amplitudes of the ALCs at the different temperatures. Figure 7.1 shows the time integrated data plotted for both temperatures around the resonance. The most striking feature is the large increase in amplitude of the ALC at 300 K with most importantly no change to the shape or width of the ALC. This behaviour is resemblant of the eSR modelled in Section 5.1 where it was shown that for an increase in the eSR the amplitude of the ALC increased also without other significant changes.

It is also clear to see the influences expected from a change in eSR in the muons spin relaxation. Figure 7.2a shows the time resolved polarisation data for the TIPS-Pentacene at 0.27 T for 10 K and 300 K. It is quite apparent that there is a much larger relaxation rate at 300 K. In a typical ALC the loss of polarisation expresses itself as a loss of asymmetry only not as a relaxation. However, it is quite clear from Figures 7.2a an 7.2b that the muon spin relaxation is present throughout the whole ALC and not just at the minima and that the peak increase in relaxation rate corresponds to the position of the ALC. To obtain Figure 7.2b the time resolved data in Figure 7.2a was fitted with an exponential relaxation function for all the magnetic fields and the characteristic relaxation rate was plotted as a function of field. The typical power law trend for the relaxation rate can be seen in Figure 7.2b for both

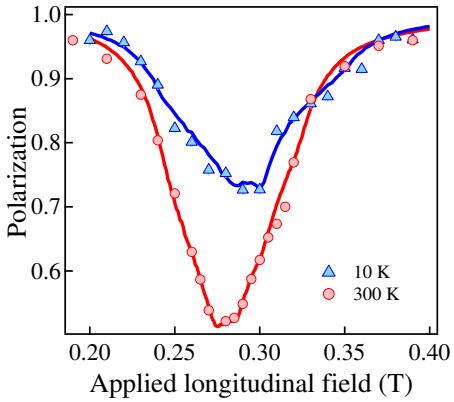

Figure 7.1: Group 1 ALC in TIPS-Pentacene plotted at 10 K and 300 K with modelling results shown as solid lines

temperatures plotted as solid lines. The power law originates from the spectral density function for the relaxation rate and In the case of a lorentzian spectral density for which the relaxation data is an exponential the power law becomes $B^{-1/2}$. These lines highlight the peak in relaxation rate around the resonance. Thus far an additional eSR is the only known phenonema to explain the temperature dependant depth changes in the ALC [209] without changes in the width or shape.

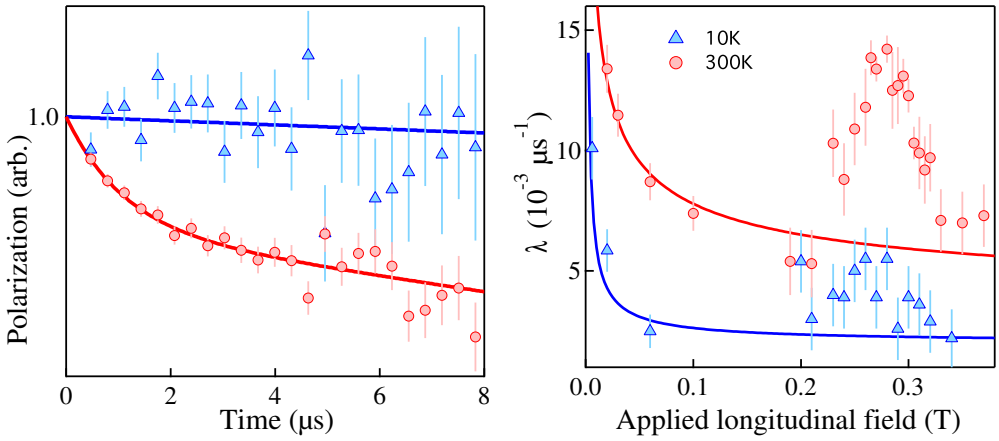

(a) Polarisation time resolved data for TIPS-Pentacene at 10 K and 300 K with exponential fits shown as solid lines

(b) Relaxation rate against applied magnetic field for TIPS-Pentacene at 10 K and 300 K with typical power law fits shown as solid line

Figure 7.2: Relaxation data in TIPS-Pentacene

It is worth noting at this point that having allocated all the muon sites earlier the most intense ALC, group 1, has been focused on in all of the TIPS-Pentacene work. The ALC data was modelled with the method described in Chapter 6 and the eSR parameter was extracted. The sensitivity limit of the eSR is in the order of 0.01 MHz and at 10 K therefore the eSR was assumed to be 0.02 MHz. The same two independent ALCs mentioned earlier were used and had relative amplitudes of 0.64 and 0.32 for ALC 1 and ALC 2 respectively. The 10 K data modelling allows

for the determination of the experimental units to polarisation scaling factors that are o be used for the modelling of the 300 K. The final modelling can be seen as the solid lines in Figure 7.1 and the increase in amplitude of the ALC is accounted for by increasing the eSR. The values extracted were 0.02±0.01 MHz at 10 K and 0.76±0.03 MHz at 300 K. The increase confirms the presence of an additional eSR in the TIPS-Pentacene.

7.1.2 Rubrene

Having established the presence of an eSR in the TIPS-Pentacene it is necessary to determine the nature of the eSR. In order to understand if the eSR is a local phenomena or one that is transport related the same measurements were performed in Rubrene. The key difference between the Rubrene and the TIPS-Pentacene is the morphology of the sample. The Rubrene is amorphous and consequently has an extremely low (nearly zero) mobility. On the other hand, the TIPS-Pentacene is poly crystalline and possesses a much higher mobility. If the eSR is still present in the Rubrene then it would imply that the eSR is an intra-molecular phenomena. The ALCs were extracted from the data in the method reported earlier and the results are plotted in Figure 7.3 for 1.8 K, 10 K, 25 K, 50 K, 100 K and 280 K.

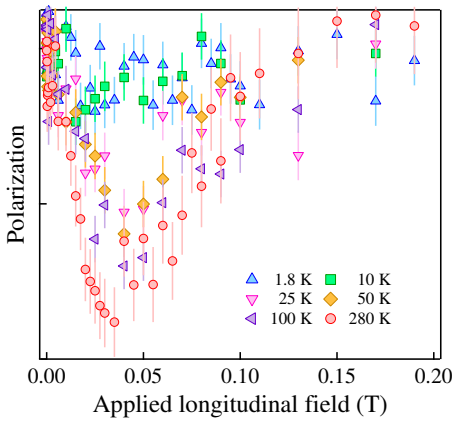

Figure 7.3: ALC resonance in Rubrene plotted for six temperatures

The ALCs are extremely broad which makes it difficult to extract the the exact line shape of the ALC but it is still possible to gain qualitative information from the ALCs. There are two important features in the Rubrene data. The first of these is the broadness of the ALCs. This can easily be understood by considering the amorphous nature of the sample. This will produce a distribution of HFCs which overlap to give a broadening of the over all ALC as there are many environments in which the muon can stop. The second feature is the much lower position of the ALCs compared to the Pentacene derivatives which are around 0.3 T. This could be due to the fact that the muon site is on the ligand rather then on the backbone which is quite plausible. In this case the HFC between the electron and the muon

may be weakened as the electron wave-function is delocalised across the backbone not the ligand creating an effect analogous to a "bottle-neck".

The most striking feature in the data however is that despite the amorphous nature there is still a distinct presence of the increasing amplitude with temperature. Although the ALCs are broad to model reliably and extract a quantitative eSR it is still possible to compare the relaxation data. As in the case of the TIPS-Pentacene there is a clear increase in the relaxation at 280 K compared to the 10 K polarisation. This can be seen in Figure 7.4a. Once again the time resolved data can be fitted with an exponential relaxation function (solid lines) to extract the relaxation rate for all the fields. The resultant data is plotted in Figure 7.4b and it is immediately possible to see the peak in the relaxation rate at the resonance that also occurred in the TIPS-Pentacene. This shows that the same eSR is present in the Rubrene as well as the TIPS-Pentacene and strongly suggesting that the eSR is indeed an intra-molecular process that is also more general to all functionalised acenes.

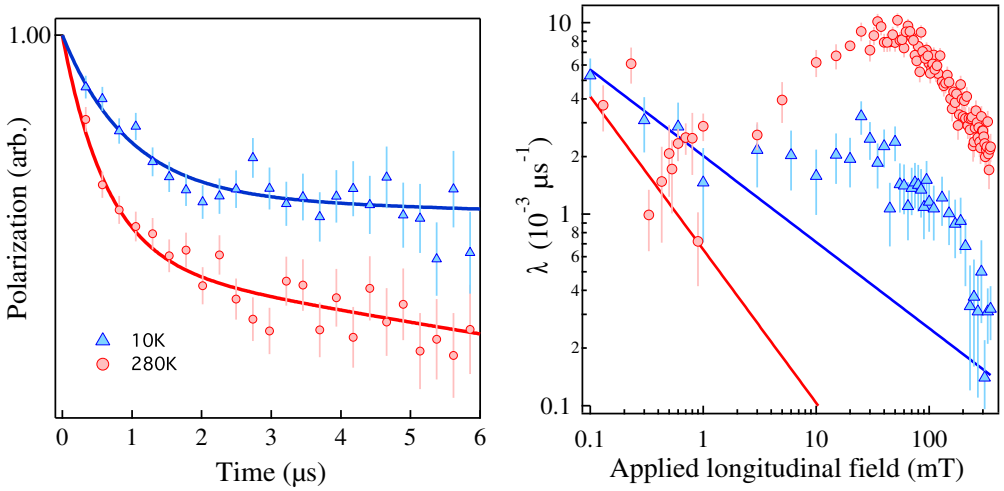

(a) Polarisation time resolved data for Rubrene at 10 K and 280 K with exponential fits shown as solid lines

(b) Relaxation rate against applied magnetic field for Rubrene at 10 K and 280 K with typical power law fits shown as solid lines

Figure 7.4: Relaxation data for Rubrene

7.2 TIPS-Pentacene vs. Deuterated TIPS-Pentacene

In the previous sections it was shown that there is an additional eSR present in the functionalised acenes and that it was an intra-molecular phenomena. In order to further understand the nature of the eSR it is important to determine the mechanism behind the eSR and this essentially is the driving force behind the rest of the work presented in this thesis. There were two mechanisms discussed in Chapter 2, the HFI and the SO interaction and in each case models were preposed like those of

Bobbert and Eliott-Yaffet which tried to describe the spin relaxation in organic semiconductors. In the measurements discussed so far the energy scales in the system raise some questions over the HFI.

In the case of Bobbert's model the electron experiences a vast array of random HFIs as it interacts with the nuclei in the system and therefore its spin relaxes. However, in the muon experiments any nuclear HFIs have been quenched as the nuclear HFCs are of the order of a few mT and therefore the application of a magnetic field much larger than this (a factor of 1000) would act to decouple any nuclear HFIs. This was discussed earlier in the case of the repolarisation curve where the muons start to recover their polarisation as the magnetic field is increased. It is also possible to see this decoupling in the relaxation rate. If the initial part of the relaxation rate with field is focused on as in Figure 7.5 it is clear to see that the relaxation rate starts to drop of after a few mT which is expected as the nuclear HFIs decouple and no longer cause the muons spin to relax.

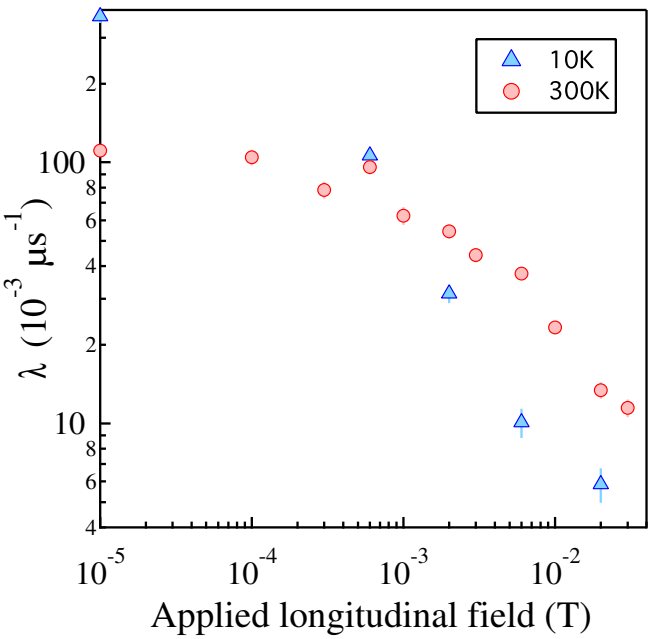

Figure 7.5: Relaxation rate against applied magnetic field for 10 K and 300 K at low fields showing the decoupling of nuclear HFCs

There is also another way to study any effects from the nuclear HFIs. A simple test exists to change the strength of the HFI and therefore alter the size of the spin relaxation in the system. This test involves deuterating the molecule so that the hydrogens are all substituted for the heavier deuterium. This is useful as one of the properties of the deuterium is that the magnetic moment is around a third of the size of that in Hydrogen. The dependence of the HFI on the magnetic moment was derived earlier and was shown to have a linear relationship. It is therefore expected that any decrease in the magnetic moment would also cause a decrease in the HFI. The magnetic moment in Deuterium is 0.857 μ_N compared to that of Hydrogen

which is 2.7928 μ_N, where μ_N is the Bohr magneton unit. This is a reduction of over two thirds and hence should have the same decrease in the HFI. If the eSR is a result of the nuclear HFIs then there should be a substantial decrease in the eSR also. Given the dependency of the amplitude of the ALC on the eSR the ALCs provide a novel way of tracking any effects from the change of the HFI. In order to test the HFI TIPS-Pentacene was fully deuterated and the ALCs compared between the protonated and deuterated samples.

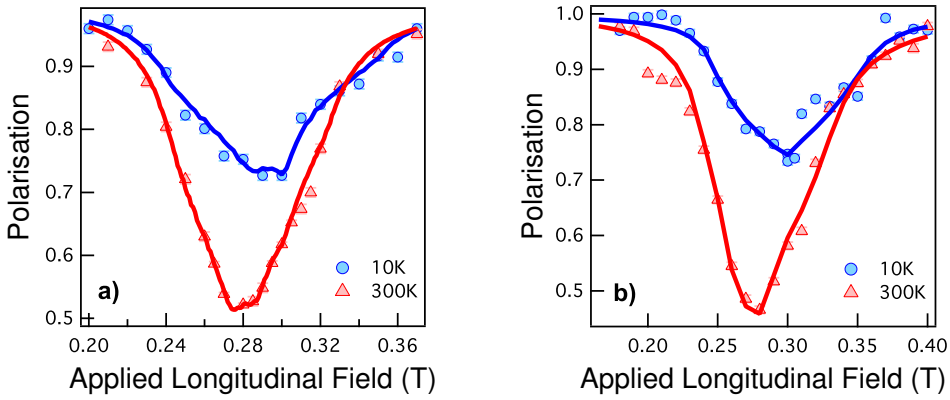

Figure 7.6: ALC resonances for a) TIPS-Penacene and b) deuterated TIPS-Pentacene at 10 K and 300 K with modelling results shown as solid lines

Table 7.1: TIPS- Pentacene model parameters

	A (MHz)	**D (MHz)**	**E (MHz)**	**eSR (μs^{-1})**
10K				
ALC 1	72.5±0.5	−5.0±1.0	5.0±1.0	0.02
ALC 2	84.5±0.6	10.0±0.8	5.0±1.0	0.02
300K				
ALC 1	70.7±0.4	−5.0±0.5	5.0±1.0	0.77±0.04
ALC 2	79.0±0.3	9.0±0.7	5.0±1.0	0.75±0.04

Figure 7.6 shows the time integrated asymmetry around the group 1 resonance reported earlier in both the TIPS-Pentacene and the deuterated TIPS-Pentacene (DTIPS-Pentacene). It is immediately possible to see that the increase in the amplitudes at 300 K is very similar in both the protonated and deuterated samples. It is also worth noting that the DTIPS-Pentacene measurements were taken on the DOLLY spectrometer but are consistent with the results from the ARGUS spectrometer. The ALC positions and shapes are very much the same. The ratio between the largest amplitudes at 10 K and 300 K is approximately 1.6 in both the samples which gives a quantitative indication that the eSR is not effected by the deuteration. To confirm this the data were modelled in the same manor as before. The results of

these models can be seen in Figure 7.6 as solid lines and the average eSR values extracted were 0.74±0.05 MHz in both the samples. The modelling parameters can be seen in Tables 7.1 and 7.2. This result leads to the conclusion that the deuteration of the sample is causing no reduction of the eSR as the amplitude is not decreasing. Furthermore this would imply that the HFIs of the nuclei are behaving as expected on the application of a large magnetic field and decoupling from the muons spin resulting in no effect on the eSR. On the other hand the SO interaction would not be expected to change with magnetic moment therefore could still be consistent with the deuteration data. Also the energy scales of the SO interaction are more consistent with the energy scales of the muon measurements, being in the order of 1000's of Gauss up in to the Tesla range in terms of the magnetic field. This leaves some doubt as to whether the dominant mechanism behind he eSR is in fact the SO interaction not the HFI and it is this that inspires the following studies in this thesis.

Table 7.2: DTIPS- Pentacene model parameters

	A (MHz)	**D (MHz)**	**E (MHz)**	**eSR (μs^{-1})**
10K				
ALC 1	75.0±0.7	−9.0±0.7	5.0±1.1	0.02
ALC 2	86.4±0.8	9.0±0.7	1.0±0.2	0.02
300K				
ALC 1	73.3±1.0	−6.3±0.5	4.0±0.3	0.76±0.03
ALC 2	82.6±1.2	5.5±0.5	4.0±0.3	0.76±0.03

7.3 Determining the Source of Electron Spin Relaxation Through the Muon Spin Deploarisation

One point that remains to be addressed in the study of TIPS-Pentacene is to determine the source of the eSR for which there are two main possibilities. The first of these is that the eSR originates from the electrons ionised in the path of the muon as it thermalises. These are denoted "track" electrons and are discussed in detail by Storchak et al. in reference [182] and [210]. The second of the possibilities is that the eSR originates from the electron captured by the muonium which is in a bound state on the molecule. The likelihood of the track electrons causing the eSR is determined by Storchak et al. to be dependant on the distance between the final stopping position of the muon and the average position of the last track electron. They evaluate this to be in the order of 0.05 μm. In order to have an effect on the

eSR that is detectable by the muons spin depolarisation the track electrons must be in close enough proximity to the muon in the timeframe of the measurements. This can be calculated approximately from the mobility for the small organic molecules presented in this thesis.

In the case of TIPS-Pentacene the mobility is in the order of 1 cm^2/Vs therefore in a period, t, the electrons can travel a distance, d, given by equation 7.1

$$d = \mu \times t \times E_{\mathrm{Loc}} \tag{7.1}$$

E_{Loc} is the weak Coulombic electric field present in the case where no external electric field is applied. The formula given by Storchak et al. to approximate this is:

$$E_{\mathrm{Loc}} = \frac{e}{\epsilon_r r^2} \tag{7.2}$$

where ϵ_r is the dielectric constant in F/m and r is the average distance of the track electrons from the muon. An approximate value for r is given by Storchak et al. [182] as 5E-8 m and a typical dielectric constant for organic semiconductors such as Pentacene is given as $3.15\epsilon_0$ [182]. Using these values and equation 7.2 the value for E_{Loc} can be calculated and gives a result of 2.3 MV/m. If one considers a time period of 1 μs (this is comparable to the relaxation times in muSR) and taking the highest mobility of 1 cm^2/Vs given for TIPS-Pentacene then equation 7.1 can be applied. The distance therefore the track electrons can travel in this period is in the order of 230 μm. This is much greater then the distance to the muon and would imply that these electrons may have already dispersed throughout the sample before the time window of the muon measurements and as a result should not influence the eSR measurements.

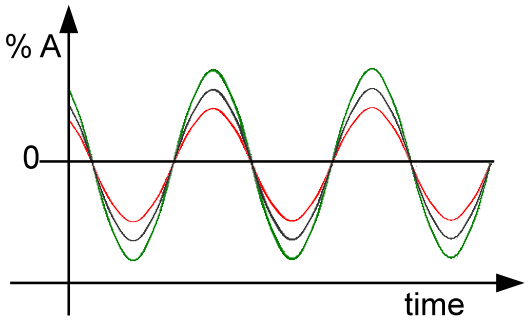

(a) Expected effect on time-resolved TF data upon the application of an electric field as a consequence of diamagnetic fraction changes where red = -5 kV, green = +5 kV and grey = 0 kV

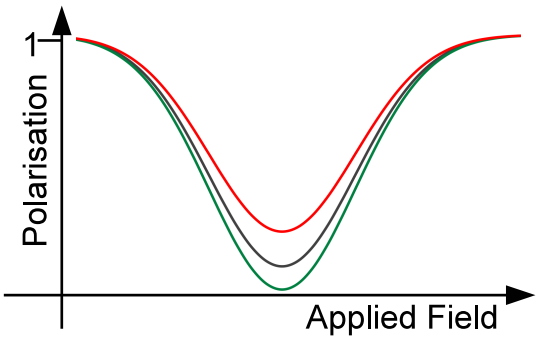

(b) Expected effect on the amplitude of the ALC upon the application of an electric field from additional relaxation processes where red = +5 kV, green = -5 kV and grey = 0 kV

Figure 7.7: Electric field effects from track electrons

In order to confirm this the MuSR measurements can be carried out in the presence of an electric field. There are two main ways that the track electrons can effect the MuSR measurements. The electrons could alter the muon formation, through the delayed processes described by Storchak et al. [182], which would have an effect on the diamagnetic fraction of muons in the sample. In turn this would be reflected in the TF-MuSR measurements. A decrease or increase in the muonium formation would cause an increase or decrease in the diamagnetic fraction respectively. This would result in a corresponding increase or decrease in the amplitude of the oscillations in the asymmetry in the TF measurements. Alternatively the electrons could interact with the electron bound to the muon if they are in close enough proximity inducing an eSR detectable by the muon. This would be present in the ALC measurements in the form of an increase or decrease to the amplitude of the ALC with an increase or decrease of eSR respectively. These are illustrated in figures 7.7a and 7.7b.

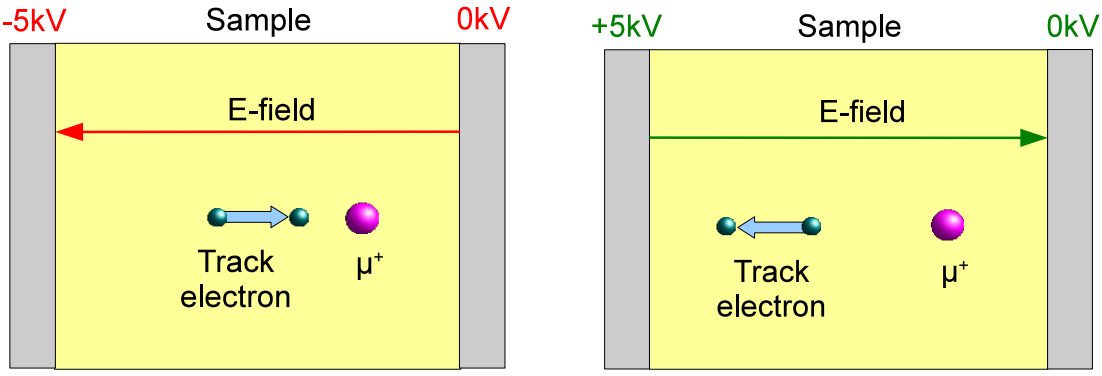

(a) Effect on track electron in the presence of a negative electric field

(b) Effect on track electron in the presence of a positive electric field

Figure 7.8: Application different electric fields

Through the application of an electric field the influence of these effects can be altered if the track electrons are not already dispersed before the time window of the measurement. The effect of applying both a positive and negative electric field can be seen in figures 7.8a and 7.8b. Depending on the direction the electric field is applied (with or against the momentum of the muons) the track electrons will be drawn away from or towards the muons. In turn this will reduce or enhance any effects resulting from the track electrons. This measurement was carried out in TIPS-Pentacene using the EMU spectrometer at ISIS. The sample weighing ∼0.5 g was pressed in to a pellet, using a standard dye press, from the powder form. The diameter of the pellet was approximately 1 cm and the pellet was mounted in the adapted sample holder described in Section 3.2.

In order to obtain both a positive and negative electric field a voltage was applied to the top titanium electrode. This sequence can be seen in figure 7.9 and is continually cycled throughout the muon measurement. The data is later filtered using the

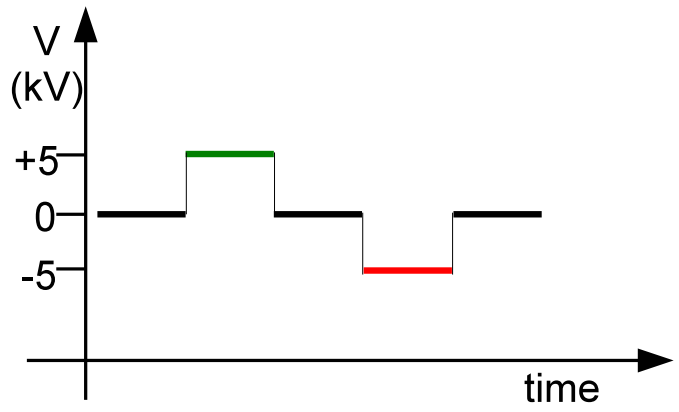

Figure 7.9: Pulse sequence for electric field experiment. Note the pulse widths are not to scale in this diagram; the pulse width for the positive and negative fields is 10 s and the pulse width for the zero field is 5 s

WIMDA software in to positive, negative, and zero electric field bins and the events are co-added in each bin. In the TIPS-Pentacene electric field measurements a positive voltage of 5 kV and a negative voltage of -5 kV were used to produce the electric fields. The purpose of the zero electric field is to ascertain a direct comparison with the effects of switching on the electric field.

The first set of data presented here is the TF measurements. As mentioned before the electric field will cause a shift in the effect of the track electrons on the muonium formation. In the case of a positive field the electron will be drawn away from the muon (figure 7.8b) which would in turn reduce the muonium formation. A decrease of muonium would increase the diamagnetic fraction of muons in the sample and consequently increase the amplitude of the asymmetry in the TF-MuSR measurements. Alternatively the application of a negative field would act as to draw the track electrons towards the muons (figure 7.8a). This would have an opposite effect to those described for the positive field.

Figure 7.10 shows the time resolved asymmetry at a field of 20G for the +5 kV (green), −5 kV (blue) and zero (red) electric fields. It is clear to see that the amplitudes of the oscillations appear the same within the scatter on the data for all the electric fields. This was checked quantitively by fitting the data with a relaxing oscillation function and extracting the relaxing asymmetry. The values obtained were $12.62 \pm 0.14\%$ for +5 kV, $12.56 \pm 0.14\%$ for −5 kV and $12.26 \pm 0.14\%$ for 0 kV. These results confirm that there is no measurable change in the amplitude in the presence of either electric field. This strongly suggests that if the track electrons are not already dispersed they are not having any direct effect on the muonium formation.

The next set of data presented are the results of the ALC measurements for TIPS-Pentacene in the presence of an electric field. If the electric field were drawing the track electrons towards the muons then they may see an additional eSR from the

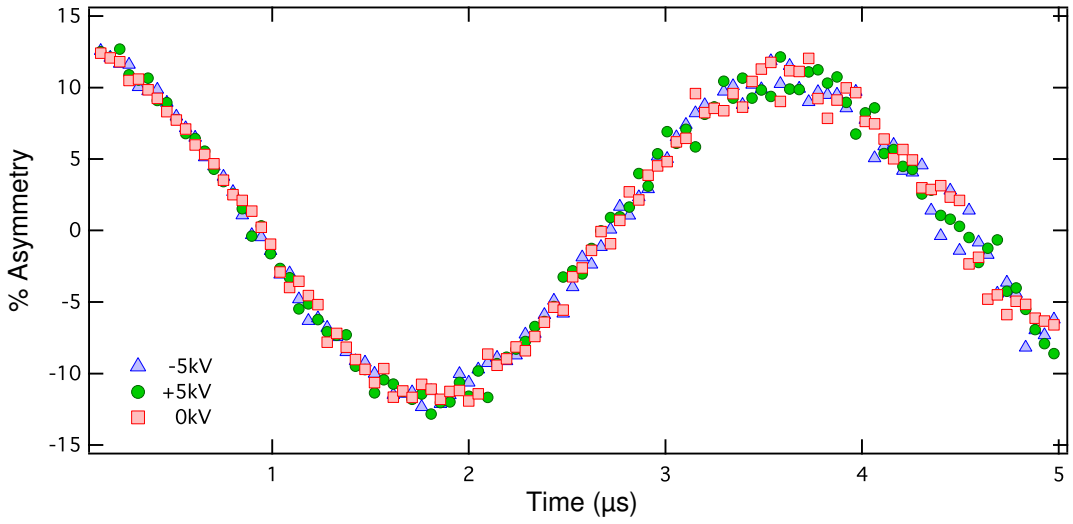

Figure 7.10: Time resolved TF data for TIPS-Pentacene at 300 K for the three electric fields with a magnetic field of 20 G

interaction of the bound electron with the free moving track electron. This would be seen as an overall increase in the eSR at the resonance field. Hence the expected result would be an increase in the muons depolarisation and in the amplitude of the measured ALC. However if the track electrons were drawn away from the muons as in the case of a positive electric field then this would proceed to reduce any eSR effects present from the track electrons.

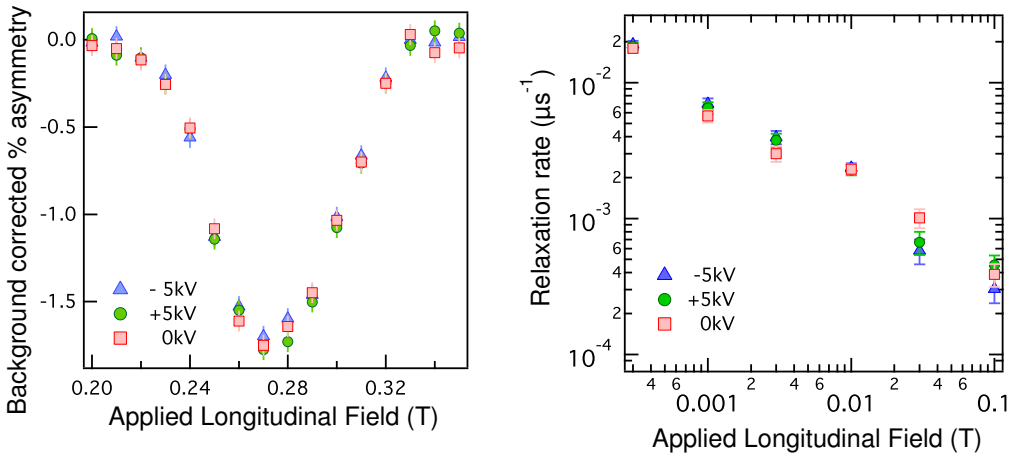

(a) ALC resonances for TIPS-Pentacene as a function of an applied electric field of +5 kV (green circles) and -5 kV (blue triangles). Measurements in zero electric field are also shown for comparison (red sqaures)

(b) Off resonance relaxation data as a function of an applied electric field of +5 kV (green circles) and -5 kV (blue triangles). Measurements in zero electric field are also shown for comparison (red sqaures)

Figure 7.11: Electric field data in the presence of an applied longitudinal field

Figure 7.11a shows the time integrated data around the resonance in TIPS-Pentacene and it is consistent with the data measured on ARGUS and GPS reported earlier. The data is plotted at three fields and it is immediately apparent that the data shows

no difference in the amplitude of the ALC between the electric field being present and the zero field. This result is also confirmed by the off resonance relaxation data. This data is plotted in Figure 7.11b again for all three electric fields. The relaxation rate values were extracted by fitting the time resolved data in WIMDA with a lorenzian relaxation function for each magnetic field. It is also clear in this plot that there is no effect from the presence of either the positive or negative electric fields and the relaxation rates are the same within the errors. The combination of the TIPS-Pentacene results reported in this section lead to the conclusion that there is no clear influence from the track electrons on either the muonium formation or the eSR and instead support the idea that the eSR originates from the captured electron in the bound muonium state. However, this is not the case for all the small organic molecules in this thesis and in fact there appears to be an effect on the relaxation rate from the electric field in AlQ_3 . This is reported by Drew et al. [151] who conduct a similar experiment to that described above for TIPS-Pentacene and they see a clear shift in the off resonance data. Their results are shown in figure 7.12 [151] and they apply a negative and a zero electric field to the sample.

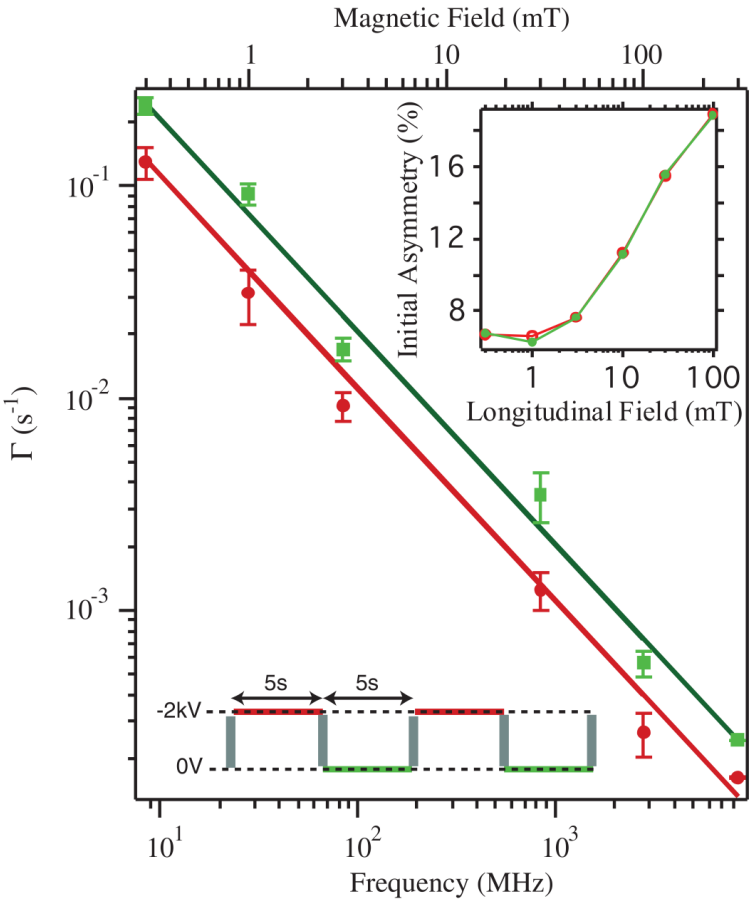

Figure 7.12: Data for electric field experiment on AlQ_3 by Drew et al. showing the relaxation rate alter upon the application of an electric field. Lower inset shows the electric field pulse sequence and upper inset shows the repolarisation curve

In order to consider the difference between the two sets of electric field data one must

must first consider the mobilities in the two samples as this is key to the effects seen from the track electrons. In the case of the AlQ_3 the mobility is much lower then that of the TIPS-Pentacene. If equation 7.1 is applied to the AlQ_3 then the result is significantly different and for a mobility of 1.4E-6 cm^2/Vs the distance travelled by the track electron in 1 μs is in the order of 3 Å. This is a factor of 100 less then the distance between the track electrons and the muon. Therefore in the AlQ_3 the electrons do not disperse rapidly as in the TIPS-Pentacene. This is important as the electric field is able to act on the track electrons in the timeframe of the muon measurement resulting in a clear field dependance in the relaxation data. However, there is still no effect on the muonium formation. It is therefore clear that in TIPS-Pentacene the mobility of the molecule allows the track electrons to disperse rapidly in the sample and nullify any effects from the electric field and hence this is why there is no evidence of these electrons in any of the data.

Chapter 8

Z-Dependence Study in the Quinolate and TES Series

The last highlighted the importance of understanding the mechanism behind spin relaxation in small organic molecules. One of the key points in the SO interaction is the dependence on the atomic number (Z-number). It was shown earlier that the Hydrogen-like Z^4 dependence can easily be derived. This direct Z-dependence, however, is not present in the HFI hence by studying the Z-dependence of the eSR an insight in to the underlying mechanism can be gained. The systems in this thesis are not Hydrogen-like so do not have the ideal potential of the Hydrogen atom. It is for this reason that the Z-dependence is expected to deviate from the typical Z^4 dependence in Hydrogen. This section looks at two series of substituted molecules, the Quinolate series and the TES series. In both cases there is one atom substituted by a heavier counterpart. The atoms are carefully chosen in order to rule out any direct or indirect HFIs.

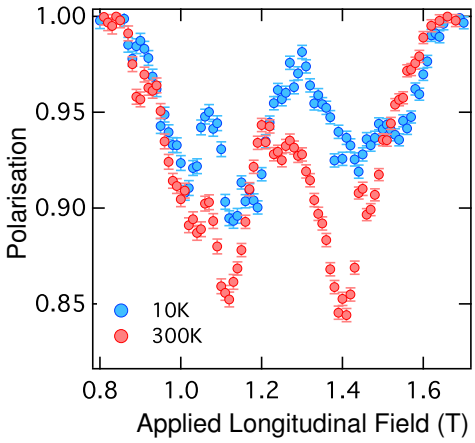

Figure 8.1: ALC resonance for AlQ_3 at 10 K and 300 K taken on the ALC spectrometer

8.1 The Quinolate Series

The first series considered is the Quinolate series. In this series the central ion is substituted from Aluminium to Gallium, Indium and Bismuth. The Quinolate molecules have a very different structure to the previously reported TIPS-Pentacene and Rubrene so in order to prove the generality of the eSR to all small organic molecules it is necessary to first present the relaxation rate data in AlQ_3 . Figure 8.1 shows the extracted ALC for AlQ_3 at 10 K and 300 K. It is quite clear that the same increase in amplitude without change to the shape or width of the ALC is still present in the Quinolate molecule. The ALC in AlQ_3 is quite broad in comparison to the TIPS-Pentacene presented earlier. This is due to there being a combination of more sites and conformations then in the TIPS-Pentacene which as discussed previously causes an overlap of several HFCs broadening the ALC.

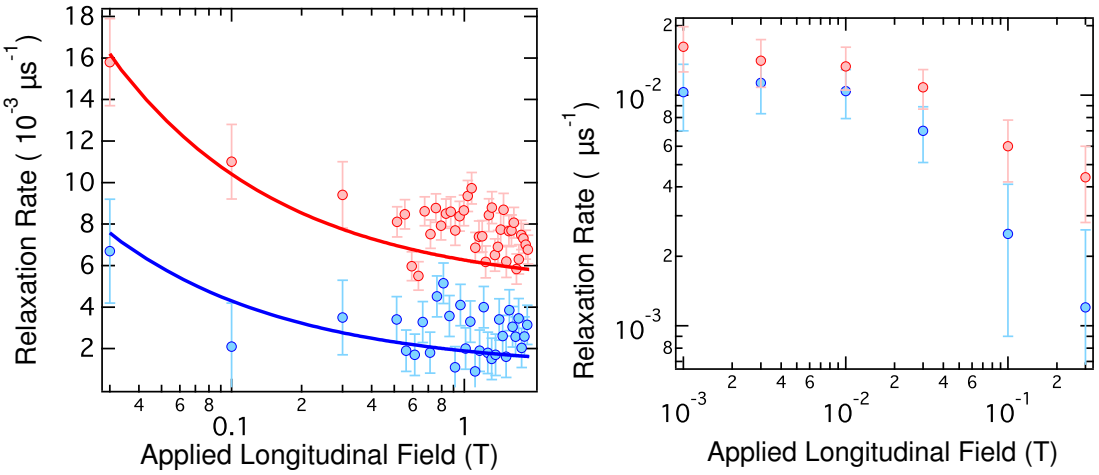

(a) Relaxation rate against magnetic field for AlQ_3 at 10 K and 300 K with typical power law fits shown as solid lines

(b) Relaxation rate at low fields for AlQ_3 at 10 K and 300 K showing the decoupling field

Figure 8.2: Relaxation data in AlQ_3

Figure 8.2a shows the relaxation rate with applied magnetic field at 10 K and 300 K in AlQ_3 . The key feature of the data is the presence of the increase in relaxation rate in the region of the ALC. It is hard to see a change in the height of this peak with the change in temperature as the combination of a very broad ALC with the low number of events measured on the HIFI spectrometer induces a lot of scatter in the data. The relaxation rate was obtained by fitting the time resolved polarisation data to an exponential function as before for all the magnetic fields. This data is consistent also with the time integrated data taken on the ALC spectrometer at PSI which is presented later. This data proves that the eSR is in fact more general to all small organic molecules and in addition the Quinolate series can be used to study the Z-dependence of the eSR. One last point to note about the relaxation data is that the energy scales are even more consistent with the decoupling of the nuclear

HFIs. This is shown by the drop off in the relaxation rate in Figure 8.2b at a few 100 Gauss at which point the muons start to recover their polarisation.

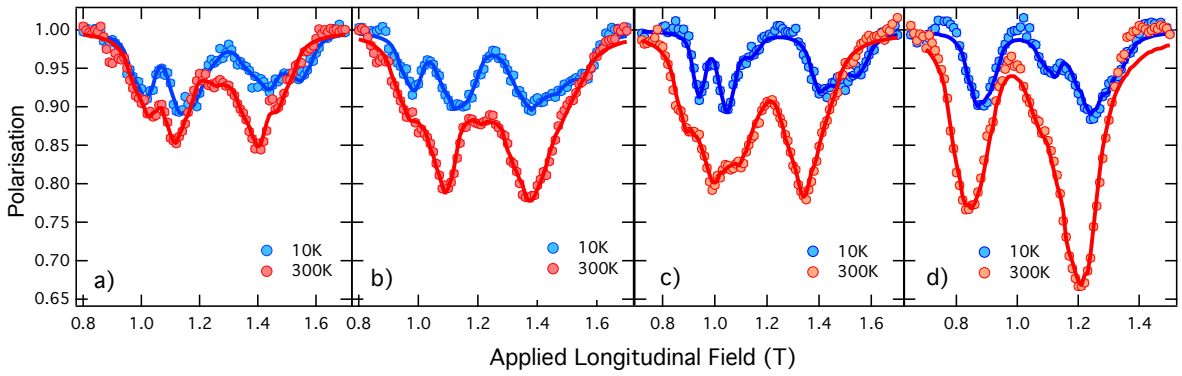

Figure 8.3: ALC spectra at 10 K and 300 K for: a) AlQ3, b) GaQ3, c) InQ3, d) BiQ3 with modelling results (solid lines)

Table 8.1: AlQ3 and GaQ3 model parameters where A, D and E are in MHz and eSR is in μs^{-1}

	A	**D**	**E**	**eSR**	**A**	**D**	**E**	**eSR**
10K								
ALC 1	274±2	10±2	15.0±3	0.02	266±2	9±2	13±3	0.02
ALC 2	311±2	14±2	10.0±3	0.02	305±2	14±2	15±3	0.02
ALC 3	329±2	15±2	13.0±3	0.02	321±2	8±2	11±3	0.02
ALC 4	386±2	14±5	24.0±6	0.02	378±2	23±5	18±6	0.02
ALC 5	420±2	12±2	15.0±3	0.02	417±2	5±2	24±3	0.02
300K								
ALC 1	276±2	12±2	11±3	0.06±0.02	263±2	15±2	15±3	0.08±0.02
ALC 2	306±2	14±2	11±3	0.20±0.02	295±2	15±2	15±3	1.00±0.02
ALC 3	344±2	16±2	12±3	0.11±0.02	328±2	14±2	14±3	0.90±0.02
ALC 4	378±2	10±5	14±6	0.77±0.20	372±2	20±5	20±6	1.10±0.20
ALC 5	403±2	13±2	18±3	0.10±0.02	405±2	17±2	17±3	0.10±0.02

The ALC data for all four quinolates at 10K and 300 K can be seen in figure 8.3. The background was removed using local fourth order polynomials as reported in the TIPS-Pentacene section. The resonances are all situated between 0.8 and 1.6 T and exhibit the increase in amplitude seen previously with an increase from 10 K to 300 K. This confirms again that the eSR is present in all four of the molecules and behaves in much the same manner as expected from past studies. What is most striking about the spectra is that the 10 K amplitudes are almost exactly the same throughout the series but the 300 K amplitudes rapidly increase. This makes it remarkably clear to see the increase in the ratio between the 300 K and 10 K data. The amplitudes of the lowest points for 10 K and 300 K can be seen plotted in Figure 8.4, highlighting this trend in the data. As in the case of TIPS-/DTIPS-

Table 8.2: InQ3 and BiQ3 model parameters where A, D and E are in MHz and eSR is in μs^{-1}

	A	D	E	eSR	A	D	E	eSR
10K								
ALC 1	256±2	7±2	7±3	0.02	235±2	8±2	10±3	0.02
ALC 2	285±2	9±2	9±3	0.02	248±2	8±2	8±3	0.02
ALC 3	310±2	10±2	10±3	0.02	302±2	8±2	15±3	0.02
ALC 4	385±2	15±5	9±6	0.02	334±2	10±5	15±6	0.02
ALC 5	417±2	15±2	22±3	0.02	355±2	15±5	10±6	0.02
300K								
ALC 1	243±2	13±2	11±3	0.03±0.02	224±2	11±2	11±3	0.90±0.02
ALC 2	278±2	24±2	11±3	0.50±0.02	240±2	10±2	11±3	0.80±0.02
ALC 3	308±2	25±2	11±3	1.40±0.02	294±2	14±2	12±3	0.05±0.02
ALC 4	359±2	9±5	18±6	1.60±0.20	326±2	12±5	14±6	3.50±0.20
ALC 5	382±2	16±5	9±6	0.55±0.20	330±2	10±5	18±6	1.50±0.20

pentacene this gives a qualitative indication that the eSR is also increasing with Z-number.

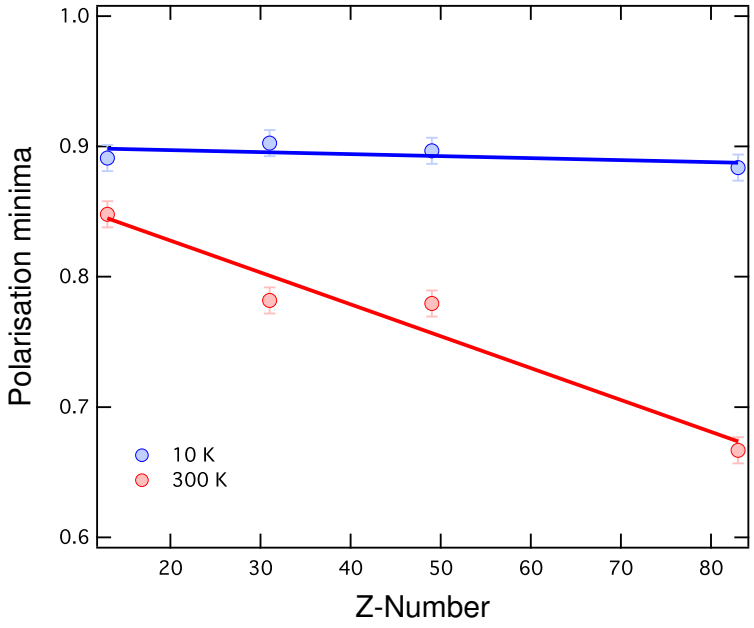

Figure 8.4: Minima of ALC resonances at 10 K and 300 K against Z-number with lines to guide the eye

The spectra taken at 300 K were modelled to obtain the quantitative eSR values again using powder averaging but with 3000 Monte Carlo steps. There were five independent resonances used corresponding to the five muon sites discussed earlier and the values obtained for all the parameters at 10 K and 300 K are reported in tables 8.1 and 8.2. The results from the modelling are also shown as solid lines in figure 8.3 and as expected the ratios are increasing. Figure 8.5 shows the

increase in the average eSR values plotted against the Z-number. It is immediately clear that the eSR is increasing with the Z-number and that the dependance is linear consistent with a Z^1 power law. It has already been shown that the HFI has no direct relationship to the Z-number and so if it were the dominant mechanism one would not expect to see a change in eSR with Z-number. This supports the deuteration results and the work presented on TIPS-Pentacene and Rubrene that contradict a HFI based model for spin relaxation.

In contrast, if the SO interaction was the dominant mechanism then the Z-dependence would be expected to follow a power law. The data is constant with this hypothesis and in deed as the system is not hydrogen like the power law is Z^1 not Z^4. This follows from the reasoning discussed earlier in which the variation of the potential in the system causes the Z-dependence to deviate from the hydrogen-like Z^4 dependence to become an altered power law Z^n where in this case $n = 1$. It is worth noting at this point that the HFI cannot be ruled out on the Z-dependence of just the Quinolate series as there may be other direct or indirect effects present. One such effect may come directly from the substituted atom. As the central atom is changed all the chemical properties of the atom change also, not just the atomic number. One of these properties is the magnetic moment of the atom. As described in the deuteration work the HFI is directly related to the magnetic moment of the atom. If the magnetic moment is increased then the HFI will be also. This can be checked by considering the data in Figure 8.5.

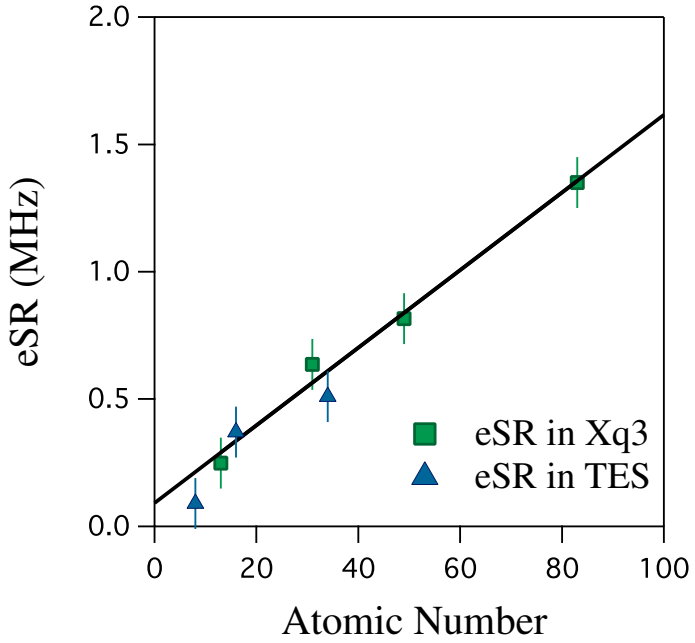

Figure 8.5: The eSR at 300 K plotted against Z-number for the quinolate (green squares) and TES (blue triangles) series fitted with a straight line (solid black line)

Firstly the magnetic moment of Aluminium is 3.64 μ_N and the magnetic moment of Gallium is 2.01 μ_N where μ_N is the Bohr magneton. Therefore the change from

Aluminium to Gallium is a reduction in the magnetic moment of just under 50%. The dependence on the magnetic moment of the HFI is linear so there should be a similar order decrease in the eSR. This is not the case and in fact there is nearly a factor of three increase in the eSR. In addition if Indium and Bismuth are then considered, the magnetic moment of Indium is 5.54 $\mu_N$and the magnetic moment of Bismuth is 4.11 μ_N. This is a reduction of approximately 20% in the magnetic moment so a reduction in the same order would be expected in the eSR. Again this is not reflected in the data and there is actually an increase in the eSR in the order of 50%.

Some of the indirect effects may arise from the general changes to the energies or population of vibrational states in the system. These can be a result of several things such as changes in size, to the position or shifts in the crystal packing of the molecules. One such change which is quite apparent is the change in bond lengths in the molecule from the larger central atom being slightly differently oriented. Small changes to the bonds like those just described could induce small changes to the population of certain vibrational modes. If the HFI is the mechanism and is coupling to these modes then the change will effect this coupling and hence indirectly the effect eSR. These interactions are ruled out in the next section by using a different series of molecules.

8.2 The TES-Series

In order to rule out these indirect effects the TES series, which has a completely different structure, was studied. Again the ALC spectra were measured at 10 K and 300 K and the background was removed using a local polynomial. The spectra for all three molecules in the series are shown in figure 8.6. The same trend of an increasing ratio with increasing Z-number can be observed although as expected the ALCs are

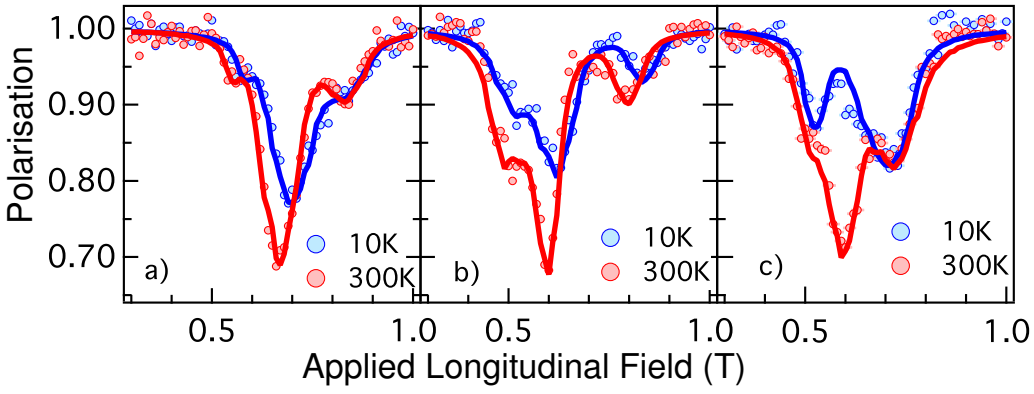

Figure 8.6: ALC resonances at 10 K and 300 K for TES series with modelling results (solid lines)

more resemblant of those in the TIPS-Pentacene molecule owing to the similarities in the chemical structure. This is again indicative of an increase of the eSR with Z-number. The ALC spectra were modelled using powder averaging and with 10000 Monte Carlo steps. In this case three independent resonances corresponding to three muon sites were required to model the TES series. The values for all the parameters for 10 K and 300 K are reported in tables 8.3 and 8.4 and the results of the modelling are shown as solid lines in figure 8.6.

Table 8.3: TES-ADF and TES-ADT model parameters where A, D and E are in MHz and eSR is in μs^{-1}

	A	**D**	**E**	**eSR**	**A**	**D**	**E**	**eSR**
10K								
ALC 1	158±1	5±1	5±2	0.02	142±1	15±1	15±2	0.02
ALC 2	190±1	15±2	15±2	0.02	170±1	12±1	12±2	0.02
ALC 3	227±1	15±2	15±2	0.02	227±1	10±1	10±2	0.02
300K								
ALC 1	150±1	5±1	5±2	0.02±0.02	137±1	15±1	10±2	0.50±0.03
ALC 2	182±1	13±2	13±2	0.18±0.02	163±1	8±1	8±2	0.38±0.03
ALC 3	227±1	13±2	13±2	0.05±0.02	217±1	10±1	10±2	0.22±0.03

Table 8.4: TES-ADS model parameters where A, D and E are in MHz and eSR is in μs^{-1}

	A	**D**	**E**	**eSR**
10K				
ALC 1	143±2	18±2	15±3	0.02
ALC 2	188±2	8±2	8±3	0.02
ALC 3	200±2	10±2	10±3	0.02
300K				
ALC 1	140±1	10±2	10±2	0.71±0.03
ALC 2	162±1	10±2	10±2	0.01±0.01
ALC 3	197±1	15±2	15±2	0.79±0.03

The Z-dependance can also be seen in figure 8.5 and it obeys much the same power law as the quinolate series. This agrees with the Z-dependance expected from the SO interaction. The direct HFI with the substituted atom can once again be ruled out even more so than in the case of the Quinolate series. The substituted atoms in the TES series have more then one natural isotope so there are several magnetic moment values for each atom. The most abundant forms of the atoms have a zero magnetic moment. This makes any direct form of the HFI impossible with these isotopes impossible which alone is quite strong evidence to suggest that the direct HFI can be ruled out of the eSR altogether. However, for the sake of completeness

one needs to consider the effects from any of the other isotopes. The magnetic moments of the additional isotopes of oxygen (for which the abundances are less than 1%) are 0 μ_N and 1.893 μ_N and the magnetic moments for the remaining sulphur isotopes are 0 μ_N and 0.643 μ_N. The zero magnetic moments can be ruled out for the same reasons as above, which leaves a decrease in magnetic moment from 1.893 μ_N to 0.643 μ_N as the only possible source of a HFI. This a decrease of over 50% and so there should be a significant reduction in the eSR between the oxygen and the sulphur. Not surprisingly, the data tells a different story with there being an increase from 0.063 MHz to 0.347 MHz, which is nearly a factor of six increase. Lastly in the series there is the magnetic moments for the selenium which are all zero apart from one isotope with an abundance of 7.63% that has a magnetic moment of 0.503 μ_N. The decrease between sulphur and selenium is not as large as that between the oxygen and sulphur but it should result in a decrease in the eSR. The data shows an increase from 0.347 MHz to 0.503 MHz from sulphur to selenium, a 50% increase. Given all the results from the magnet moment data there is strong cause to rule out any direct effects from the HFI and the substituted atoms.

This leaves the indirect effects. In general these evolve, as mentioned in the previous section, from changes to the energies or population of vibrational states of the molecule. Within one series it is not possible to say whether these effects are occuring. O n the other hand by comparing the two series a more definite conclusion can be drawn. The energies in the TES series are quite different to those in the Quinolate series. These changes are very visible in the difference in the colours of the two samples and in the measured HOMO and LUMO levels. In addition to this the vibrational spectra will be vastly different with the existence of different ligands and backbones compared to central ions. These have different distortion, shearing, stretching and bending modes. Considering these differences the final Z-dependance would be expected to be quite different for each series especially with the simple form of HFI coupling to the population of these modes. However, this leads to perhaps the most poignant result of the Z-dependence study. The Z-dependence of the TES series sits exactly on the same trend as the Quinolate series suggesting that even with the different energies and vibrational modes the process behind the relaxation is more fundamental then that of the HFI. These result which are seen in Figure 8.5 provide srong evidence to rule out the indirect results of the HFI and essentially discount the HFI altogether as the dominant process. This conclusion brings about the last of the major studies completed for the small organic molecules in which the role of the SO interaction and vibrations in the eSR at a fundamental level are investigated.

Chapter 9

Temperature Dependence

It is reported that vibrations present in the small organic molecules may play a role in the eSR [211]. Although this was ruled out in the case of the HFI there is evidence to suggest that an enhanced SO interaction may transpire as a result of a direct coupling between the spin and the vibrations at a molecular level. This in turn would provide a coupling of the eSR to the population of these vibrational states. There are various models to explain the nature of such a coupling, some of which, were discussed in the spin relaxation section. However, one key point that arose from the models is that the coupling has a strong temperature dependance and that it would be logical progression to conduct an in-depth temperature dependance study for some of the small molecules presented in this thesis.

This Chapter looks at the temperature dependance of the eSR studied in the TIPS-Pentacene and Rubrene molecules and compares the results to the temperature dependance study in the Quinolate series. The energy scales involved in the temperature dependant eSR are then extracted and compared to the vibrational spectra for these molecules to give evidence of the vibrational coupling. Lastly one of the models describing the vibrational coupling is applied to the data to try and gain an insight in to the role of any local curvature in the mechanisms behind the eSR.

9.1 TIPS-Pentacene and Rubrene

The full temperature dependance has been measured for both the molecules TIPS-Pentacene and Rubrene. The data for the TIPS-Pentacene was modelled using the same method discussed earlier for all the temperatures and the eSR values were extracted. The data is shown in figure 9.1a and the eSR is plotted on a logarithmic scale against the inverse of the temperature [209]. The first detail to note is that there appears to be two regions to the data, 10-50 K and 100-300 K, with a transition from 50-100 K. The second important feature to note is that the eSR displays a linear

trend in each region, a sign of an Arrhenius behaviour. In order to test this the two regions were fitted with a simple two component Arrhenius function:

$$F(T) = A\exp\left(-E_1/k_BT\right) + B\exp\left(-E_2/k_BT\right) \tag{9.1}$$

For clarity the results from these fits are seen as two separate solid lines in figure 9.1a [209]. As is evident from the figure the fits show a very good agreement with the data, suggesting that the eSR does indeed have an Arrhenius behaviour. This behaviour is not completely unexpected if the the eSR is coupling in some manner to the population of vibrational states. In fact the population of such states would strongly depend on the number of vibrations present in the system and the relationship between the number of states and the temperature is given earlier in the thesis in the discussion of Rybicki's model. He derived an Arrhenius relation with some form of ΔE activation energy, typically in the order of 100 meV. This is not too dissimilar to the function used to fit the data and hence the values can be compared to a certain extent. The energies that are extracted are 19±2 meV in the high temperature region and 3.2±0.2 meV in the low temperature region (153.25 cm^{-1} and 25.81 cm^{-1} respectively).

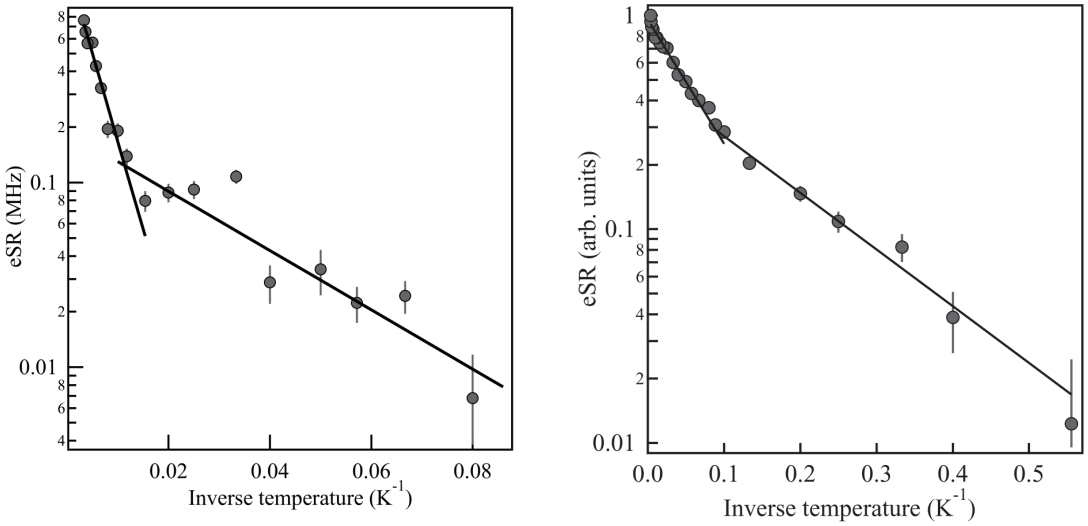

(a) TIPS-Pentacene temperature dependence of the eSR with results from the double Arrhenius fits shown as solid black lines

(b) Rubrene temperature dependence of the eSR with results from the double Arrhenius fits shown as solid black lines

Figure 9.1: Temperature dependance of the eSR

These values naturally differ from that derived by Rybicki owing to the differences in the molecules, but they are still in the order of meV and are still very reasonable. Also it is worth noting that the model had not been applied to the case of small organic molecules which naturally possess a quite different vibrational spectra to the spectra of the molecule being studied by Rybicki. What is interesting is that if the vibrational spectra is calculated for TIPS-Pentacene that has undergone a simple

geometric optimisation then the energy values extracted from the data are very much comparable to the energies in the spectra. The exact vibrations corresponding to the energies in the data will be discussed below, however, what this data does provide is evidence to support the idea of an eSR-vibration population coupling. The specific values extracted from the data correspond to two different vibrations present in the spectra for TIPS pentacene. The first of these, corresponding to the lower energy, is an independent in-plane side to side movement of the unit containing the backbone and silicon. The second higher energy vibration is an out of plane flexing/distortion of the backbone in addition to the movement of the methyl groups on the ligands. These two sets of vibrations can both be seen in files 'High_Energy_TIPS_mode' and 'Low_Energy_TIPS_mode' in the digital appendix and both involve the ligand of the molecule which is what one would expect given the muon site on or around the triple bond. The muon would be particularly sensitive therefore, to vibrations effecting the triple bond which is consistent with the results from the data. Another point of interest is that there appears to be a distinct temperature transition region which allows the population of the higher energy modes which go on to become dominant in the eSR.

Naturally further investigation is needed to understand these two regions and to give a comparison of other small molecules to the TIPS-Pentacene. Hence the same study was also carried out for amorphous Rubrene and the result is shown in figure 9.1b [209]. Again there are two characteristic energy scales, Arrhenius in nature, that are present in the data with a transition in approximately the same region. As mentioned before, owing to the amorphous nature of the Rubrene and distribution of the HFCs the ALCs were too broad to model sufficiently in order to extract quantitative information with respect to the eSR and energy scales. Despite the data not producing quantitative results for the energy scales it does offer the ability to compare the qualitative trends of the eSR. It is clear to see that there are once again the two distinctive regions in the data with the same transition range as that in the TIPS-Pentacene. This data confirms that the coupling is at a molecular level as the Arrhenius behaviour is present irrespective of the morphology of the (Rubrene being amorphous in comparison to the poly-crystalline TIPS-Pentacene).

One issue that requires an explanation is the fact that there are only two energies. One would typically expect in the case of a vibrational coupling a single energy, as in the case of the model, or a multitude of energies given the organic molecules studied in this thesis have a vast vibrational spectra. There are some theories that attempt to explain this. One is that the interaction may be enhanced by a symmetry breaking process such as that involved in the SO coupling mechanism and that only some of the vibrational modes possess the relevant symmetry breaking. This does give an explanation for the selection of specific modes, but on the other hand the molecules have two different chemical structures and the vibrational modes present

would be expected to differ some what between the two molecules. This is not the case and in the data there appear to be two energies irrespective of the chemical structure. This means that symmetry breaking alone is not sufficient to explain only having two energies. Another mechanism could be one related to a geometric phase, analogous to a Berry phase, with only a few vibrational modes sweeping out a finite solid angle in one period. Although this mechanism offers a selection rule to explain the few contributing modes, for much the same reasons as above it does not explain why there are only two in all the molecules. There is an alternative suggestion that the mechanism is related to Bose-Einstein statistics with the addition of absorption and emission processes which is covered in detail in reference [212] but this still does not give a definitive answer to why there are only two modes.

However, one possible conclusion that is able to solve most of the problems mentioned above is that the energies extracted are in fact an average of a group of energies that cannot be resolved within the experimental limits of the MuSR. At the higher temperatures the molecules vibrate with more degrees of freedom so the average energy lies in the higher frequency vibrations. As the temperature is decreased there is an apparent transition point in which the higher frequency vibrations are not present or as dominant so the average energy shifts to the lower frequencies that do not have as many degrees of freedom. The higher temperature vibrations involve large flexing, distortion and stretching motions in comparison to the simple more constrained motion in the lower temperature vibrations. This is irrespective of the model applied and would explain why there exists only two energies for all the molecules despite the chemical structure.

9.2 Quinolate Series

In order to investigate the idea of this vibrational coupling further the same temperature dependance was carried out in the Quinolate series. Figure 9.2a shows the temperature dependence for AlQ_3 , the first in the Quinolate series. The eSR is plotted on the same logarithmic against inverse Temperature scale in order to give a direct comparison to the data reported earlier for the functionalised acenes. The first point to note is that the Arrhenius behaviour is still present despite the completely different chemical structure to that of TIPS-Pentacene and Rubrene. This would suggest that the vibrational coupling is general to small organic molecules which is not too surprising given the general nature of the eSR itself. The different chemical structure does produce some alterations in the data when it comes to the high and low energy regions. There are still two distinct regions but the transition range appears to be shifted to a significantly higher temperatures, in the region of 150 K to 200 K. The shift in this transition would imply that the eSR is coupling to a different set of vibrational modes where the energy required to populate the higher

frequency modes is distinctively greater than in the TIPS-Pentacene and Rubrene.

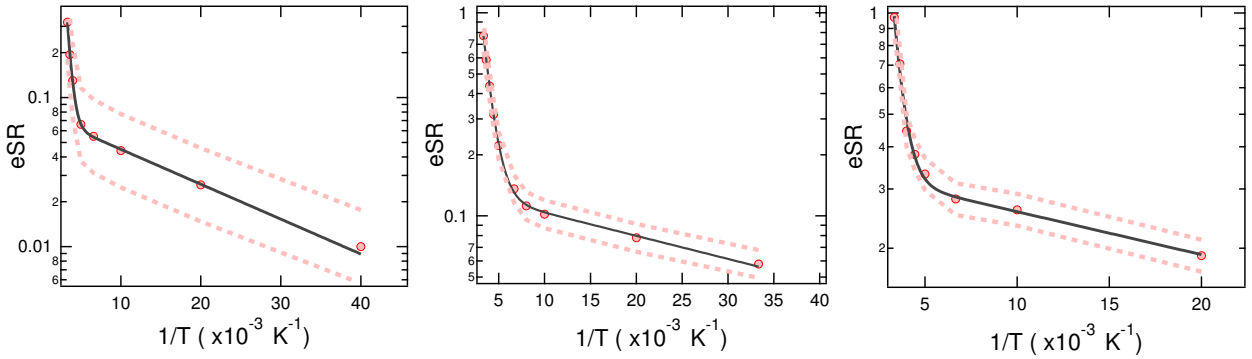

(a) Temperature dependance of the eSR in AlQ_3 with confidence intervals. Solid black line show the double Arrhenius fit result

(b) Temperature dependance of the eSR in GaQ_3 with confidence intervals. Solid black line show the double Arrhenius fit result

(c) Temperature dependance of the eSR in InQ_3 with confidence intervals. Solid black line show the double Arrhenius fit result

Figure 9.2: Temperature dependence of the eSR in the Quinolate series

In addition to the AlQ_3 the temperature dependance was carried out in GaQ_3 and InQ_3 to determine if the Z-number was having a significant effect on the vibrational coupling. The data for these molecules is also plotted in Figure 9.2. Initially there appears to no effect from the slight change to the crystal structure as the transition temperature region is consistent throughout the series i.e. there there appears to be no appreciable difference in the energy required to populate the higher frequency modes. The Z-dependance is also consistent with the temperature data as can be seen from figure 9.3. Interestingly the gradient of the power law appears to undergo a significant and sharp change at the temperature range corresponding to that of the transition in the eSR temperature data.

The next logical step was to compare the measured energies of both the regions in the AlQ_3 to the vibrational spectra to ascertain if the values were comparable to the vibrational modes present in the molecule. The data was fitted in the same manor as the TIPS-Pentacene and Rubrene in which the two component Arrhenius function in Equation 9.1 was used. As before the contribution of each component is embedded in the pre-factors and the fits can be seen in Figure 9.2a. In this case the fits are presented as one function with both components.

The energies extracted were 179.8 meV and 4.6 meV (1450.3 cm^{-1} and 37.4 cm^{-1}) for the high and low energy regions respectively. These values when compared to the vibrational spectra published by Halls and Aroca [213] correspond to two main types of vibrations. The lower energy value lies in the range of the low frequency torsional vibrations of the ligands in the AlQ_3 , where as the higher energy value lies in the range of the less restrained distortion/stretching modes of the rings in the ligands. Both of these modes can be seen in files 'High_Energy_ALQ_mode' and 'Low_Energy_ALQ_mode' in the digital appendix. These modes require a more

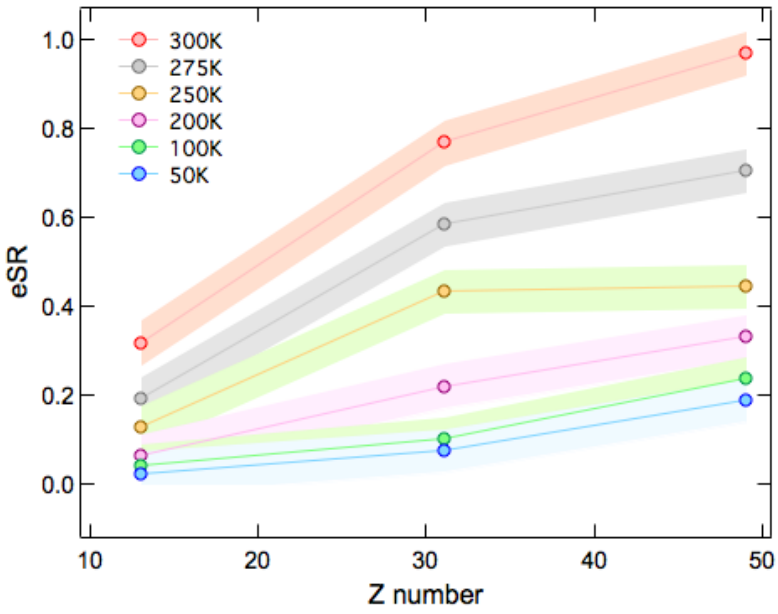

Figure 9.3: Z-number dependence of the eSR at various temperatures shown with confidence intervals

substantial amount of energy to overcome the constraints from the crystal packing and ligand overlap which may point towards the cause for a higher transition temperature in these molecules.

To compare the effect of an increasing Z-number the data for the GaQ_3 and InQ_3 were also fitted with the same function and the energies extracted for both regions in each molecule. These can be seen plotted in figure 9.4. It is obvious from the data that within the limits of the experimental error there is no change in the energy with increasing Z-number in both the high and low temperature regions. This result is not unexpected given the comparison with the vibrational modes. As previously mentioned the muonium is attracted to the positions on the molecule with an unpaired spin and consequently the highest electron spin density which in the case of the AlQ_3 is on the ligands [208] and therefore would be sensitive to any vibrational modes that involve the ligand. In the AlQ_3 this was the case as both the torsion and distortion/stretching were to the rings in the ligands of the molecule and any effect on the frequencies from the heavier central ions would be expected to be very small. Indeed the size of this change in frequency if present is clearly less then the experimental error on the data confirming that the major effects in the temperature dependance results are arising from the vibrational modes on the ligands and not the central ion in all three quinolates.

These temperature studies have shown that the SO interaction determined to be the dominant mechanism in the Z-number studies is a mediator for a molecular coupling between the eSR and the population of the vibrational modes. It is clear that the coupling is facilitated by a more direct coupling of the spin to the vibrations although the exact nature of the coupling is uncertain. Several models have been

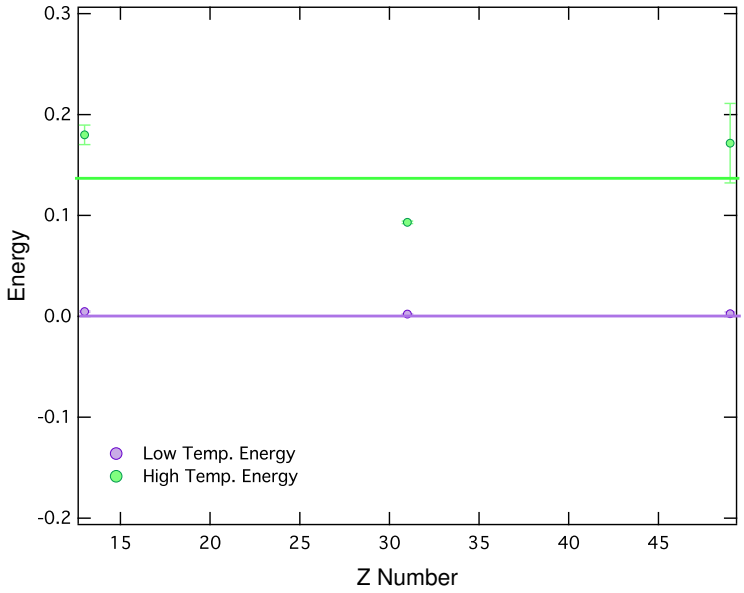

Figure 9.4: Z-dependance of the energies in the Quinolate series

proposed and in this section the model by Rybicki was touched upon to explain the Arrhenius behaviour. It is important to try and understand if, or how much, the curvature of the molecule plays a role in this coupling of the spin and it is this reason that leads to the final part of the work presented in this thesis.

9.3 Curvature and Enhanced SO in the Quinolate Series

In the spin relaxation section the model of Fratini et al. was discussed. The model involved the absorption and emission of phonons through a coupling of the spin to the vibrations. This arose from the local curvature of the bending modes in the molecule and acted to enhance the SO interaction. The bending modes were taken from Pentacene and can be seen in Figure 9.5. Similar bending modes are expected in the other small molecules presented in this thesis which makes this mode very relevant to the data reported. In their work they have derived an expression for the temperature dependance in particular in the context of the MuSR technique. Naturally this model provides the tools to test the role of the curvature and consequently the idea of an enhanced SO interaction in the small organic molecules. This section aims to use the model to analyse the temperature data for the Quinolate series and to establish through the fitting of the data a comparison to the analysis presented in the previous section. The model is still in developmental stages, but it is useful to obtain whether the coupling to the curvature needs to be considered in these molecules.

The relation between the eSR and the temperature reported by Fratini et al. takes the form of an inverse hyperbolic tan function. The frequency of the coupled vi-

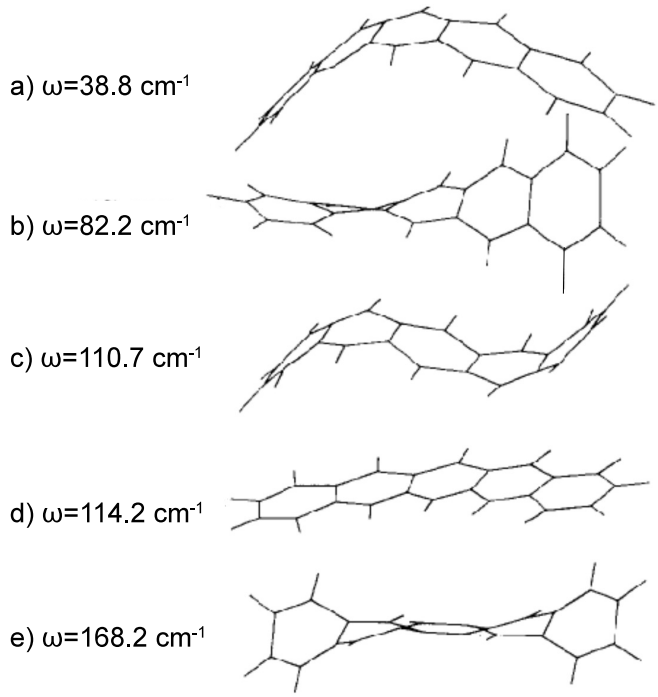

Figure 9.5: The lowest five frequency bending modes in Pentacene used in the model by Fatini et al.

bration determines the shape of this hyperbolic tan function and an energy can be extracted which can be compared to the other data. The function can be seen in equation 9.2 and is derived purely from the bending modes/curvature in Pentacene described earlier.

$$\mathrm{eSR} = A + \frac{B}{\tanh \frac{\hbar\omega}{2K_B T}} \tag{9.2}$$

The significance of the constant A in the equation is that instead of the both the absorption and emission of phonons occurring in the system there is in fact only one process taking place stemming from the 1+2n instead of simply 2n in the derivation, most probable is the absorption of phonons. The pre-factors including the spin orbit coupling strength, the LUMO matrix elements and the energy difference between the two states involved in the spin flip process are all constant and hence can be amalgamated in to the two constants A and B.

Figure 9.6 shows the eSR plotted on a linear scale against the temperature for all three quinolates. The data are fitted with the function above and the results of the fits can also be seen as solid lines in figure 9.6. It is clear that the single component tanh function does not describe the data as well as the double Arrhenius function presented earlier. In particular there is poor fitting in the lower temperature with the function producing a straight line where as the data appears to have a gentle slope. It is worth noting at this point that the absolute values of the parameters A

and B are the same however the value for A is negative. This confirms the notion that only one absorption/emission process is occurring in these molecules.

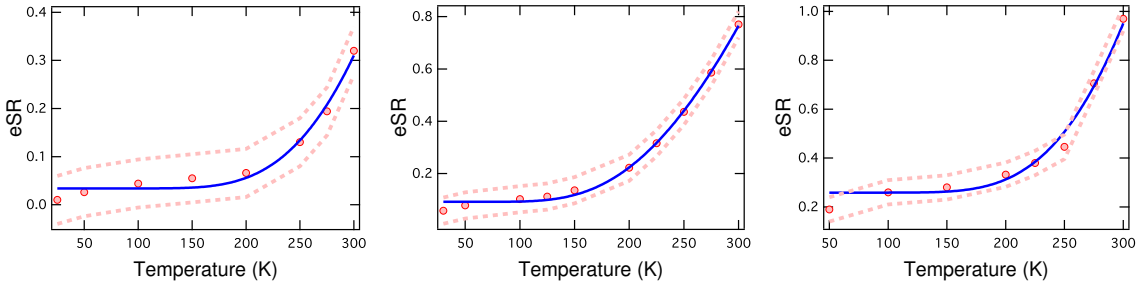

(a) Temperature dependence of the eSR in AlQ_3 plotted on a linear axis with confidence intervals. Solid blue line shows single component fit

(b) Temperature dependence of the eSR in GaQ_3 plotted on a linear axis with confidence intervals. Solid blue line shows single component fit

(c) Temperature dependence of the eSR in InQ_3 plotted on a linear axis with confidence intervals. Solid blue line shows single component fit

Figure 9.6: Single component hyperbolic tanh function fits to temperature data

Initially these results would imply that the model needs to be altered to incorporate the behaviour of the eSR at lower temperatures. However, if the data is considered to have two regions at high and low temperatures as in the previous analysis then it is logical to conclude that there is a coupling to more than one frequency and hence the fit may require a second component. In order to test this a second component was incorporated in to the function as before via a simple addition of the two components. The data were then fitted with the new function (equation 9.3) and the results of these fits can be seen with the data in figure 9.7.

$$\mathrm{eSR} = A + \frac{B}{\tanh \frac{\hbar\omega_1}{2K_BT}} + \frac{C}{\tanh \frac{\hbar\omega_2}{2K_BT}} \tag{9.3}$$

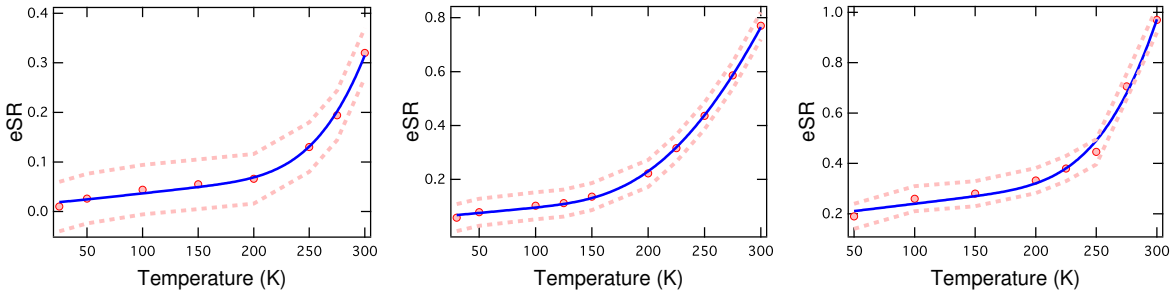

(a) Temperature dependence of the eSR in AlQ_3 plotted on a linear axis with confidence intervals. Solid blue line shows double component fit

(b) Temperature dependence of the eSR in GaQ_3 plotted on a linear axis with confidence intervals. Solid blue line shows double component fit

(c) Temperature dependence of the eSR in InQ_3 plotted on a linear axis with confidence intervals. Solid blue line shows double component fit

Figure 9.7: Double component hyperbolic tanh function fits to temperature data

This function allows for the fitting of the eSR at lower temperature as is in much greater agreement with the data. There are now two frequencies that can be extracted from the fits and what is most interesting is that the values of these frequencies are the same as those extracted from the Arrhenius fitting. This firstly suggests that the models are in agreement with one another and that there are definitely two energies in the data. It also implies that the process responsible for the coupling of the spin to the vibrations may well be dependant on the curvature of the vibrational modes in the molecule giving an enhanced SO interaction.

These are promising results and highlight the need for the enhanced SO interaction from the coupling to vibrations to be considered in the future models to describe the eSR in small organic molecules. However it is also clear that further development and understanding of this model is needed to fully analyse the mechanisms behind the eSR.

Chapter 10

Summary

With technology rapidly advancing in the field of organic electronics the spin degree of freedom is the next highly sought after advancement. It s therefore to no surprise that spintronics has become a hot topic in the scientific community. In particular understanding the mechanisms that influence the spin transport and spin relaxation have become of great interest. This thesis has presented the theories and models currently being proposed in particular those related to the SO and HFI and has portrayed the debate that continues in the community as to the dominant mechanism behind spin relaxation.

The results presented have shown that there is an electron spin relaxation on an intramolecular level which exists in small organic molecular semiconductors and that this spin relaxation can be probed using the MuSR technique. The measurements have provided a wealth of strong evidence to support the SO coupling as the dominant mechanism behind spin relaxation contradicting the long held belief that it is the HFI. Deuteration of the functionalised Acene TIPS-Pentacene has shown that changing the magnetic moment does not appear to have any effect on the spin relaxation which supports the SO interaction not the HFI. This result combined with the Z-dependence study of two separate series of molecules has gone as far as ruling out any direct or indirect HFI at the molecular level.

The existence of a spin vibrational coupling has also arisen from the work in this thesis and there is a need to understand the nature of this coupling. Evidence is being presented that suggest the coupling may be the result of an enhanced SO interaction through the curvature of the molecule and indeed one such model and its relevance to the MuSR studies have been reported in this thesis. The model does not use the commonly adopted conventional band theory which makes the other models contentious but instead is derived directly from the bending modes such as those present in Pentacene. The application of this model does offer a lot of promise for the future and may certainly be useful in understanding the role of curvature in spin relaxation. The temperature dependance studies of the eSR carried out in this

thesis have shown that in future focus needs to be turned to the vibrational modes in organic semiconductors as they hold the key to understanding the mechanisms behind the spin relaxation.

One of the major drawbacks that was highlighted from the work presented here was the need for stronger, more accurate computational methods in particular that are suitable for the solid state. Currently the main methods are semi-emperical and DFT calculations and it was the DFT calculations specifically that were brought in to question. The variation in the results was made quite obvious between the calculations performed by McKenzie and Pratt with the assumptions of McKenzie being fundamentally wrong and missing conformations. This makes it difficult to mesh the theoretical predictions with the experimental results. However, the calculations by Pratt did show that the results from DFT can be improved and further development should be carried with the aid of experimental for comparison.

In order to continue the work in this thesis further experiments have been proposed in the form of variation of the location of the substituted atoms in the Z-dependance work in addition to further temperature studies in TIPS-Petacene. Some of these have been started and are already proving useful in developing a greater understanding of the eSR and its coupling to the vibrations in the molecules as well as how an enhanced SO interaction plays a part. Analysis of these results is ongoing but in combination with the previous results one thing is clear. In order to fully utelise the spin degree of freedom the spin relaxation needs to be fully realised and its appears that there is an important interaction between the vibrational modes and the spin relaxation whose nature needs to be understood to pogress.

Chapter 11

Work in Progress

11.1 Z-Dependance of the Core V's the Ligand

11.1.1 X-substituted Quinolate Series (X-AlQ3 series)

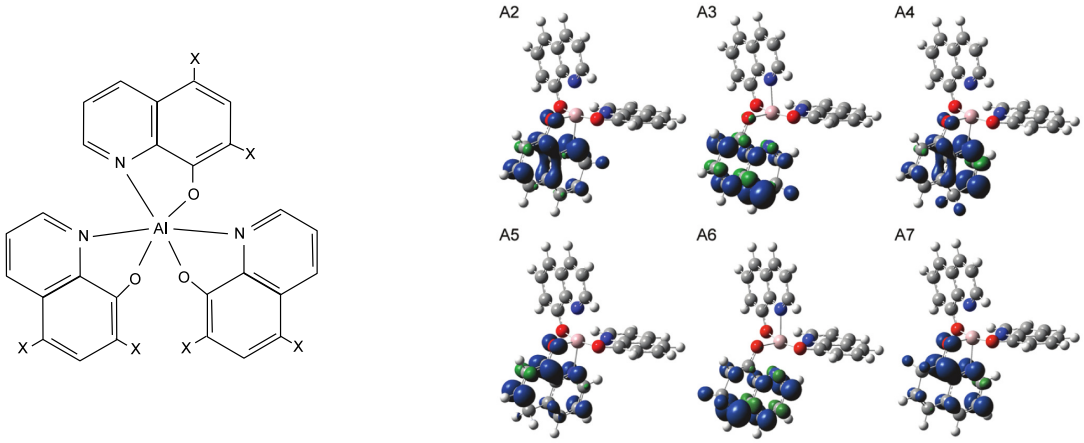

(a) Structure of the X-AlQ3 series

(b) Electron density on AlQ3 for various muon adduct positions [208]

Figure 11.1

The Quinolate series has been studied in depth in this report and the Z-dependance of the eSR has been extracted, however, the Quinolate molecules consist of two parts to their structure. There is the central metal ion or cation and the three side groups or ligands attached to the central ion. In the case of the Quinolate series the alteration is to the central metal ion which is only changing one part of the structure. The next logical step would be to change the ligand part of the structure to make a comparison between the two. This may also help to establish a better understanding of how the eSR and hence Z-depndance is related to the electron density across the molecule. A series involving the substitution of two Hydrogens, in each of the AlQ3 ligands, with Br, Cl and I has recently been synthesised. The structure of this

substituted series can be seen in figure 11.1a. In the case of the Quinolate molecules the electron density is distributed only on the hydroxyquinoline ligands and not on the central ion. An example of this distribution is shown in figure 11.1b for various muon adduct possibilities as determined by McKenzie et al. [208]. This means by substituting the Hydrogen in the ligand of the molecule instead of the central ion the substituted atom will be located directly where the electron distribution resides. Therefore the change in Z will directly effect the eSR that the muon measures and result in a much more significant change. In addition the substituted atoms are much more electronegative then the Hydrogen so may well change the dependance even further. It is worth noting that the shape of the ALC resonance is expected to be different to the spectra reported for the Quinolate series as the muon adduct positions and their probabilities are changing.

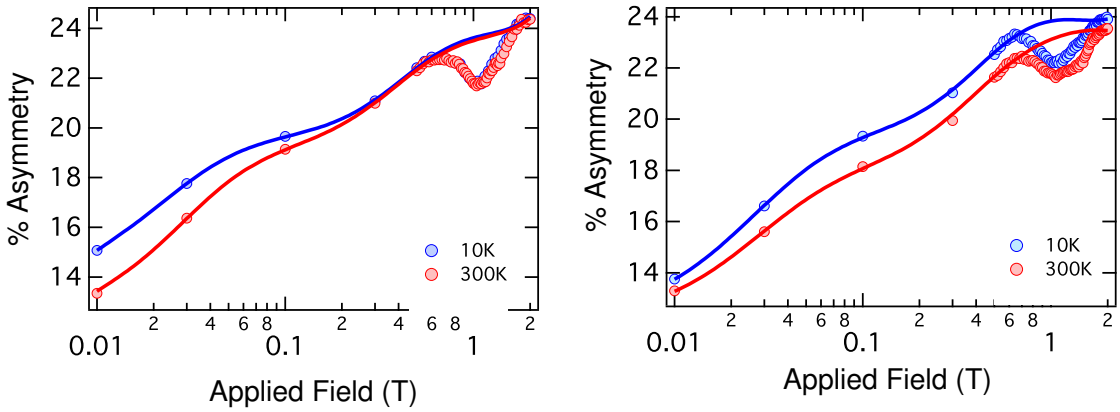

(a) Fitted repolarisation curves for Chlorine substituted AlQ_3 at 10 K and 300 K

(b) Fitted repolarisation curves for Bromine substituted AlQ_3 at 10 K and 300 K

Figure 11.2: Fitted repolarisation curves

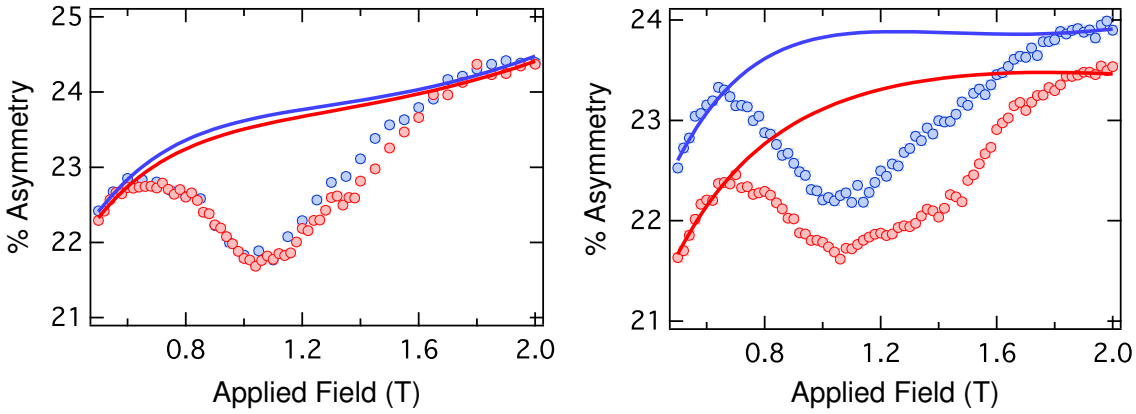

(a) Fit from Figure 11.2a focused in around the resonance

(b) Fit from Figure 11.2b focused in around the resonance

Figure 11.3: Repolarisation fits around the resonance in the X-substituted AlQ_3 series

The data at 10 K and 300 K has been measured on he HIFI spectrometer for the

Chlorine and Iodine substituted X-Quinolate series. The time integrated data was fitted using a combination of an isotropic repolarisation, a full anisotropic repolarisation and a shifted $3^r d$ order polynomial to extract the ALCs. These fits are presented in FIgures 11.2 and 11.3 where it is clear to see that these ALCs are situated on the end of the repolarisation curve and hence a polynomial function alone is not sufficient to extract the ALC. Figure 11.4 shows the resultant ALCs at 10 K and 300 K after the background subtraction. What is immediately clear is that there does not appear to be a temperature dependence of the ALC in either of the two cases. This is completely the opposite to the data presented earlier in the thesis and the only change appears to be a shift in the HFCs.

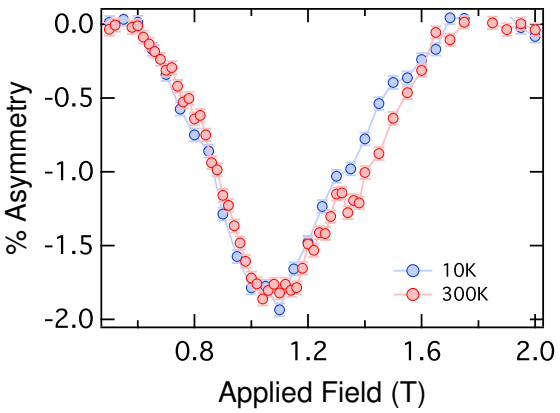

(a) Extracted ALC resonance at 10 K and 300 K in Chlorine substituted AlQ_3

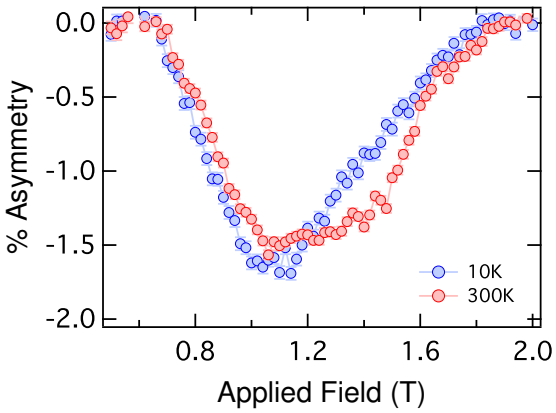

(b) Extracted ALC resonance at 10 K and 300 K in Bromine substituted AlQ_3

Figure 11.4: ALC resonances in the X-substituted AlQ_3 molecules after background removal

Initially this data appears contradictory to the results obtained earlier for the other small molecules. However, it may be explained by the fact that the additional substituted atom is now located directly on the ligand with the muon rather than in the central ion position. In the case of the X-substituted AlQ_3 the the SO interaction behind the eSR is evolving from two sources such that the $\mathbf{SO}_{\text{eSR}} = \mathbf{SO}_{\text{CI}} + \mathbf{SO}_{\text{X}}$ where $\mathbf{SO}_{\text{CI}}$ is the SO due to the central ion and $\mathbf{SO}_{\text{X}}$ is the SO due to the X-substituted atom. Nominally the $\mathbf{SO}_{\text{X}}$ is zero in AlQ_3 so $\mathbf{SO}_{\text{CI}}$ is the dominant source of the SO interaction. This leads to a change in the eSR of approximately a few MHz. However in the case of the X-substituted AlQ_3 the $\mathbf{SO}_{\text{X}}$ is present and is much stronger due to the direct overlap of the orbitals of the substituted atom and the electron compared to that resulting from the bending modes in standard AlQ_3 . As a result of the size of the $\mathbf{SO}_{\text{X}}$ the $\mathbf{SO}_{\text{CI}}$ is now a perturbation and hence any change from the bending of the molecules does not have a significant effect on the overall SO interaction.

This would cause a dramatic difference in the temperature dependence as the eSR would be a lot stronger, in the region of 10s - 100s of MHZ. When this is modelled in

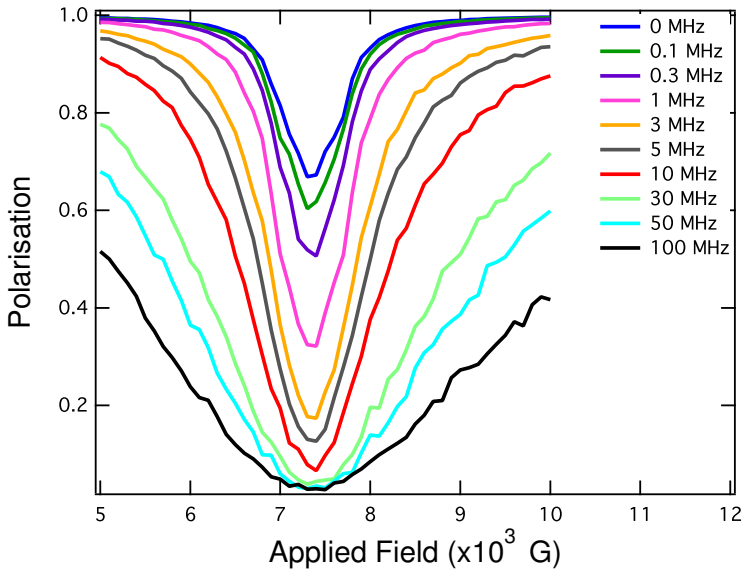

Figure 11.5: Modelling of a typical resonance to show the extremes of the shape and amplitude changes with eSR

the quantum software it becomes clear as to how the temperature dependence would not be present. This can be seen in Figure 11.5 In the region of zero to a few MHz the change of amplitude is quite significant. So, in the nominal case there is a change of eSR from the vibrational coupling in the order of 1 Hz from what was 0.02 MHz and hence falls in to this lower eSR regime. On the other hand when the eSR is in the tens to hundreds of MHz range the amplitude of the ALC does not change significantly with reasonable changes in eSR but instead just broadens. Therefore in the case of the X-substituted molecules the 1 MHz becomes a perturbation on the already large eSR from the direct SO interaction. This is evident in the modelling where a change of 10% above 10 MHz has no real effect as to change the width of the ALC slightly. So one would be able to conclude that given this explanation the temperature dependence would be masked by the much greater $\mathbf{SO}_{\mathrm{X}}$ interaction.

11.1.2 TMX-ADT Series

The comparison between the substitution of the central ion in the Quinolate series and the ligand in the X-substituted Quinolate series discussed above is not the only possibility to compare the core of the molecule to the ligand, there is also the TES series reported earlier. The same approach could be taken for the TES series as in the Quinolate series. The atoms on the ligands can be substituted instead of those on the backbone. Recently a series of molecules called the TMX-ADT series have been synthesised. In this series the Carbon in the ligand is substituted for Silicon and Germanium. The structure of the series along with an idea of the orbital distribution can be seen in Figure 11.6. The backbone is the same as that in TES-ADT whereas the ligand is the same as that in the TMS-Pentacene described in Chapter XX.

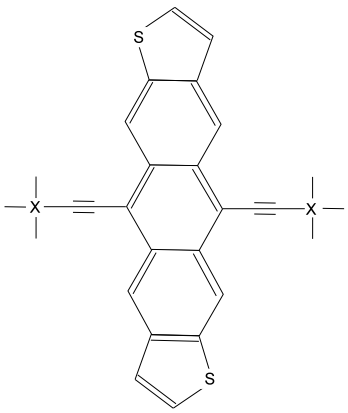

(a) Structure of the TMX-ADT series

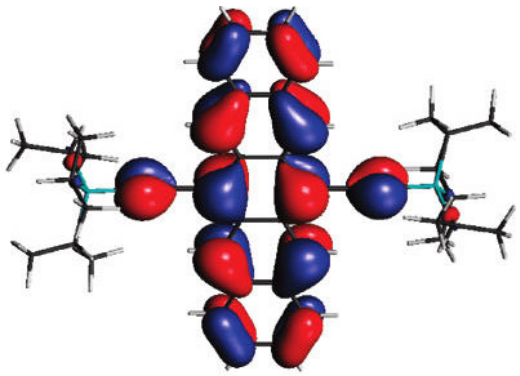

(b) HOMO in TIPS-Pentacene [135]

Figure 11.6

The interesting feature about the TMX-ADT series is that the substituted atom is on the ligand and is much closer to the triple bond where the muon is located. Consequently on would expect the SO to have a much different Z-dependence. To study this very recent measurements have been carried out on the ALC spectrometer at PSI.

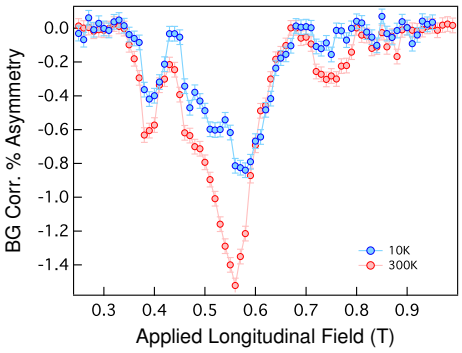

(a) ALC spectra for TMS-ADT at 10 K and 300 K

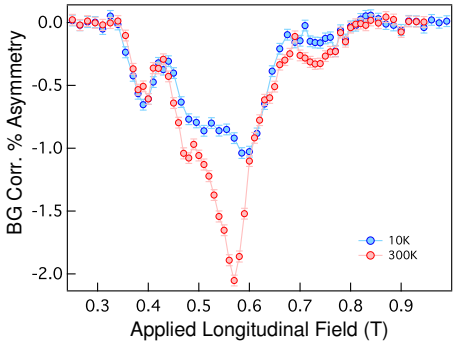

(b) ALC spectra for TBU-ADT at 10 K and 300 K

Figure 11.7: ALC spectra at 10 K and 300 K for TMS-ADT and TBU-ADT

Figure 11.7 shows the time integrated data at 10 K and 300 K around the resonances extracted from the raw data. The raw data was fitted locally with a third order polynomial to extract the ALCs. The temperature dependent amplitude is still present in the series which implies the eSR is still present and that it is still dominated by the coupling to the vibrations in the system. One feature that can be observed is the similarity of the TMS-ADT ALC to the of TES-ADT. The increase in the amplitude is in the order of 100% in both and therefore it would be reasonable to assume that the increase of the eSR is of the same order in the TMS-ADT as in the TES-ADT. This data also confirms that the methyl groups in the functionalised acenes do not play a significant role in the eSR as this is the only difference between the TMS-ADT and the TES-ADT. This is far from surprising as the electron spin

density resides on the main backbone of the molecule so the strongest effects would be observed from the bending modes in the spine. This is consistent with the data earlier in which the vibrations involving the backbone and triple bond were the ones causing most effect in the eSR. This could go towards explaining the very weak Z-dependance in this series as the substituted atom is removed from the electron spin density and so does not cause a significant effect.

11.2 Additional DFT and Temperature Studies

11.2.1 DFT

One point highlighted in the studies reported in this thesis is the need for improved computational methods to analyse the data. Improved DFT calculations would provide a useful tool in not only determining experimentally where to measure to obtain the resonances but also in the modelling of the spectra. Currently the modelling is carried out by assessing the data and determining "by hand" the positions and widths of the ALCs. These are then compared to any DFT results. Although the modelling procedure is consistent and does provide reliable results it would be far more efficient and accurate if the correct DFT calculations were readily available in order to simply run a fit routine for the data. Thus far the DFT calculations by McKenzie in the solid state have proved unreliable and inaccurate by factors of up to 40%. Despite this, very recent calculations by Pratt have proven fruitful in helping to understand the the data in the Quinolate series and providing reliable comparisons to the modelling parameters to within 5%.

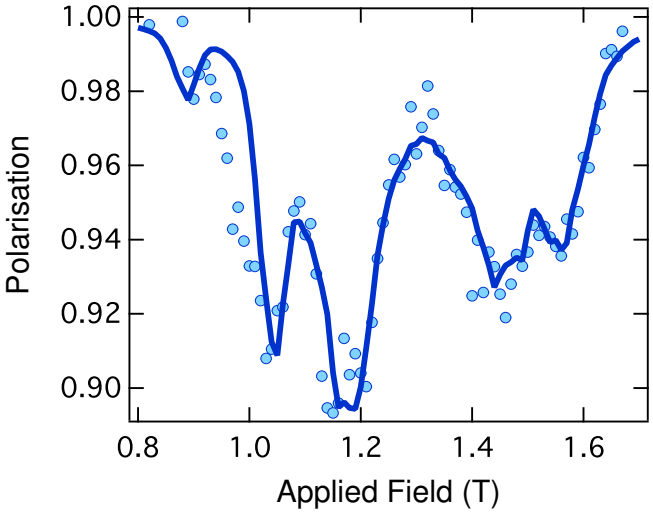

Figure 11.8: 10 K ALC spectra for AlQ_3 with scaled data from DFT calculation (solid blue line)

As was discussed earlier Pratt uses a combination of an unrestricted Hartree-Fock

PM3 calculation to optimise then feeds the structure in to the DFT calculation to obtain the electron spin distribution. From this Pratt is able to provide accurate HFC constants an in addition useful dipolar terms to model the data with. In fact a very rough and initial attempt has been made by the author to model the 10 K AlQ_3 data directly from the results of Pratt's DFT calculations, only altering the scaling factors to reflect the adduct formation probabilities. The results of this can be seen in Figure 11.8 and although the result is quite rough it is immediately clear that with some refinement the data could quite easily be modelled from the DFT values. This also would strongly suggest that the DFT calculations from the functionalised acene work need to be reviewed and recalculated using the method of Pratt not McKenzie. This in turn could be followed by the remodelling of the data directly from the DFT values.

11.2.2 Temperature

One other main conclusion that has emerged from this thesis is the presence of a vibrational coupling that may well be influenced by the curvature of the molecule. The nature of this coupling is still uncertain, however, the difference in the muon adduct positions may provide a source of further understanding. It was shown in Section XX that there are the two groups seen below (Figure 11.9) in TIPS-Pentacene. It was also shown that the sites in group 1 involved or were situated very close to the triple bond. On the other hand the sites in group 2 were shown to be on the end of the backbone.

One would expect the two different sets of sites to be influenced in different ways by the vibrations of the molecules and hence couple to different modes. If this were the case then the energy scales would be altered between the two sets of adduct sites. As yet the temperature dependence has not been studied in group 2 of TIPS-Pentacene. However, this would prove useful to extract the energies of the vibrations that couple to the eSR in these sites given the previous temperature dependence studies conducted in TIPS-Pentacene. It is also already evident that there is a difference as the percentage increase at 300 K is lower in the group 2 compared to that in group 1 indicating a change in the size of the eSR between the two groups. This study could be carried out in future work to try and understand the vibrational coupling further.

In addition to the muon measurements there is also the need for further spectroscopic measurements to be made to fully interpret the temperature dependent data in TIPS-Pentacene. In the results reported in the earlier chapters the vibrational spectra in TIPS-Pentacene was calculated for a structure optimised from the base molecule without the knowledge of the exact crystal structure available. In order to obtain this information it would be necessary to perform x-ray diffraction mea-

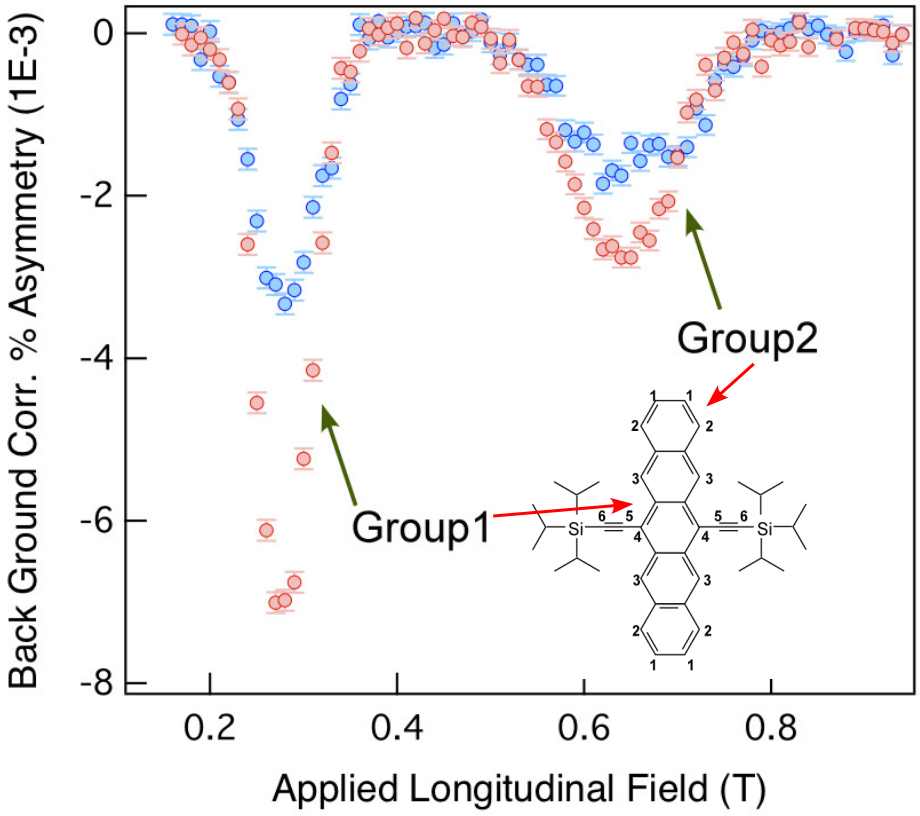

Figure 11.9: Lower field ALCs in TIPS-Pentacene at 10 K and 300 K with their coresponding site allocations (inset)

surements on a single crystal of TIPS-Pentacene to obtain a full refinement of the structure. Also measurements are needed of the vibrational spectra to compare to the calculated values in order to assign the vibrational modes present in the data. These measurements already exist in the case of the Quinolates where it was demonstrated that a direct comparison can be made between the muon data and the vibrational spectra. However, to the best of the authors knowledge these measurements have not yet been conducted in TIPS Pentacene but would allow for a much more accurate comparison of the effects from the vibrational coupling on the eSR. These could be performed along with the DFT calculations to gain a complete study of TIPS-Pentacene.

11.3 Electron Spin Relaxation V's Electronic Transport in P3HT

So far the eSR has been studied on a scale local to the molecule and the effects have been due to vibrations concerned with that molecule. However, it may be possible to use the eSR and the ALC-MuSR technique to study the effect of a transition of a hopping transport to band transport. Recent experiments along

with DFT calculations have shown the presence of eSR similar to that reported in small organic molecules in the P3HT-Regioregular (P3HT-RR) polymer and its heavier counterpart P3HS. The data also showed some unusual effects in the ALC amplitude not expected with the eSR. Therefore measurements were taken on P3HT-Regiorandom (P3HT-RRa) and two morphologies of P3HT-RR at high fields to establish the exact nature of the eSR in these polymers and to understand any additional effects with temperature.

The measurements were conducted on the HIFI spectrometer at ISIS using a CCR cryostat. The samples were mounted in 25 μm thick silver packets measuring 20mmX30mm and suspended in an Aluminium frame. The P3HT-RRa weighed 220mg and was red in colour. The first morphology of the P3HT-RR (sample A) was as purchased and weighed approximately 179mg. The second morphology of P3HT-RR (sample B) was re-crystallised from the purchased material in chloroform and weighed 370mg. Both the P3HT-RR samples were green in colour.

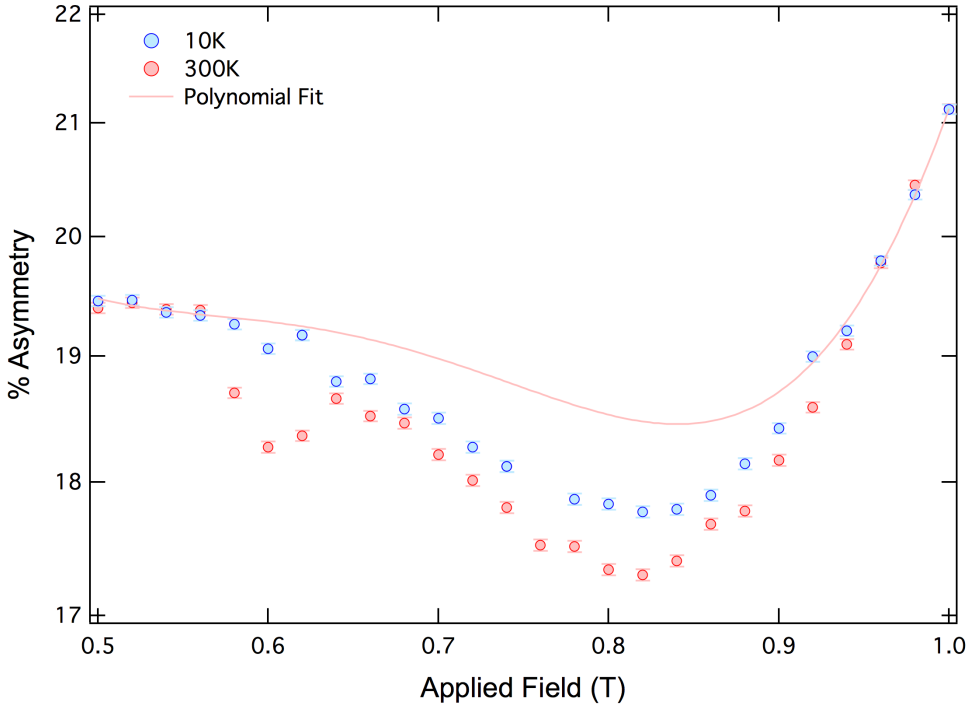

Figure 11.10: Fitted time-integrated data in P3HT-RRa. Solid line shows fourth order polynomial fit in the local region to the ALC

Figure 11.10 shows the time-integrated asymmetry around the resonance in P3HT-RRa. This data was fitted locally with a 3rd order polynomial to remove the background and the resultant fit can also be seen in Figure 11.10 as a solid line. It was possible to use the same background for both the 10 K and 300 K data as they clearly overlap in the fields off resonance. Figure 11.11 shows the final background subtracted ALCs at 10K and 300K. The ALCs are very broad which is expected given the disorder in the sample. It is also clear to see that the amplitude of the ALC has increased in the 300K spectra, which is consistent with the data reported

in this thesis for the small molecules. The magnitude of the increase of the broader, higher field peak with respect to 10 K is in the order of 80%. This increase can be attributed to the intra-molecular eSR, which was proven to occur in organic semiconductors.

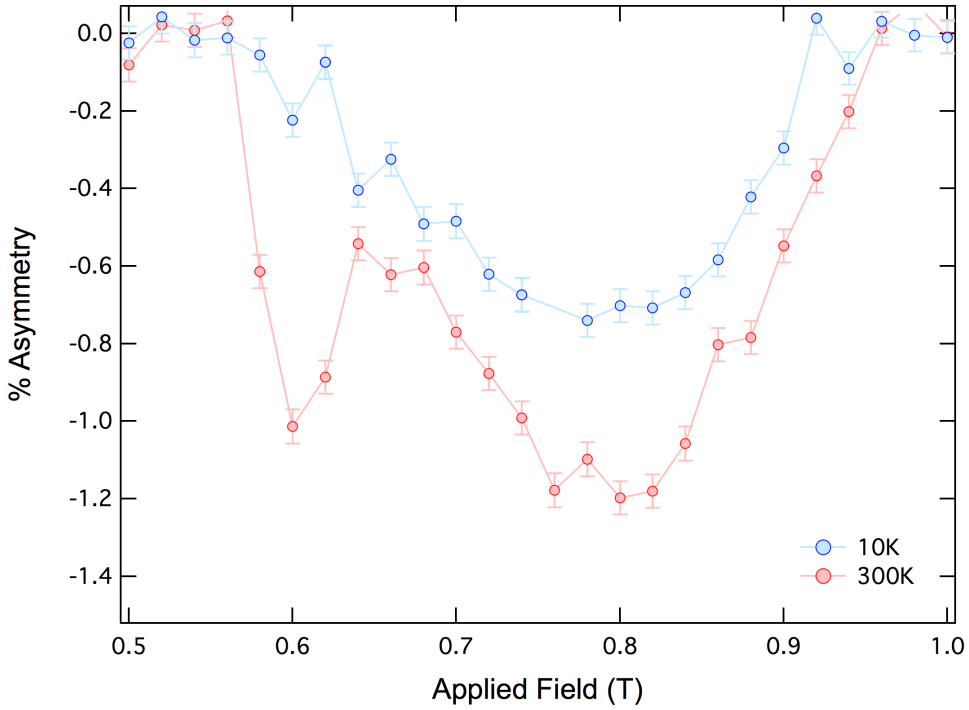

Figure 11.11: ALC spectra at 10 K and 300 K in P3HT-RRa

In order to gain a comparison P3HT-Regioregular was also measured. Field scans were performed for sample A at 10 K and 300 K in the same region as for the P3HT-RRa and in a similar manner the background was removed. The resultant spectra can be seen in Figure 11.12 along with the crystal structure (inset) of the polymer unit. The ALC at 300 K appears sharper then in the P3HT-RRa, which is to be expected with the more regular packing in this sample. The data is also consistent with measurements made previously on this sample on the HIFI spectrometer. However what is surprising both in the previous data and this data is the fact that the ALC at 10 K appears to have almost vanished. This is contrary to the expected behaviour for the eSR as the relaxation of the electron will enhance the spin depolarisation in the muon and hence will only increase the amplitude of the ALC. In this case the amplitude of the 10 K ALC is severely reduced which would suggest there is an additional effect present in the data.

One explanation is that the coupling between the muon and the electron is somehow being quenched which is possible if the system is becoming delocalised at the lower temperatures. This in turn could allow the initially bound electron to travel away from the muon and essentially vanish or alternatively another electron could be able to move freely in the delocalised state to occupy the energy level of the bound electron, which would cause the singularly occupied molecular orbital (SOMO) to

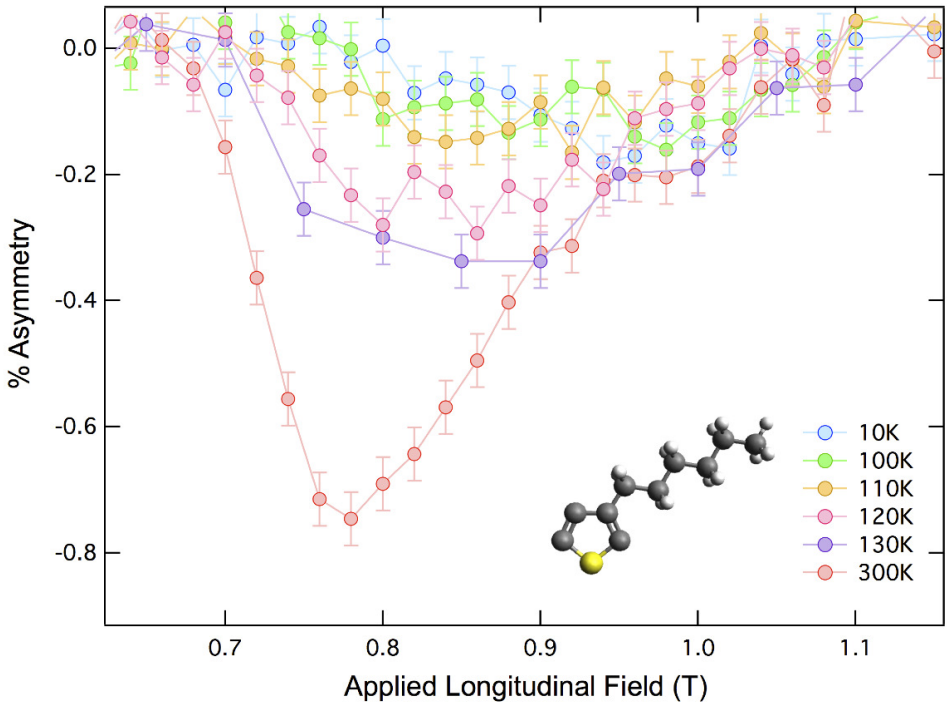

Figure 11.12: ALC spectra in P3HT-RR at multiple temperatures and inset the polymer unit cell of P3HT

become a doubly occupied molecular orbital (DOMO).

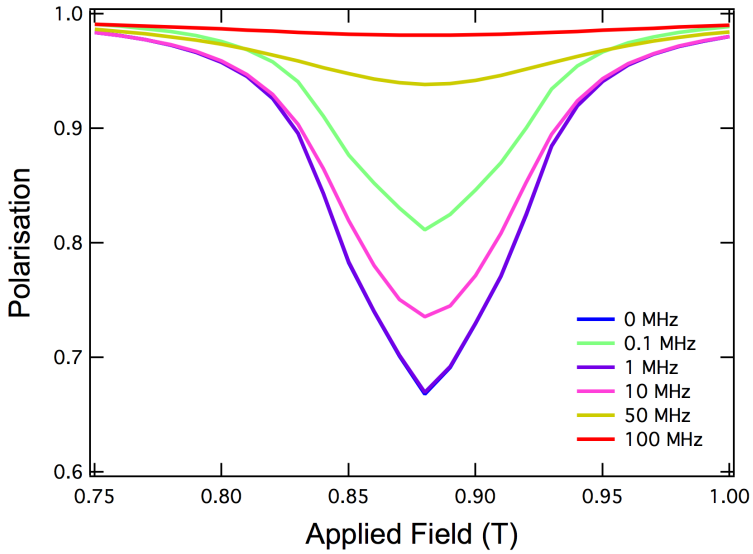

Figure 11.13: Modelling of an ALC with varying hopping rates in a two site system

In either case from the perspective of the muon the electron vanishes and therefore the resonance state would disappear also. To ascertain the effect of the electron moving away from the muon site a two-site model was used in Quantum software to simulate the ALC data for various hopping frequencies with no eSR. The results of this modelling are shown in Figure 11.13. There is a clear reduction in the amplitude of the ALC after an initial increase to 1 MHz as the hopping frequency (essentially the probability of the electron moving away) is increased. This supports the idea of

a delocalisation transport regime.

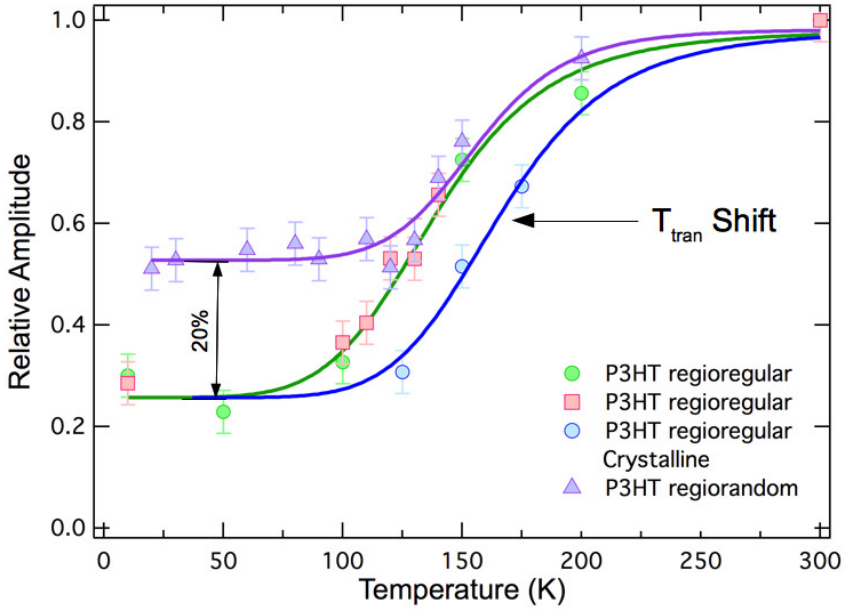

Figure 11.14: Normalised ALC amplitudes of P3HT-RRa (purple), P3HT-RR old measurements(green), P3HT-RR new measurements (red) and crystalline P3HT-RR (blue) as a function of temperature. Solid lines are to provide a guide to the eye

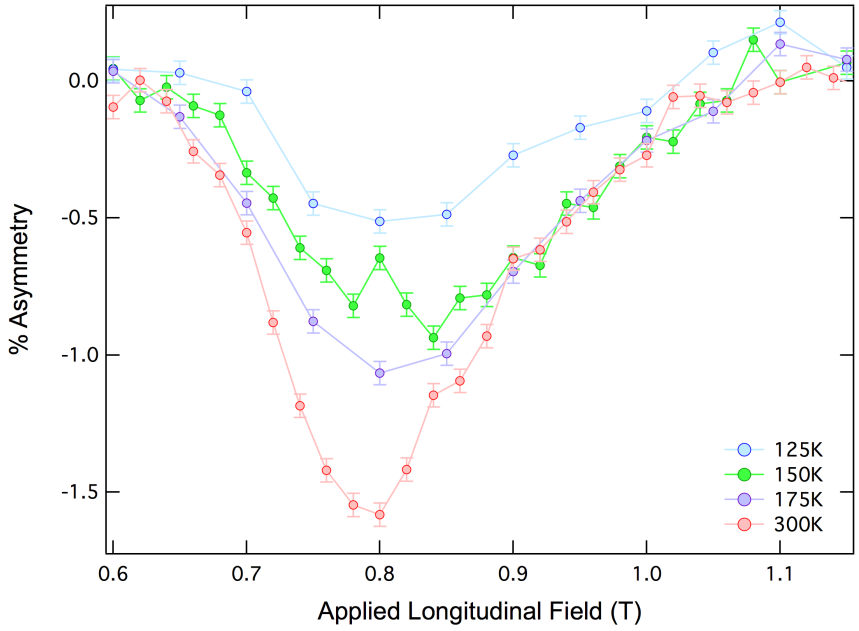

Figure 11.15: ALC spectra for P3HT-RR at various temperatures in the crystalline sample

An in-depth study of the temperature dependence was carried out for the P3HT-RR sample A. The subtracted ALCs can be seen in Figure 11.12 along with the 10 K and 300 K spectra. It is apparent from the data that there is a transition that occurs in the temperature region 130-200 K where the amplitude of the ALC starts to dramatically increase. The percentage change in amplitude with respect to

the amplitude at 300 K is plotted against temperature along with the temperature dependence in the P3HT-RRa sample and the previous data collected for the P3HT-RR in Figure11.14. The data shows that this effect is not dominant if at all present in the random morphology given the 20% difference in amplitudes between the P3HT-RR and P3HT-RRa at low temperatures. This could be possible if the diminished ALCs were a result of a transition to a delocalised electronic transport regime, as the P3HT-RRa has a much more disordered crystal packing making it much less likely for the electron wave-function to delocalise across the molecules. Therefore the eSR would still resemble that expected in a localised hopping regime. The study of the crystalline P3HT-RR sample B was also carried out. In this case the formation of delocalised bands would be expected to be easier as the sample has less defects to localise the wave-function and so any transition would be expected to occur at a higher temperature.

The result of the temperature dependant ALCs is plotted in figure 5 while the percentage change in amplitude is plotted with the other data in Figure11.14. It is evident that the amplitude is still diminished as in sample A implying any delocalised transport effect is still occurring but there is a clear shift in the transition temperature (in the order of 25 K) as expected. This data leads to the conclusion that in addition to the presence of the eSR there is a competing effect that could be evolving from the transition between a localised hopping transport to a delocalised band-like transport and that the effect can be probe using the eSR and ALC-MuSR technique. In the future the data will need to be modelled so that the exact values can be extracted but initially this proves the transport can influence the local measurements in these polymers.

Thank you to all

It is a great pleasure to thank the many people who have made this thesis possible.

First and for most I would like to express my deepest gratitudes to my two supervisors Dr Alan J. Drew and Dr William P. Gillin for without their help this work would not have been possible. Throughout my Ph.D they have provided great encouragement, sound advice and many opportunities to learn new things. In addition, they have shown vast amounts of patience and time to develop my scientific understanding and subject knowledge. I also thank them both for the fun, enjoyment and the many experiences I have had during my time as a Ph.D student. I have gained from them a new appreciation for beer and swiss fondue not to mention a valuable education in current affairs and the finer ingredients of ISIS canteen food :-). I especially would like to thank Alan for offering me the opportunity and encouraging me to work on such an engaging Ph.D project.

I have had the privilege of working with a wonderful group of friends and colleagues. For their unconditional support, kindness, valuable discussion and for keeping me sane I would like to thank: Leander Schulz, Laura Nuccio, Dr Pratik Desai, Nicola Rolfe, Kirsty Roy, Carlos Aristizabal, Calum McAndrew, Will Little, Filippo Boi, Sijie Zhang, Hongtao Zhang, Huanqing Ye, Shamim Khademi, Dima Bolmatov, Ali Karatutlu, Viswanathan Mohandoss and Eva Zarkadoula. In particular to Leander Schulz and Laura Nuccio who have taught me so much both as terrific friends and mentors and who have educated me in the German and Sicilian ways.

I would also like to thank the school and research staff who have supported me with their friendship, time and technical expertise. In particular Mr Geoff Gannaway, Mr George Neville, Ms Sarah Cowls and Miss Lucie Bone. They have all played a major role in making my Ph.D possible.

Of course I wish to thank the many collaborators and academics involved in my work: Prof Christian Bernhard, Dr Theo Kreouzis, Dr Simone Fratini, Prof Charles Stafford, Dr Ignacio Hernandez, Dr Rory Wilson, Prof John Anthony, Dr Martin Heeney, Dr Natalie Stingelin, Prof Martin Dove and I would also like to thank the EPSRC who have provided the funding my PhD.

One of the most fundamental parts of my Ph.D has been the many beamtimes in Oxford and Swizerland. For their help and academic discussion, I thank the staff at the Paul-Scherer Instutute: Dr Kamil Sedlak, Dr Christopher Baines, Dr Robert Scheuermann and Dr Andreas Suter.
ISIS facilities: Dr Francis Pratt, Dr Peter Baker, Dr Iain McKenzie, Dr James Lord, Dr Steven Cottrell, Dr Adrian Hillier and Emma Roberts for putting up with my supervisor.

My family have been there no matter what to support me during my Ph.D and to them I am indebted. In particular I would like to thank my brother and his wife who have always found the time to listen and guide me, but most importantly, I wish to thank my parents, Rosina Josephine Willis and Richard John Willis. They raised me, supported me, taught me, and loved me. To them I dedicate this thesis.

Bibliography

[1] Granström et al. *Nature*, 395(257), 1998.

[2] P. Peumans et al. *Nature*, 425(158), 2003.

[3] F. Yang et al. *Nature Materials*, 4(37), 2005.

[4] H. Sirringhaus et al. *Science*, 280(1741), 1998.

[5] M. Muccini. *Nature Materials*, 5(605), 2006.

[6] E. Cantatore et al. *IEEE Journal of Solid-State Circuits*, 42(84), 2007.

[7] K. Myny et al. *Organic Electronics*, 11(1176), 2010.

[8] Y. J. Chan et al. *IEEE International Workshop on Radio-Frequency Integration Technology, Proceedings*, (139), 2005.

[9] P. Ball. *Nature News*, 2004.

[10] G. H. Gelinck et al. *Nature Materials*, 3(106), 2004.

[11] J. Janata et al. *Journal of Solid state*, 13(41), 2009.

[12] U. Lange et al. *Analytica Chimica Acta*, 614(1), 2008.

[13] R. H. Friend et al. *Nature*, 397(121), 1999.

[14] J. Clarke et al. *Nature Photonics*, 4(438), 2010.

[15] V. A. Dediu et al. *Solid State Communications*, 122(181), 2006.

[16] Z. H. Xiong et al. *Nature*, 427(821), 2004.

[17] M. Schwörer et al. *Physik*, 7(5), 2008.

[18] G. Gustafsson et al. *Nature*, 357(477), 1992.

[19] S. R. Forrest. *Nature*, 428(911), 2004.

[20] Y. H. Kim et al. *IEEE Electron Device Letters*, 25(702), 2004.

[21] N. Stringelin-Stutzmann. *Nature Materials*, 7(171), 2008.

[22] N. Stringelin-Stutzmann et al. *Nature Materials*, 4(601), 2005.

[23] S. Pramanik et al. *Nature Nanotechnology*, 2(216), 2007.

[24] J. E. Anthony. *Angewandte Chemie International Edition*, 47(452), 2008.

[25] `http://www.almaden.ibm.com/spinaps/research/sd/?racetrack`.

[26] S. Bandyopadhyay. *Physical Review B*, 81(153202), 2010.

[27] P. A. Bobbert. *Nature Materials*, 9(288), 2010.

[28] V. A. Dediu et al. *Nature Materials*, 8(707), 2009.

[29] J. Rybicki et al. *Physical Review B*, 79(153202), 2009.

[30] S. Sanvito. *Nature Nanotechnology*, 2(204), 2007.

[31] `http://nobelprize.org/nobel_prizes/chemistry/laureates/2000/chemadv.pdf`.

[32] J. E. McGinniss et al. *Science*, 183(853), 1974.

[33] J. E. McGinniss et al. *Science*, 177(896), 1972.

[34] Photo taken by Peter H Proctor on 17 August 2006 and uploaded before donating the image to the Smithsonian institution Acc.#2003.0029.

[35] C. W. Tang and S. A. Vanslyke. *Applied Physics Letters*, 51(913), 1987.

[36] A. Bernanose et al. *Journal de Chimie Physique*, 50(64), 1953.

[37] A. Bernanose and P. Vouaux. *Journal de Chimie Physique*, 50(261), 1953.

[38] A. Bernanose. *Journal de Chimie Physique*, 52(396), 1955.

[39] A. Bernanose and P. Vouaux. *Journal de Chimie Physique*, 52(509), 1955.

[40] Y. Sato et al. *Journal of Selected Topics in Quantum Electronics*, 4(40), 1998.

[41] `http://www.ewh.ieee.org/soc/cpmt/presentations/cpmt0401a.pdf`.

[42] M. D. McGehee and M. A. Topinka. *Nature Materials*, 5(675), 2006.

[43] J. Nelson. *Current Opinion in Solid State and Materials Science*, 6(87), 2002.

[44] P. Peumans et al. *Journal of Applied Physics*, 93(3693), 2003.

[45] Y. Yamashita. *Science and Technology of Advanced Materials*, 10(024313), 2009.

[46] C. D. Dimitrakopoulos. *Advanced Materials*, 14(99), 2002.

[47] W. Brütting. *Physics of Organic Semiconductors*. Wiley 1st edition, 2005.

[48] A. Troisi. *Advanced Polymer Science*, 223(259), 2010.

[49] N. W. Ashcroft and D. Mermin. *Solid State Physics*. Holt, Reinhart and Winston, NewYork, 1976.

[50] G. D. Mahn. *Many Particle Physics*. 3rd Edition. Plenum, NewYork, 2000.

[51] C. Jacoboni and L. Reggiani. *Review of Modern Physics*, 55(645), 1983.

[52] A. Troisi and G. Orlandi. *Physical Review Letters*, 96(086601-1), 2006.

[53] R. Marcus. *Journal of Chemical Physics*, 24(979), 1956.

[54] J. Jortner. *Journal of Chemical Physics*, 64(4860), 1976.

[55] M. D. Newton. *Electron Transfer - From Isolated Molecules to Biomolecules*. pt 1, vol. 106, Wiley, NewYork, 1999.

[56] A. Nitzan. *Annual Review of Physical Chemistry*, 52(681), 2001.

[57] S. Fratini and S. Ciuchi. *Physical Review Letters*, 103(266601), 2009.

[58] Y. C. Cheng and R. J. Silbey. *Journal of Chemical Physics*, 128(114713), 2008.

[59] J. Loos et al. *Journal of Physics Condensed Matter*, 18(2453), 2006.

[60] P. E. Kornilovitch. *Journal of Physics Condensed Matter*, 19(255213), 2007.

[61] R. Feynmann. *Physical Review*, 97(660), 1955.

[62] W. Warta and N. Karl. *Physical Review B*, 32(1172), 1985.

[63] Y. C. Cheng et al. *Journal of Chemical Physics*, 118(3764), 2003.

[64] D. Emin. *Physical Review B*, 48(13691), 1993.

[65] T. Holstein. *Annals of Physics*, 8(325), 1959.

[66] T. Holstein. *Annals of Physics*, 281(725), 1959.

[67] K. Hannewald et al. *Physical Review B*, 69(075211-1), 2004.

[68] R. W. Munn and R. J. Silbey. *Journal of Chemical Physics*, 83(1843), 1985.

[69] Y. Zhao et al. *Journal of Chemical Physics*, 100(2335), 1994.

[70] L. J. Wang et al. *Journal of Chemical Physics*, 127(044506), 2007.

[71] I. Fishchuk et al. *Physical Review B*, 67(224303-1), 2003.

[72] A. Troisi and G. Orlandi. *Journal of Physical Chemistry*, 110(4065), 2006.

[73] A. Troisi. *Advanced Materials*, 19(2000), 2007.

[74] O. Ostroverkhova et al. *Applied Physical Letters*, 88(162101), 2006.

[75] O. D. Jurchescu et al. *Applied Physics Letters*, 84(3061), 2004.

[76] V. Podzorov et al. *Physical Review Letters*, 93(086602), 2004.

[77] T. Sakanoue and H. Sirringhaus. *Nature Materials*, 9(736), 2010.

[78] J. Takeya et al. *Japanese Journal for Applied Physics*, 44(L1393), 2005.

[79] V. Podzorov et al. *Physical Review Letters*, 95(226601), 2005.

[80] K. Marumoto et al. *Physical Review Letters*, 97(256603), 2006.

[81] D. V. Lang et al. *Physical Review Letters*, 93(086802), 2004.

[82] K. P. Pernstich et al. *Nature Materials*, 7(321), 2008.

[83] N. Koch et al. *Physical Review Letters*, 96(156803), 2006.

[84] P. Atkins and R. Friedman. *Molecular Quantum Mechanics Fourth Edition*. Oxford University Press, 2008.

[85] P. J. Mulders and W. Ubachs. *The Structure of Matter*. Vrije Universiteit Amsterdam, 2003.

[86] P. A. Bobbert et al. *Physical Review Letters*, 102(156604), 2009.

[87] T. D. Nguyen et al. *Nature Materials*, 9(345), 2010.

[88] D. R. McCamey et al. *Physics Review Letters*, 104(017601), 2010.

[89] Z. G. Yu. *Physical Review Letters*, 106(106602), 2011.

[90] B. Kanchibotia et al. *Physical Review B*, 78(193306), 2008.

[91] N. J. Rolfe et al. *Physical Review B*, 80(241201), 2009.

[92] A. J. Drew et al. *Nature Materials*, 8(109), 2008.

[93] J. D. Jackson. *Classical Electrodynamic Third Edition*. John Wiley & Sons, Inc., 1999.

[94] C. E. Soliverez. *Journal of Physics C: Solid State Physics*, 13(L1017), 1980.

[95] R. Moskowitz and E. Della Torre. *IEEE Transactions of Magnetism*, 2(739), 1966.

[96] I. Žutić et al. *Review of Modern Physics*, 76(323), 2004.

[97] H. M. McConnell. *Journal of Chemical Physics*, 24(764), 1956.

[98] K. Schulten and P. J. Wolynes. *Journal of Chemical Physics*, 68(3292), 1978.

[99] R. J. Elliott. *Physical Review*, 96(266), 1954.

[100] Y. Yafet. *Solid State Physics*, 14, 1963.

[101] F. Beuneu and P. Monod. *Physical Review B*, 18(2422), 1978.

[102] M. I. D'yakonov and V. I. Perel. *Fiz. Tverd. Tela*, 13(3581), 1971.

[103] J. Fabian et al. *Acta Physica Slovaca*, 57(565), 2007.

[104] A. G. Aranov G. L. Bir and G. E. Pikus. *Sov. Phys. JETP*, 42(705), 1975.

[105] J. Rybicki et al. *Synthetic Metals*, 160(280), 2010.

[106] Private discussion with S. Fratini.

[107] D. Huertas-Hernandos et al. *Physical Review B*, 74(155426), 2006.

[108] D. Huertas-Hernandos et al. *Physical Review Letters*, 103(146801), 2009.

[109] J. S. Cámara. *Rapport de Stage Master 2 Recherche*, 2011.

[110] J. S. Jeong et al. *Physical Review B*, 84(195457), 2011.

[111] Photo tetracene taken by user Northfox on 26 October 2007 and uploaded to wikipedia commons and ball and stick image tetracene taken by users Ben Mills and Jynto on 12 November 2009 and uploaded to wikipedia commons.

[112] `http://www.ncnr.nist.gov/AnnualReport/FY2003_html/RH5/`.

[113] R. B. Campbell et al. *Acta Crystallographica*, 15(289), 1962.

[114] D. Holmes et al. *Chemistry - A European Journal*, 5(3399), 1999.

[115] U. Sondermann et al. *Journal of Physical Chemistry*, 89(1735), 1999.

[116] RWI. de Boer et al. *Journal of Applied Physics*, 95(1196), 2004.

[117] C. Goldmann et al. *Journal of Applied Physics*, 96(2080), 2004.

[118] A. Hepp et al. *Physical Review Letters*, 91(157406), 2003.

[119] C. Santato et al. *Applied Physics Letters*, 86(141106), 2005.

[120] F. Cicoira et al. *Advanced Functional Materials*, 15(375), 2005.

[121] Photo pentacene taken by user Northfox on 26 October 2007 and uploaded to wikipedia commons and ball and stick image pentacene taken by users Ben Mills and Jynto on 12 November 2009 and uploaded to wikipedia commons.

[122] `http://www.mrsec.umn.edu/nuggets/Fritz/fritznugget.shtml`.

[123] O. D. Jurchescu et al. *Acta Crystallographica Section B*, 62(330), 2006.

[124] W. H. Taylor. *Zeitschrift fr Kristallographie*, 93(151), 1936.

[125] S. A. Akopyan et al. *Zhurnal Strukturnoi Khimii*, 3(602), 1962.

[126] D. E. Henn and W. G. Williams. *Journal of Applied Crystallography*, 4(256), 1971.

[127] I. Bulgarovskaya. *Latvijas PSR Zinatnu akademijas vestis. Fizikas un tehnisko zinatnu serija*, 4(53), 1983.

[128] T. Siegrist et al. *Advanced Materials*, 19(2079), 2007.

[129] C. C. Mattheus et al. *Acta Crystallographica Section C: Crystal Structure Communications*, 57(939), 2001.

[130] T. Siegrist et al. *Angewandte Chemie International Edition*, 40(1732), 2001.

[131] J. E. Anthony et al. *Chemical Review*, 106(5028), 2006.

[132] J. E. Anthony et al. *Organic Letters*, 4(15), 2002.

[133] C. D. Sheraw et al. *Advanced Materials*, 15(2009), 2003.

[134] Z. Zhu et al. *Russian Journal of Physical Chemistry A*, 82(2293), 2008.

[135] O. L. Griffith et al. *Journal of The American Chemical Society*, 132(580), 2010.

[136] J. Chen et al. *Journal of Physical Chemistry B*, 110(16397), 2006.

[137] J. Chen et al. *Journal of Applied Physics*, 103(114513), 2008.

[138] M. M. Payne et al. *Journal of The American Chemical Society*, 127(4986), 2005.

[139] J. E. Anthony et al. *Journal of The American Chemical Society*, 123(9482), 2001.

[140] M. M. Payne et al. *Organic Letters*, 6(3325), 2004.

[141] K. C. Dickey et al. *Advanced Materials*, 18(1721), 2006.

[142] W. H. Lee et al. *Applied Physical Letters*, 91(092105), 2007.

[143] Y. L. *American Institute of Chemical Engineers*, 53(1066), 2007.

[144] L. Pecha et al. *Chemistry of Heterocyclic Compounds*, 38(695), 2002.

[145] E. M. Campi et al. *Zeitschrift fr anorganische und allgemeine Chemie*, 632(1483), 2006.

[146] M. Cölle et al. *Advanced Functional materials*, 13(108), 2003.

[147] I. Hernández et al. *Journal of Physical Chemistry B*, 113(14079), 2009.

[148] M. Braun et al. *Journal of Chemical Physics*, 114(9625), 2001.

[149] T. Lee et al. *Crystal Growth and Design*, 7(1803), 2007.

[150] M. Cölle et al. *Chemistry Communications*, (2908), 2002.

[151] A. J. Drew et al. *Physical Review Letters*, 100(116601), 2008.

[152] M. Brinkmann et al. *Chemistry Materials*, 16(4627), 2004.

[153] Y. Wang et al. *Chemistry Materials*, 11(530), 1999.

[154] L. Wang et al. *Displays*, 21(47), 2000.

[155] L. Sapochak et al. *Chemistry Materials*, 16(401), 2004.

[156] J. Kang et al. *Journal of the American Chemical Society*, 130(12273), 2008.

[157] J. E. Anthony et al. *Journal of the American Chemical Society*, 123(9482), 2001.

[158] M. Cölle and W. Brütting. *physica status solidi (a)*, 201(1095), 2004.

[159] `http://www.ccp14.ac.uk/ccp/ccp14/ftp-mirror/gsas/public/gsas/manual/GSASManual.pdf`.

[160] M. Abramowitz and I.A. Stegun. *Handbook of Mathematical Functions*. Dover Publications Inc., Ch. 22.

[161] Von Dreele. *Journal of Applied Crystallography*, 30(517), 1997.

[162] H. J. Bunge. *Texture Analysis in Materials Science: Mathematical Methods*. Butterworth-Heinemann, 1982.

[163] M. Rajeswaran and V. V. Jarikov. *Acta Crystallographica Section E*, E59(m306), 2003.

[164] S. H. Neddermeyer and C. D. Anderson. *Physical Review*, 51(884), 1937.

[165] G. H. Eaton and S. H. Kilcoyne. *Muon production: Past, Present and Future.* Scottish Universities Summer School in Physics, 1999.

[166] R. De Renzi. *μSR and NMR: Fundamental Concepts and Selected Examples.* Scottish Universities Summer School in Physics, 1999.

[167] S. J. Blundell. *Contemporary Physics*, 40(175), 1999.

[168] A. Carne. *Hyperfine Interactions*, 65(1175), 1990.

[169] `http://www.isis.stfc.ac.uk/index.html`.

[170] M. Seidel and P. A. Schmelzbach. Upgrade of the psi cyclotron facility to 1.8 mw. *Cyclotrons and Their Applications 2007, Eighteenth International Conference*, 2007.

[171] S. Adam et al. *Operation and development of the Proton Accelerator complex in 2006.* Paul Scherrer Institute (PSI Scientific Report 2006), 2006.

[172] `http://www.psi.ch/`.

[173] K. Nagamine. *Introductory Muon Science.* Cambridge University Press, 2007.

[174] E. Morenzoni. *Physics and Applications of Low Energy Muons.* Scottish Universities Summer School in Physics, 1998.

[175] T. Proschka et al. *Physica B*, 326(51), 2003.

[176] V. N. Gorelkin et al. *Physica B*, 289(409), 2000.

[177] D. G. Eshchenko et al. *Physical Review B*, 66(035105), 2002.

[178] P. Percival et al. *Advances in Chemistry Series*, 175(335), 1979.

[179] D. C. Walker. *Muon and Muonium.* Cambridge University Press, 1983.

[180] L. D. A. Siebbeles et al. *Journal of Chemical Physics*, 111(7493), 1999.

[181] D. C. Walker et al. *Journal of Chemical Physics*, 118(3233), 2003.

[182] V. Storchak et al. *Physical Review Letters*, 78(2835), 1997.

[183] V. Storchak et al. *Hyperfine Interactions*, 105(189), 1997.

[184] C. Bouchiat and L. Michel. *Physical Review*, 106(170), 1957.

[185] K. Jungmann. *Aspects of Fundamental Muon Physics.* Scottish Universities Summer School in Physics, 1999.

[186] M. Bardon et al. *Physical Review Letters*, 14(449), 1965.

[187] Y. Kuno and Y. Okada. *Review of Modern Physics*, 73(151), 2001.

[188] J. H. Brewer and R. Cywinski. *μSR: An Introduction.* Scottish Universities Summer School in Physics, 1998.

[189] S. J. Blundell. *Chemical Review*, 104(5717), 2004.

[190] B. D. Patterson. *Reviews of Modern Physics*, 60(69), 1988.

[191] J. W. Schneider. *PhD Thesis, Universität Zürich*, 1989.

[192] M. Heming et al. *Chemical Physics Letters*, 128(100), 1986.

[193] F. Pratt. *Philosophical Magazine Letters*, 75(371), 1997.

[194] M. Senba. *Physical Review A*, 62(042505), 2000.

[195] E. Roduner. *Aspects of muon chemistry.* Scottish Universities Summer School in Physics, 1998.

[196] E. Roduner et al. *Journal of Physical Chemistry A*, 102(7591), 1998.

[197] D. G. Fleming et al. *Journal of Physical Chemistry B*, 106(6395), 2002.

[198] M. D. Bridges et al. *Journal of Physical Chemistry C*, 111(9779), 2007.

[199] E. Roduner. *Hyperfine Interactions*, 65(857), 1990.

[200] L. Schulz, 2010. Inaugural-Dissertation: Charge and Spin Dynamics in Organic Materials and Metal-Organic Spin Valve Structures.

[201] E. Roduner et al. *Chemical Physics*, 192(231), 1995.

[202] P. F. Meier. *Physical Review A*, 25(1287), 1982.

[203] M. Heming et al. *Hyperfine Interactions*, 32(727), 1986.

[204] J. S. Lord. *Physica B*, (374,472), 2006.

[205] E. Roduner. *Chemical Society Reviews*, (337), 1993.

[206] R. F. Kiefl et al. *Physical Review Letters*, 53(90), 1984.

[207] Private discussion with I. McKenzie.

[208] I. McKenzie. *Journal of Physical chemistry A*, 114(12759), 2010.

[209] L. Schulz et al. *Physical Review B*, 84(085209), 2011.

[210] V. G. Storchak. *Mass and Charge Transport in Condensed Matter via μSR.* Scottish Universities Summer School in Physics, 1998.

[211] Z. G. Yu. *Physical Review B*, 77(205439), 2008.

[212] S. Guha et al. *Physical Review B*, 67(125204), 2003.

[213] M. D. Halls and R. Aroca. *Canadian Journal of Chemistry*, 76(1730), 1998.

Appendix A

Errors: A Brief Note

As of yet the errors present in the data have not been discussed. This aim of this section is to discuss the origin of the error bars reported in the analysis and the impact they have on the results presented in this thesis.

There are three types of error in the data presented here. The first of these is the error on the raw asymmetry data. These are purely statistical and originate from the number of measurements taken of the asymmetry at any given field i.e. the number of the muon events measured. They follow a $1/\sqrt{2}$ relationship hence to reduce the error bars by half the number of events needs to be quadrupled. It is worth noting at this point that all statistical errors are contained within the standard error bars in the figures however some of the systematic errors are shown as confidence intervals in the form of dashed lines to give a better representation of the errors. To obtain these values the data was analysed in the WIMDA software which automatically generates the value from the data. This error can be reduced by increasing the number of events either indirectly (improving the signal to background ratio) or directly by counting for longer. These error bars only impact the data significantly if the ALCs posses a particularly small amplitude as they can add uncertainty to the modelling and mask the finer detail of the ALC. However, in the data presented in this thesis the ALCs are very broad and deep making the error bars less significant and the finer detail is easily visible in each case.

The second type of error is that present in the eSR values extracted from the modelling which initially, from the temperature data appears to be over estimated. However, this error is not statistical but in fact is a purely systematic error. It originates from two sources. The first source is a propagation of the errors from the modelling parameters. These are determined by altering the values individually until the overall eSR values changes significantly (approx. by a half) and is analogous to a FWHM error. The second source of error for the eSR arises from the background subtraction of the ALC from the raw data. This error is again systematic in nature and is achieved by carrying out three independent background subtractions by

three different people. The subtracted data is then modelled in the same fashion with separate analyses and the final eSR values compared. The value for the error is taken as half the maximum difference and is the larger of the two contributors to the total error on the eSR. Given the lack of statistical error from the modelling of the data this is the best form of error that can be presented for the data and is a more truthful representation of the variation in the analysis. The impact of the magnitude of the error is made clear in the temperature analysis where it is apparent, from the "over fitted data", that in the lower energy regime there is a more significant variation in the fits where as in the higher energy regime this becomes less of a concern and the fits are more constrained.

The last type of error is that presented on the energy data extracted from the temperature dependance fits. This error is purely a statistical error and is obtained from the unweighted Arrhenius fits of the temperature data. These errors are reflective of the errors on the eSR and naturally decrease as the % variation on the eSR decreases also. These errors are the most significant in terms of impacting the results as they only permit a straight line to be deduced from the energy data and may mask any small changes in the energies with changes in Z-number. In order to improve these errors the background fitting and subtraction analysis ideally needs to be improved or a suitable, different method is required (the author welcomes any suggestions :D). The errors discussed in this section, to the best of the authors knowledge, cover all the known statistical and systematic errors present in the analysis of the data reported in this thesis.

Publications

- *The Effects of Deuteration on Electron Spin Relaxation in Organic Semiconductors.* **M. Willis**, L. Nuccio, L. Schulz, F. L. Pratt, J. Lord, K. Sedlak, J. E. Anthony, W. P. Gillin and A. J. Drew, **in preparation**

- *The Importance of the Spin-Orbit interaction in Organic Semiconductors.* L. Nuccio, **M. Willis**, L.Schulz, S. Fratini, F. Messina, M. D'Amico, F. L. Pratt, J. Lord, I. McKenzie, P. Shakya, P. Desai, M. Loth, B. Purushothaman, J. Anthony, M. Heeney, R. M. Wilson, I. Hernandez, M.Cannas, K. Sedlak, T. Kreouzis, C. Bernhard, W.P. Gillin and A. J. Drew, **submitted Nature Materials**

- *Importance of intramolecular electron spin relaxation in small-molecule semiconductors.* L. Schulz, **M. Willis**, L. Nuccio, P. Shusharov, S. Fratini, F. L. Pratt, W. P. Gillin, T. Kreouzis, M. Heeney, N. Stingelin, C. A. Stafford, D. J. Beesley, C. Bernhard, J. E. Anthony, I. McKenzie, J. S. Lord and A. J. Drew, Physical Review B 84(085209), **2011**

- *Engineering spin propagation across a hybrid organic/inorganic interface using a polar layer.* L. Schulz, L.Nuccio, **M. Willis**, P. Desai, P. Shakya, T. Kreouzis, V. K. Malik, C. Bernhard, F. L. Pratt, N. A. Morley, A. Suter, G. J. Nieuwenhuys, T. Prokscha, E. Morenzoni, W. P. Gillin and A. J. Drew, Nature Materials 10(39), **2011**

- *Electron spin relaxation in organic semiconductors probed through μSR.* L Nuccio, L Schulz, **M. Willis**, F L Pratt, M Heeney, N Stingelin, C Bernhard and A J Drew, Journal Of Physics: Conference Series 292(012004), **2011**

- *Coexistence and Competition of Magnetism and Superconductivity on the Nanometer Scale in Underdoped BaFe(1.89)Co(0.11)As(2).* P. Marsik, K. W. Kim, A. Dubroka, M. Rössle, V. K. Malik, L. Schulz, C. N. Wang, Ch. Niedermayer, A. J. Drew, **M. Willis**, T. Wolf, and C. Bernhard, Physical Review Letters 105(057001), **2010**